Stopping in central $\sqrt{s_{NN}} = 200$ GeV $Au + Au$ collisions at RHIC

Peter Harald Lindenov Christiansen
Niels Bohr Institute
Denmark
May 2, 2003

Ph.D. Dissertation in Physics
Faculty of Science — University of Copenhagen

Supervisor : Hans Bøggild

Preface

In relativistic heavy ion physics, nuclei are collided at large center-of-mass energies and the dynamics of the collision is probed by measuring the produced particles. In the collisions the baryon number of the initial nuclei is conserved. By measuring the baryon rapidity densities and subtracting the anti–baryon rapidity densities it is possible to study the stopping of the participating nucleons.

The data presented in the thesis was collected with the BRAHMS detector at the Relativistic Heavy Ion Collider (RHIC) at Brookhaven National Laboratory (BNL). BRAHMS is the only experiment at RHIC which can measure and identify particles over a large range in rapidity. In this thesis the measurement of proton and anti–proton transverse momentum spectra at several rapidities $0.0 < y < 3.0$ is presented. From the measured spectra the rapidity densities of protons, anti–protons and (from the difference) net–protons are derived and the implications for the stopping of the initial nucleons at RHIC is discussed and compared to model predictions and measurements at lower bombarding energies.

In chapter 1 general relativistic heavy ion physics is briefly introduced, before the subject of the thesis, the stopping of the nucleons, is addressed in detail in chapter 2. Chapter 3 discuss the BRAHMS detector and the data analysis is presented in chapter 4. The results are shown in chapter 5 and conclusions are summarized in chapter 6. In appendix I the acronyms used are explained.

The results presented here are preliminary, and as such, not official published BRAHMS results. Before quoting the results please contact the author[1] and the spokesmen of the BRAHMS collaboration[2]

Research carried out in part at the Relativistic Heavy Ion Collider, Brookhaven National Laboratory, which is supported by the U.S. Department of Energy, Division of Nuclear Physics of the Office of Science, under contract with BNL (No.DE-AC02-98CH10886).

Many people have helped and inspired me during my Ph.D. studies. I would like to thank my supervisor Hans Bøggild and the rest of the group here in Copenhagen, and the rest of

---

[1] `pchristi@nbi.dk`

[2] Flemming Videbæk (spokesman, `videbaek@bnl.gov`) and Jens Jørgen Gaardhøje (deputy spokesman, `gardhoje@nbi.dk`)

the many BRAHMS collaborators (see appendix A).

During the work on this analysis I have had many good discussions with Jens Jørgen Gaardhøje, Ian Bearden (and his ax “the motivator”), Pawel Staszel, Djamel Ouerdane, Claus Jørgensen, Christian Holm, David Sandberg, Marco Germinaro, Flemming Videbæk, Eun-Joo Kim, Kimmo Tuominen, and many others. I would like to thank Ole Hansen for his careful reading and many valuable comments on the content of this thesis, and Kim Austin for his efforts of correcting my english. A special thanks to my office mate Djamel Ouerdane for three good years of close collaboration.

Finally I would like to thank my friends and family for their love and support. In particular my dear friend Maria, and my father and mother, Ulrich and Lisbet. Thanks for everything.

Copenhagen, May 2003

Peter Christiansen

Contents

Chapter 1

Heavy Ion Physics

In Ultra Relativistic Heavy Ion Physics, large nuclei ($A \gg 1$) are collided to study the properties of matter under extreme conditions. The ultimate goal is to verify the existence and study the properties of a new phase of matter called the Quark Gluon Plasma (QGP).

In this chapter a brief review of modern theoretical tools and relevant experimental data is presented. Kinematic variables used are described in Appendix B.

1.1 QCD

Hadronic matter is made of quarks, and divided in two categories, *baryons* consisting of three quarks (e.g. nucleons), and *mesons* consisting of a quark and an anti–quark (e.g. pions and kaons). There are 6 different quarks (and corresponding anti–quarks) : u (up), d (down), s (strange), c (charm), b (bottom), and t (top).

In addition to an electrical charge the (anti–)quarks have a (anti–)color charge. There are three (anti–)color charges : (anti–)red, (anti–)green, and (anti–)blue. The interaction between color charges is called the strong interaction and is responsible for binding the quarks into hadrons.

Quantum Chromo Dynamics (QCD) is the theory describing the strong interactions. In QCD the strong interaction between quarks is mediated by gluons that themselves carries color charge. QCD has many features that are different from Quantum Electro Dynamics (QED) which describes the interaction of electrical charges. Below some of the aspects of QCD most relevant for heavy ion physics are described.

Confinement

A single “free” quark has never been observed. The quarks are confined inside the hadrons. Only systems of quarks which are “colorless” can be observed, hence either the system must have all three colors (baryons) or a color and an anti–color (mesons).

Gluonic Self Interaction

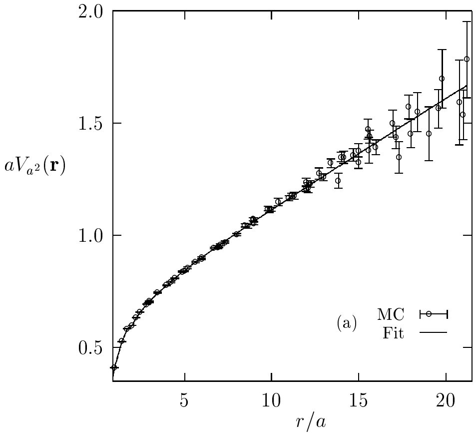

Figure 1.1: The potential between heavy quarks. Figure is taken from [2].

The 8 gluons are the gauge bosons of QCD, analogous to the single photon in QED, but unlike the photon, the gluons carries (color) charges. Gluons can therefore interact with one another.

In Figure 1.1 the potential energy between two (heavy) quarks is shown from a Lattice QCD (LQCD) calculation. At short distances the shape is similar to the Coulomb potential ($\propto \frac{1}{r}$), but at large distances the potential increases linearly because of the gluon self interaction. The force between the quarks is the slope of the potential and is called the *string tension* σ for the linear part and is of the order $\sigma \sim 1$ GeV/fm. Due to the gluon self interaction, the field between two quarks is confined in a narrow flux tube, so the system reminds of a string.

When the quarks are being separated the system will eventually have enough energy to make it energetically possible to form one or more quark–anti-quark pairs and break up the "string" and produce more hadrons. This is the basic idea of the string models discussed in section 2.3.

Coupling Constant

Interactions where the momentum transfer is so large that the cross sections can be computed using Perturbative QCD (pQCD) are called *hard* and interactions where pQCD is not applicable are called *soft*.

The dependence of the strong coupling constant α_s on the four momentum transfer Q is shown in Figure 1.2. It is only at large momentum transfers, where α_s is small ($\alpha_s \ll 1$), that perturbative calculations are convergent. For small momentum transfers other methods must be applied. One approach is the use of phenomenological models (e.g. string models) to describe hadronic interactions, but it is also possible to solve the QCD equations numerically

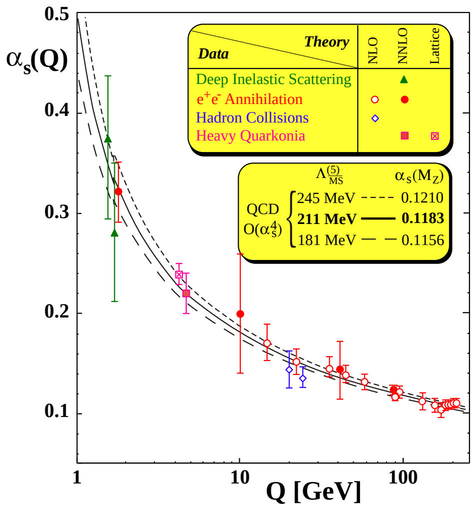

Figure 1.2: The strong coupling constant α_s as a function of the momentum transfer Q. Figure is taken from [1].

on a lattice (LQCD) for systems in equilibrium.

1.2 QGP and Deconfinement

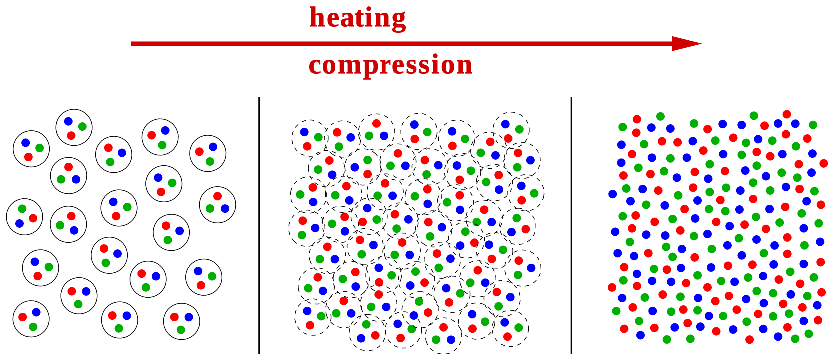

Figure 1.3: Simple picture of the QGP phase transition.

In the last section, hadrons and the strong interaction was discussed at normal temperatures ($T \sim 0$) and nuclear densities ($\rho \sim 0.17\text{GeV}/\text{fm}^3$). The energy density of a single nucleon is almost three times larger than the nuclear density, so the nucleons inside a nucleus would "overlap" if the nucleus was compressed a factor of three. When the nucleons overlap, the quarks inside different nucleons could start to interact directly and so the quarks would no longer be confined inside a hadron, but could move around freely inside the large dense zone. This new phase of quark and gluon matter is called the Quark Gluon Plasma (QGP). In Figure 1.3 this simple description is illustrated.

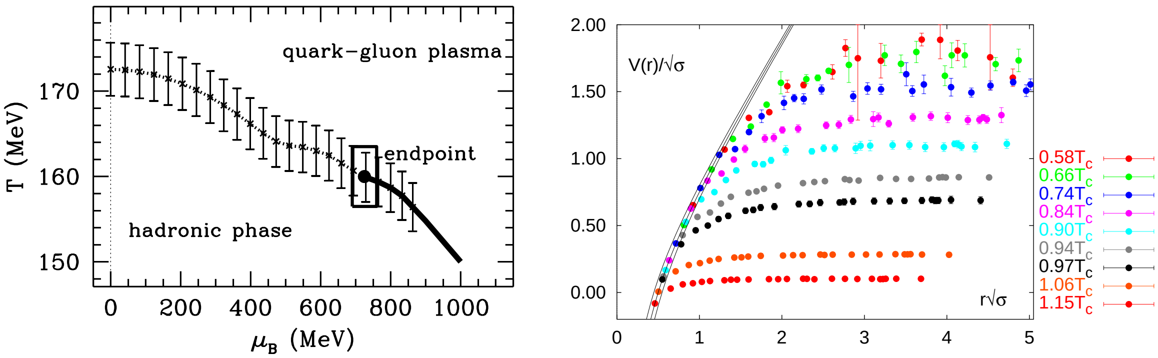

Figure 1.4: Left: A zoom in on the QCD phase diagram. The endpoint in the plot is the tricritical point. Figure is taken from [3]. Right: The heavy quark potential in units of $\sqrt{\sigma}$ (where σ is the string tension) as a function of the critical temperature ($\mu_B = 0$). $r\sqrt{\sigma} = 1$ corresponds to the distance $r \sim 0.5$ fm. Figure is taken from [4].

The question of a possible phase transition has been studied in QCD by Lattice QCD (LQCD) calculations. Interested readers are recommended to study the references in e.g. [3] for details of LQCD calculations, here only the results will be shown.

For many years only the case with zero baryon chemical potential μ_B could be studied, but in recent years it has been possible to study the phase transition for finite chemical potentials as well. In Figure 1.4 (left) the critical temperature, for the phase transition to a QGP, is shown for different chemical potentials. At $\mu_B = 0$ the critical temperature is found to be $T_C = 172 \pm 3$ MeV [3]. The order of the phase transition is disputed, but the common claim [3] is that the phase transition is second order (cross over) for $\mu_B = 0$ and first order for $T = 0$. This means that a tricritical point must exist and it was determined in [3] to be at $T \sim 160\text{MeV}, \mu \sim 725\text{MeV}$.

The second figure in Figure 1.4 shows the heavy quark potential as a function of the critical temperature. As the temperature increases, the potential decreases, beyond distances of $r \sim 0.25$ fm and eventually at $T > T_C$ flattens, meaning that the color charge is screened at distances of the order $r \sim 0.25$ fm in the QGP phase. The bound quark states (hadrons) are dissolved and the quarks (and gluons) are deconfined.

1.3 Pictures of the Collision

In this section some "pictures" will be described that are central to heavy ion collisions. "Pictures" here means that qualitative features of the collisions can be described in simple extreme scenarios to help build up intuition, whereas models should describe quantitative features and make numerical predictions.

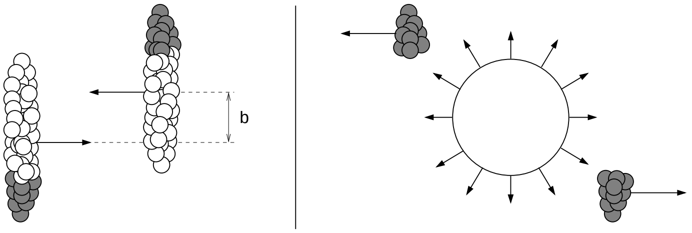

Figure 1.5: The two nuclei collide at impact parameter b. The "white" nucleons that interact with nucleons in the other nuclei are called participants and the grey nucleons are called spectators.

1.3.1 Participant–Spectator Picture

The impact parameter b is defined as the transverse distance between the center of the two colliding nuclei. In Figure 1.5 a schematic geometrical picture of the collision is shown. The number of participating nucleons depends strongly on b and it is only in the very central collisions $b \sim 0$ fm that all nucleons interact.

Often the centrality c is used instead of the impact parameter. It is defined as :

$$c = \frac{\int_0^b \frac{d\sigma_{in}(b')}{db'} db'}{\sigma_{in}} \cdot 100\% \tag{1.1}$$

where σ_{in} is the total inelastic cross section, $\frac{d\sigma_{in}(b)}{db}$ the differential cross section, and b_c is the impact parameter cut–off. For a given impact parameter c is the probability of another inelastic collision having the same impact parameter or lower. This can be confusing, since $c \sim 0\%$ when $b \sim 0$ fm (central collisions) and $c \sim 100\%$ for very peripheral collisions. The experimental determination of centrality is discussed in section 3.3.

If it is assumed that the colliding nuclei are identical, spherical, and the inelastic cross–section is $\frac{d\sigma_{in}(b)}{db}db = 2\pi b db$ (solid sphere), the following simple relation between impact parameter and centrality is obtained

$$c = \frac{\int_0^{b_c} 2\pi b db}{\int_0^{2R} 2\pi b db} = \frac{b_c^2}{4R^2} \tag{1.2}$$

where R is the radius of the nuclei. For Au, containing 197 nucleons, the radius is $R = 1.2 \cdot 197^{1/3} = 7.0$ fm. This means that the centrality range 0–5 % corresponds to the impact parameter range 0–3.1 fm.

A more sophisticated calculation of the collision geometry can be done in the Glauber model [5]. The following description was inspired by [6]. In the Glauber model three assumptions are made :

- Nucleons are distributed according to a density function (e.g. Woods–Saxon)

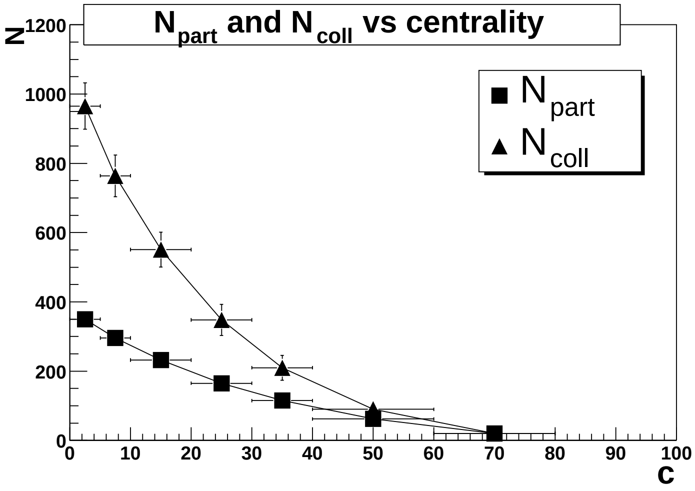

Figure 1.6: Glauber model calculation of the number of participants N_{part} and binary collisions N_{coll}. The values of the calculation have been taken from [7].

- Nucleons travel in straight lines and are not deflected by interactions
- Nucleons interact with the inelastic cross section σ_{NN} measured in $p+p$ collisions at the same initial energy even after multiple interactions

This allows the number of participants N_{part} and the number of binary collisions N_{coll} to be calculated. The number of binary collisions is the number of nucleon–nucleon collisions assuming that all nucleons whose trajectories intersect also interact. In a $p+p$ collision there is always two participants and one binary collision, however in heavy–ion collisions a nucleon can interact with several nucleons in the other nucleus.

In practice there is two approaches to the calculation. One is the Monte Carlo (MC) simulation where the nucleons are distributed over the nuclei according to the density function and the other is the optical–limit approach where the problem can be solved by numerical integrals. The difference between the methods is not in the number of participants calculated at a fixed impact parameter, but in the total cross section i.e., in the normalization to centrality. For the optical limit approach a cut–off impact parameter has to be introduced to fix the total cross section. This introduces large systematic differences between the two calculations in peripheral collisions.

In Figure 1.6 the results from a Glauber calculation is shown, and it is seen that the number of binary collisions rises faster than the number of participants as the collisions becomes more central.

1.3.2 Bjorken Picture

In his famous paper from 1983 [8], Bjorken describes the evolution of the central rapidity region in heavy–ion collisions based on observations from $p+p$ collisions and hydrodynamics.

The important assumptions in the Bjorken picture is

- Boost invariance. The rapidity densities dN/dy are independent of rapidity for at least a few units of rapidity around mid–rapidity in $p+p$ and $p+A$ collisions, from which it is assumed that the same is true for $A+A$ collisions.

- Transparency. The nuclei interpenetrate in the $A+A$ collision and the central plateau is formed through particle production from the breaking of color strings. The fragments of the original nuclei end up some units of rapidity away from mid–rapidity. In Lorentz frames with velocities close to the mid–rapidity frame, the nuclei look like receding flat pancakes.

- The transverse expansion of the source can be ignored for most of the collisions because of the large initial transverse scale of the source compared to its longitudinal scale. This is only true for central collisions and reduces the problem to a 2–dimensional problem in the coordinates z and t.

- At some early time, assumed to be of the order of the characteristic hadronic time scale $t \sim 1$ fm/c, the system thermalizes and hydrodynamics governs the evolution and expansion of the source.

The first assumption is very powerful. If the collision observed in the mid–rapidity frame is compared to the collision observed in another Lorentz frame the evolution of the source will be the same in both frames in a rapidity interval differing from the beam rapidity region. From this it is argued that the initial energy density is the same in both frames (at the same local time). Due to the homogeneity of the source in all the frames there is no pressure gradient to change the longitudinal flow and the velocity of each fluid element stays the same. If it is assumed that, at $t = 0$, right after the two nuclei have collided, the longitudinal extent of the source is negligible the relation $z = \beta t$ therefore holds true at all times $t > 0$.

The proper time τ is then

$$\tau = \frac{t}{\gamma} = \sqrt{t^2(1 - \frac{z^2}{t^2})} = \sqrt{t^2 - z^2} \tag{1.3}$$

As the evolution looks the same in all mid–rapidity like frames, the energy density and pressure only depends on τ. This gives rise to hyperbolas of constant energy densities that can be used to distinguish between the different phases in the evolution of the collision. In Figure 1.7 a possible evolution of the system is illustrated.

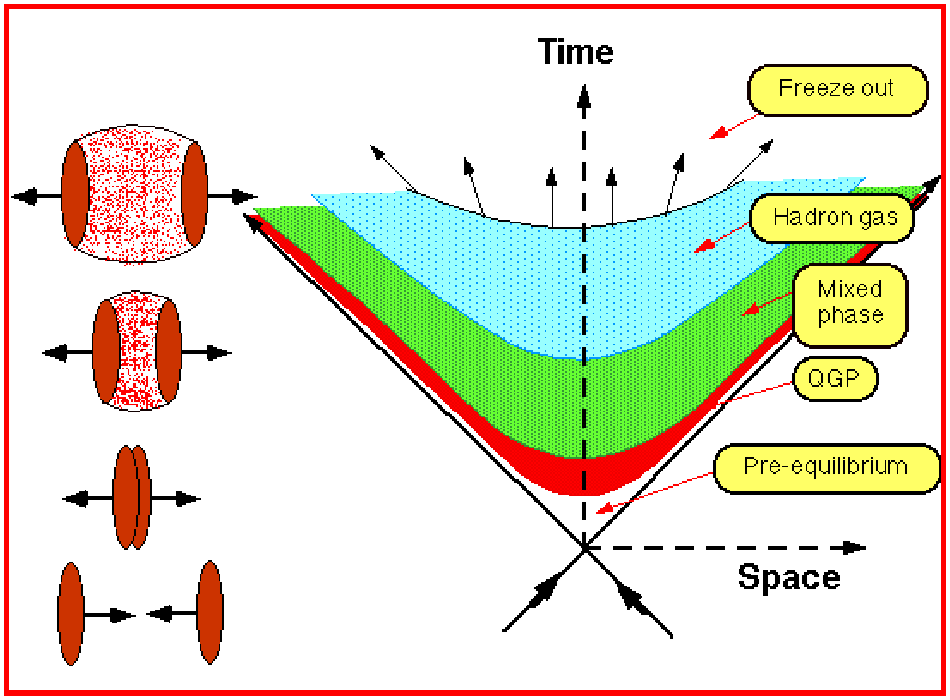

Figure 1.7: The space–time evolution of the collision in the Bjorken picture in a scenario where a QGP is formed. After a proper time τ of 1 fm/c the system is in a thermalized QGP. It then cools of by expanding and eventually the system hadronizes. When all the QGP has hadronized, scattering continues until the system is dilute enough that the mean free path of the hadrons is of the order of the system size and the system freezes out.

Justified by the preservation of entropy in the hydrodynamical expansion, the Bjorken picture also predicts the entropy when the system thermalizes is the same as that at freeze–out. This can be used to make predictions of the final multiplicities if the initial entropy can be calculated. Sometimes this is formulated in another way, extracting the initial energy density from the final multiplicity dN/dy, which is the experimentally accessible quantity.

$$\epsilon = \frac{\langle E \rangle}{V} = \frac{\langle m_T \rangle \cosh{(y)} \frac{dN}{dy} \Delta y}{\mathcal{A} \Delta z} = \frac{\langle m_T \rangle}{\mathcal{A} \tau} \frac{3}{2} \frac{dN^{ch}}{dy} \tag{1.4}$$

Where τ is the initial formation time, usually taken to be the thermalization time–scale 1 fm/c and $\mathcal{A}$ is the transverse area of the zone. dN/dz was derived from the relation $z = \tau \sinh{(y)}$.

1.4 Experimental Highlights

The experimental study of high energy heavy ion collisions at the Heavy–Ion Synchrotron (SIS), Alternating Gradient Synchrotron (AGS), Super Proton Synchrotron (SPS), and Relativistic Heavy Ion Collider (RHIC) has provided numerous measurements. In this section a few of the interesting results from SPS and RHIC will be reviewed, focusing on measurements that suggest that "new physics" (like the QGP) has been observed.

1.4.1 Statistical Model

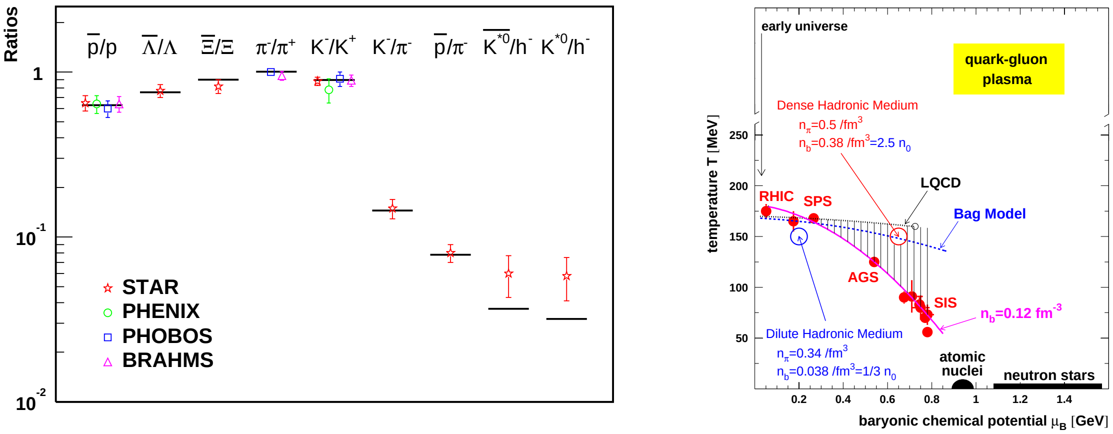

Figure 1.8: Left: Comparison between experimental particle ratios at $\sqrt{s_{NN}} = 130$ GeV and statistical model calculations with $T = 174$ MeV and $\mu_B = 46$ MeV. Figure is taken from [9]. Right: Phase diagram of nuclear matter. The experimental data points are from statistical model fits. Figure is taken from [10].

The statistical model has been very successful at describing the particle ratios of observed hadrons in central collisions from SIS to RHIC energies. The idea is that hadron abundances can be described in a thermal model using only the temperature T and the baryon chemical potential μ_B, see [11] for a clear introduction to the model. In Figure 1.8 a fit to the RHIC data at $\sqrt{s_{NN}} = 130$ GeV is shown.

The success of the model implies that the particles comes from an equilibrated source, and that there is a chemical freeze–out of the source i.e., all the particle ratios are fixed by a single temperature and chemical potential. For SPS and RHIC energies, the T and μ_B obtained from the statistical model follows the phase transition curve calculated in LQCD. This suggests that a thermalized QGP was formed initially and equilibrium was maintained as the system expanded and cooled, before the system finally hadronized and almost immediately stopped interacting inelastically.

1.4.2 J-psi Suppression at SPS

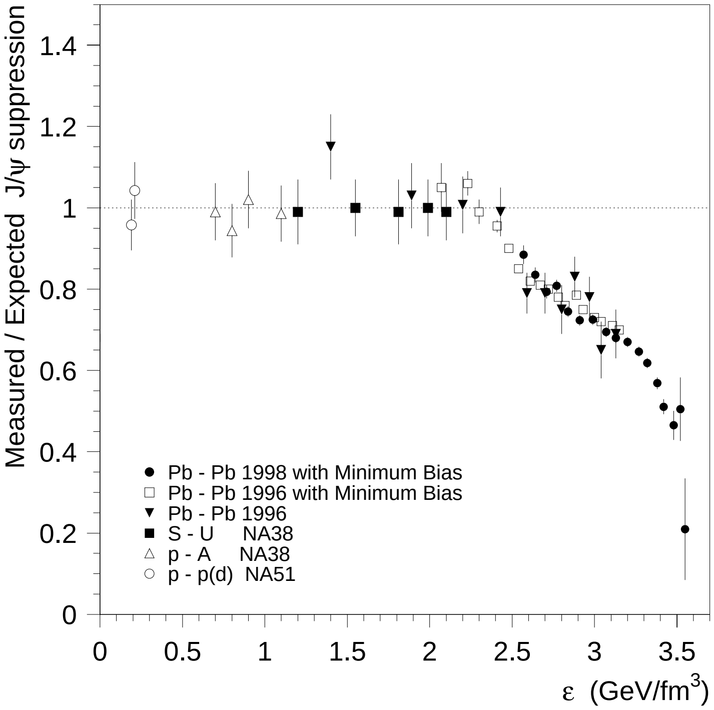

Figure 1.9: Measured J/ψ production yields, normalized to the yields expected, assuming that the only source of suppression is the ordinary absorption by the nuclear medium. The energy density ϵ has been calculated from the charged multiplicity using the Bjorken estimate, equation 1.4. Figure is taken from [12]

The J/ψ particle is a bound $c\bar{c}$ system with mass $m = 3.1$ GeV. Because of the large mass it can only be produced in initial hard interactions. The J/ψ meson is tightly bound and therefore unlikely to break in the relative soft interactions with the surrounding hadrons.

It has been predicted that if the $c\bar{c}$ pair is formed in a QGP state, the screening of the strong interaction (Figure 1.4) would prevent the system from binding, so the yield of J/ψ particles would be suppressed.

The NA50 experiment at the SPS has measured the yield of J/ψ [12]. Figure 1.9 shows the yields normalized to the yields expected if nuclear absorption is the only source of suppression. The suppression observed above the energy density $\epsilon \sim 2.3$ GeV/fm is consistent with the formation of a QGP. The second dip observed at $\epsilon \sim 3.0$ GeV/fm has given rise to speculations that the first dip corresponds to the screening of the χ_C $c\bar{c}$ resonance (responsible for a fraction of the J/ψ yield) and the second dip is the onset of the screening of the tighter bound J/ψ.

High p_T-Suppression and Jets at RHIC

At RHIC there has been a large interest in studying particles with high transverse momentum $p_T > 2$ GeV/c. Particles with such high momenta are primarily produced in hard scatterings early in the collision and they can act as a probe of the dense medium where they are produced. In the first $\sqrt{s_{NN}} = 200$ GeV run (2001), $p+p$ data was collected to be used for comparison with $Au + Au$ data.

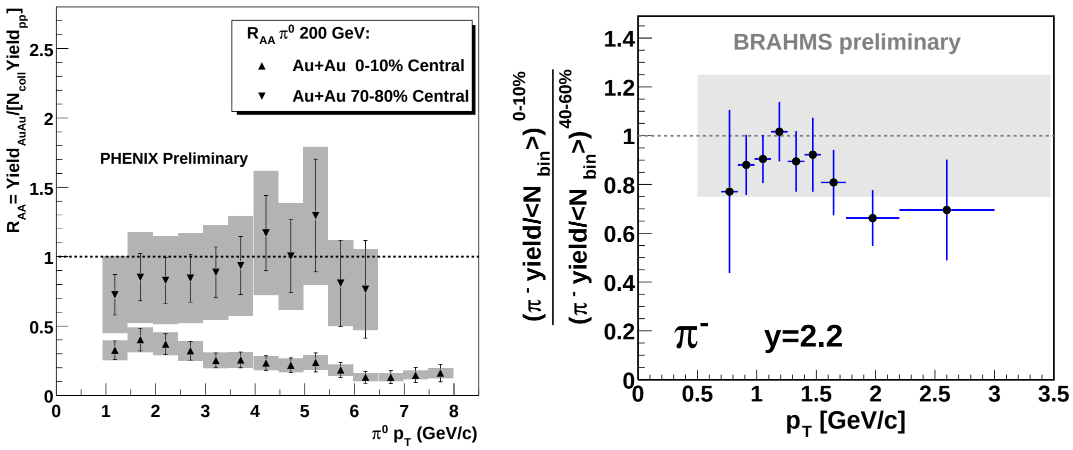

Figure 1.10: Left: R_{AA} for π^0 production in central and peripheral $Au + Au$ collisions at $\sqrt{s_{NN}} = 200$ GeV. The shaded boxes are the errors on the normalization of the ratio ($\langle N_{coll}\rangle$). Figure is taken from [13]. Right: The ratio of the negative pion p_T spectrum from central collisions (0-10 %) to peripheral (40-60%) at $y = 2$, normalised to the mean number of binary collisions. The gray area indicates the uncertainty on the normalization. Figure is taken from [14].

The number of hard scatterings is expected to scale with the number of binary collisions N_{coll}. Therefore the ratio

$$R_{AA}(p_T) = \frac{\text{(Yield per A+A collisions)}}{\langle N_{coll}\rangle\text{(Yield per p+p collision)}} \tag{1.5}$$

called the nuclear modification factor, is often used to compare p+p and Au+Au collisions. Figure 1.10 shows the nuclear modification factor for π^0 [13]. R_{AA} is consistent with 1.0 for peripheral collisions corresponding to no nuclear modification, but in central collisions the factor decreases from 0.4 at low momentum to 0.15 at high momentum, meaning that there is a large suppression of high p_T particles in central collisions. This can be understood if one assumes the particles suffer a large energy loss dE/dx as they propagate through the fireball, indicating that they were produced in a very dense medium.

BRAHMS can measure high p_T particle spectra at forward rapidity ($y > 2$). At forward rapidity no $p + p$ reference spectra are available yet, but instead the central collisions can be compared to peripheral collisions to see if any modification is observed. The first preliminary data are shown in Figure 1.10. Within the large statistical and systematical errors the results are consistent with no modification, but with better counting statistics and the measurement of $p + p$ reference spectra the analysis and results can be refined.

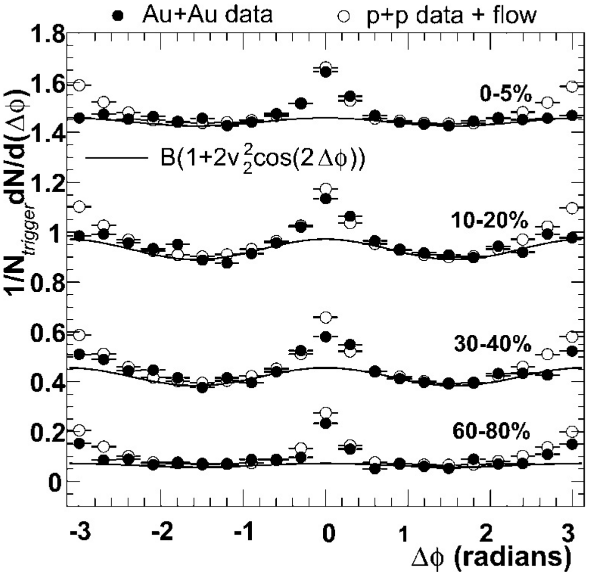

Figure 1.11: Azimuthal distributions ($0 < |\Delta\eta| < 1.4, 4 < p_T^{trig} < 6$ GeV/c) for $Au + Au$ collisions (filled circles) compared to expectations based on $p + p$ collisions (open circles). The curves represents the contribution from elliptic flow for each centrality. Figure is taken from [15].

It is well known from $p + p$ collisions that partons with large transverse momentum produced in the initial hard processes fragments to create high energy clusters of particles called jets. In $p + p$ collisions di–jets, where a produced quark–anti-quark fragments back to back, are easy to identify because of the few particles produced. In heavy–ion collisions, where the particle production is much larger, the jets are identified statistical by triggering on single particles with transverse momentum $p_T^{trig} > 3$ GeV/c, and then building correlations with other particles from the same event with transverse momentum 2GeV/c $< p_T < p_T^{trig}$. In

Figure 1.11 the azimuthal correlations are shown for different centrality classes compared to a prediction based on the $p+p$ data, with a correction for the elliptical flow present in $Au+Au$ collisions [15]. In peripheral collisions both the jet ($\Delta\phi = 0$) and the back–jet ($\Delta\phi = \pi$) are observed, but in central collisions the back–jet is no longer present. The high energy loss used to explain the high p_T suppression can also be used to explain this effect. Because of the high energy loss only jets produced close to the edge of the source make it out of the dense medium, and the back–jet, that has to traverse a large distance through the medium, is quenched during propagation.

Chapter 2

Stopping

In heavy–ion collisions the total relativistic energy and the baryon number is among other quantities conserved. The baryon number is an additive quantum number. It is +1 for qqq systems (baryons B) and -1 for $\bar{q}\bar{q}\bar{q}$ (anti–baryons $\bar{B}$). The net number of baryons is the number of anti–baryons subtracted from the number of baryons $N(B) - N(\bar{B})$. Initially all the energy is carried by the baryons, but after the collision they only carry a fraction of this energy — the baryons have been stopped in the collision. The energy difference has been used to create new particles and generate flow.

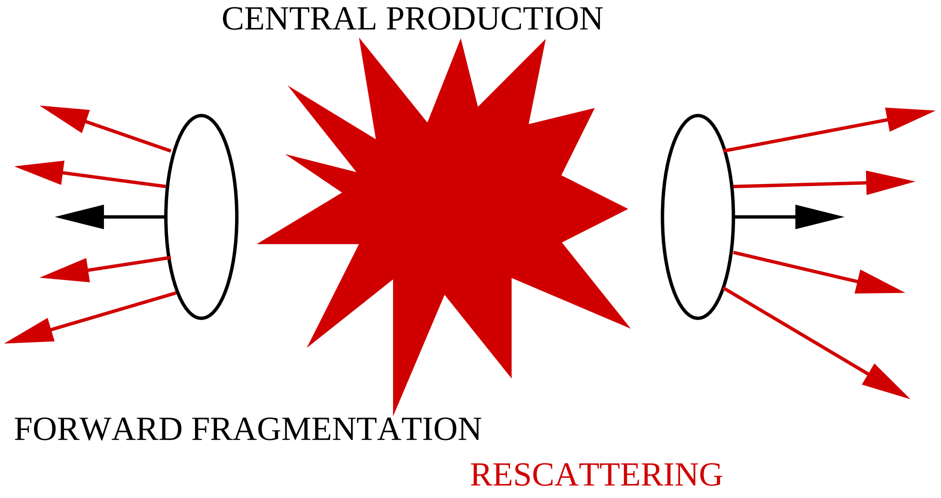

Figure 2.1: A schematic illustration of a collision in the Bjorken picture.

The Bjorken picture (see section 1.3.2) will be used to illustrate how a heavy–ion collision is assumed to proceed at RHIC energies.

When the two nuclei interpenetrate, excited color fields are formed between nucleons which decay to produce particles as they separate forming a hot and dense central region. The nucleons break up in this process (see e.g. Figure 2.11) and most of their fragments end up at forward rapidities. This scenario has been illustrated in Figure 2.1.

The energy loss of baryons occurs in three ways

- **Initial interactions**. The nucleons of the projectile interact with the nucleons in the target.
- **Rescattering**. The momentum and energy of the baryons is modified by elastic and inelastic partonic and hadronic rescattering with created particles leading to further particle production.
- **Decays**. Excited baryons decay and their energy is distributed among the decay products.

This stopping plays a very significant role in heavy–ion collisions since the energy that is available to form the hot and dense zone to be studied is determined by it, and it provides information on the initial interactions between the nuclei.

In the next sections it will be explained how to quantify stopping and an overview of the available experimental data from lower energies will be given. Finally theoretical models and their predictions for experiments at the RHIC will be discussed.

2.1 How to quantify stopping ?

There are two extreme cases that will be used to define maximal and minimal stopping. In the ideal case of full stopping the baryons loose all their kinetic energy in the collisions. In the ideal case of full transparency the baryons loose none of their kinetic energy.

In this thesis the measured rapidity shift will be used to quantify the stopping as was done in the review of stopping in heavy–ion collisions by Videbæk and Hansen from 1995 [17]. Based on the measurement of the final state net–baryon rapidity distribution over all rapidities the average rapidity of the baryons in the interval between mid–rapidity and beam rapidity is calculated.

The average rapidity loss $\langle \delta y \rangle$ is then defined as

$$\langle \delta y \rangle = |y_p - \langle y_b \rangle|, \tag{2.1}$$

where y_p is the incoming projectile rapidity and $\langle y_b \rangle$ is the mean net–baryon rapidity after the collision calculated in symmetric collisions as

$$\langle y_b \rangle = \int_{y_m}^{y_p} (y - y_m) \frac{dN_b(y)}{dy} dy + y_m, \tag{2.2}$$

where $dN_b(y)/dy$ is the net–baryon rapidity density and y_m is the rapidity of the CM in the LAB frame. If $\langle \delta y \rangle = |y_p - y_m|$ then there is complete stopping and if $\langle \delta y \rangle = 0$ there is full transparency.

In collisions of asymmetric nuclei, the measured rapidity density dN/dy is usually not symmetric around mid–rapidity and it is important to differentiate between net–baryons from the projectile and target. This is more difficult and not relevant in this thesis which deals with $Au + Au$ collisions.

The rapidity loss is invariant under Lorentz transformations along the beam axis (boost invariance) and is independent of the absolute scale of the rapidity densities. The important result found by Videbæk and Hansen and later confirmed by other experiments is that the relative rapidity loss ($\langle \delta y \rangle_{rel} = \langle \delta y \rangle / |y_p - y_t|$, y_t is the target rapidity) is independent of beam energy for a given collision system and given centrality as will be shown in the next section.

The task for the experimental physicist is to measure and characterize the dN/dy distributions of baryons and anti–baryons after the collision and from those deduce the net–baryon distribution.

The BRAHMS experiment is designed to measure charged particles from mid–rapidity to forward rapidities. Protons and anti–protons can be identified up to $y \sim 3.2$ and the net–proton distribution can be derived from those measurements and related to the net–baryon distribution using different assumptions. The net–baryon distribution over the full rapidity interval can, to a large degree, be inferred when the total number of participants (the number of net–baryons) is known by extrapolation of the rapidity density distribution in the measured rapidity interval ($0 < y < 3.2$) to beam–rapidity $y \sim 5.4$.

2.2 Experimental Data

In the study of heavy–ion collisions it is common to use data from $p + p$ and $p + A$ to establish a baseline for $A + A$ collisions. This makes it possible to see if novel effects are observed in $A + A$ or whether nuclear collisions can be described as a superposition of $p + p$ or $p + A$ collisions. The study of the beam–energy dependence can show if new physical processes become important.

Figure 2.2 shows the rapidity distribution dn/dy^* of protons from $p + p$ collisions as a function of $y^* = y_{lab}/y_{beam}$. The most important observation is that the net–proton distribution shows a minimum at mid-rapidity and increases away from mid-rapidity. The graphs for different energies reach almost the same level at forward rapidities, but differ significantly at mid–rapidity. Using equation 2.1 it is clear that some stopping is observed in $p + p$ collisions and the calculated rapidity loss is a little less than 1.0 for all energies. The integral under the dn/dy^* curves yields the proton multiplicity which is practically constant for all energies ($p + p \rightarrow 1.2\ p + 0.8\ n$ after all decays), so the number of protons is not conserved i.e., it is the *baryon* number that is conserved.

When we now turn to $A + A$ collisions it is interesting to study the centrality dependence and the dependence on the projectile and target size, in addition to the bombarding energy

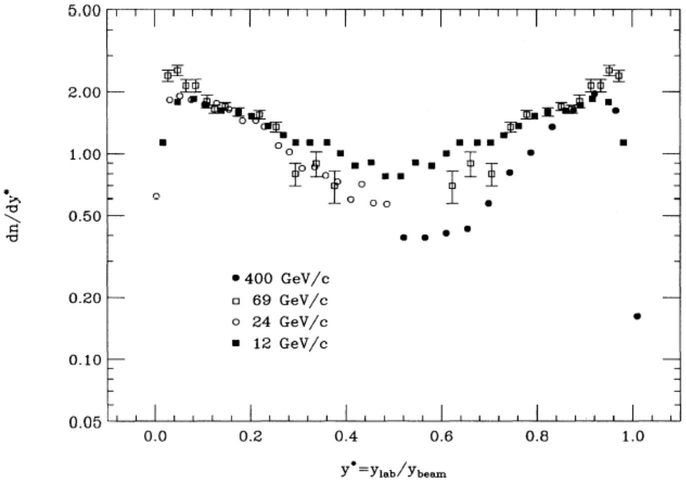

Figure 2.2: The $p + p \to p + X$ scaled rapidity densities dn/dy^* as a function of y^*. The central densities decrease as we go to higher energies i.e., the collision becomes increasingly transparent. The energy is given in the laboratory frame. Figure is taken from [17].

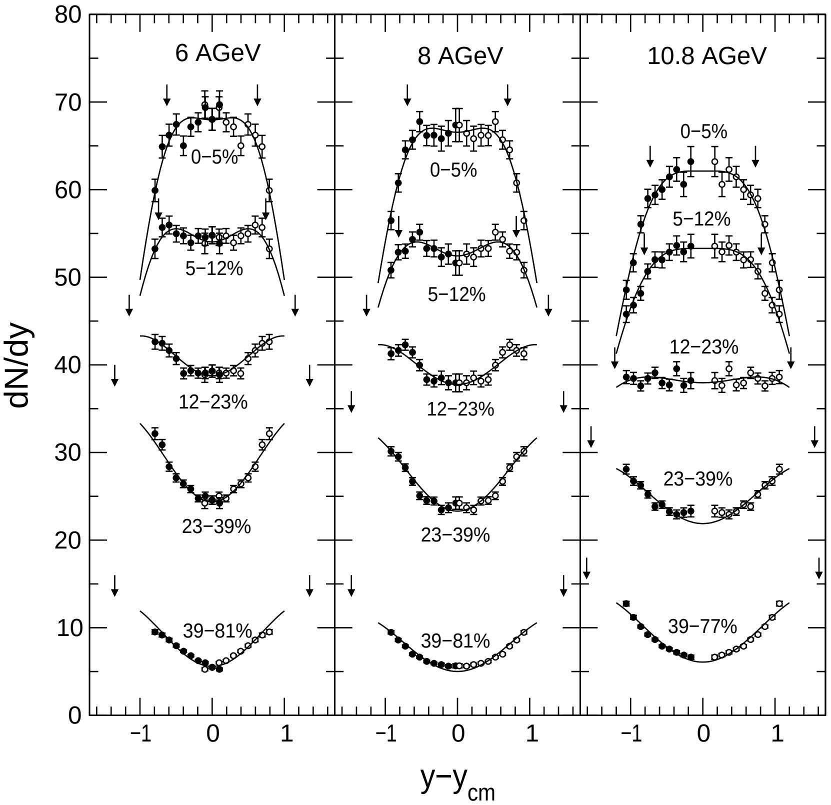

Figure 2.3: Proton rapidity distributions from $Au + Au$ collisions for different beam energies and centrality classes. As the collisions gets more peripheral the distributions resemble the distributions in $p+p$ collisions (Figure 2.2). The curves represent double Gaussian fits to the data, the centroids of which are indicated by the arrows. The figure is taken from [16].

dependence.

In Figure 2.3 results from a study on the centrality dependence of stopping at AGS beam energies are shown. One observes that the dN/dy distributions can be described with a double Gaussian ($\mu_1 = -\mu_2$) at each centrality. The centroids of these Gaussians shift toward mid–rapidity as the collisions becomes more central, so the stopping increases with centrality. In peripheral collisions the shape is the same as in $p+p$ collisions, while the central collision picture is clearly different as most of the protons are transported to near mid–rapidity. This means that in the case of stopping, $A+A$ collisions goes beyond a superposition of $p+p$ collisions. Figure 1.6 shows that the number of binary collisions rises faster than the number of participants going from peripheral to central collisions. In central $Au+Au$ collisions each nucleon on the average experience ~ 3 binary collisions compared to 1 in $p+p$, see Figure 1.6. The multiple binary collisions play an important role in stopping in $A+A$ collisions.

For the most central collisions the distribution is almost flat around mid–rapidity, but the width increases with the energy.

The fact that the distribution can be described by two Gaussians suggests that one of them is associated with protons from the target and the other with protons from the projectile. If this was always the case it would be possible to separate the measured net–protons in a target and projectile component and the average rapidity loss would simply be the mean of the projectile Gauss subtracted from the beam rapidity. Thus the integration from y_m in equation 2.2 could be avoided. Further more it is interesting to note that if the abscissa was e.g. energy, the distribution would not be Gaussian, suggesting that the description of the underlying physics might be especially simple in terms of the rapidity variable.

NA49 has studied the stopping at SPS energies in great detail in $p+p$, $p+A$, and $A+A$ collisions. Figure 2.4 show some of their latest results from [19]. Instead of using the rapidity densities they have chosen to use x_F, defined in equation B.8. It is the dependence on m_T that complicates the comparison of dN/dx_F with dN/dy measurements since there is no direct transformation. Since most of the protons are at low $p_T < 1.5$ GeV, the m_T dependence will be ignored in the following more qualitative discussion of the results, so that small x_F values corresponds to rapidities close to mid–rapidity and large x_F corresponds to rapidities close to beam–rapidity, see equation B.8.

The NA49 experiment has developed a technique to remove the target contribution to the net–proton distribution. By using a pion beam as projectile on the same target, it is known that all measured net-protons comes from the target, since pions are mesons(B=0). The net–proton distribution measured in $\pi+p$ and $\pi+A$ can then be subtracted from the net–proton distribution measured in $p+p$ and $p+A$ to obtain the projectile net–proton distribution. This solves the problem inherent in the asymmetric $p+Pb$ collisions of defining which of the final net–protons comes from the proton projectile.

NA49 has also derived the average number of binary collisions in the target in $p+A$

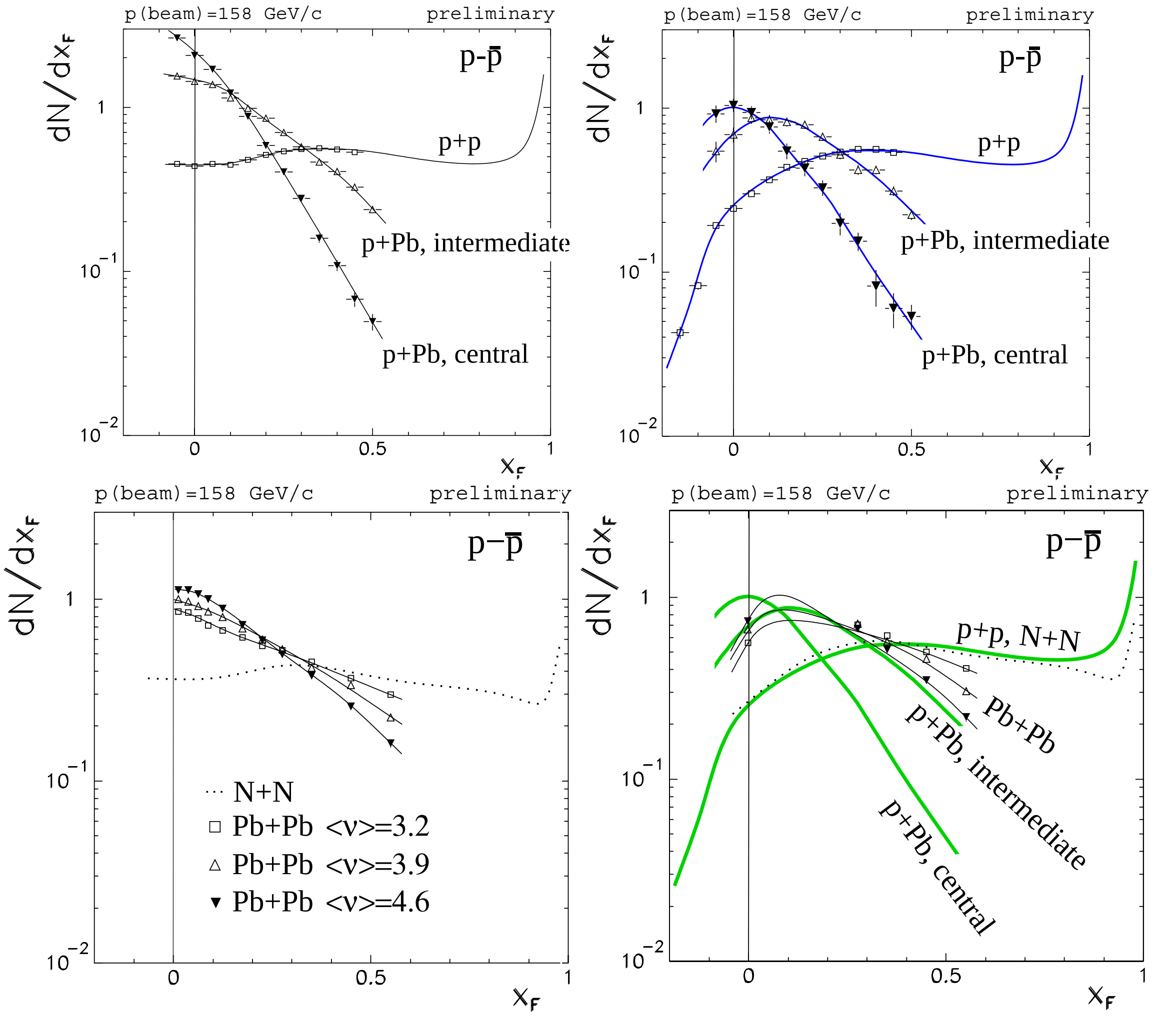

Figure 2.4: Top left: Net–proton distributions in $p+p$ and $p+Pb$ collisions. Top right: The same distribution, but the net–proton production in $\pi+p$ and $\pi+Pb$(target component) has been subtracted. Bottom Left: Net proton distribution in $Pb+Pb$ collisions for different centralities (ν is the average number of collisions from the VENUS model). Bottom Right: The target component has been subtracted and all the data is compared. All figures are from [19]

collisions by measuring the number of *gray* protons i.e., slow protons with lab momentum in the range of 0.15 to 1 GeV/c that have been knocked out of the target. The number of *gray* protons depend on the number of binary collisions and can therefore be used to separate central $p+A$ collisions from peripheral collisions.

Figure 2.4 shows the measurements of net–protons for the many different systems. The stopping in central $Pb+Pb$ collisions is less than in central $p+Pb$ collisions, but much the same as in $p+Pb$ collisions of intermediate centrality. This suggests that the $Pb+Pb$ stopping might be understood from $p+Pb$ collisions. A way to confirm this would be to use a model like the Glauber model to divide the participants in groups according to the number of binary collisions they experience, peripheral (like $p+p$), intermediate (like intermediate $p+Pb$) and central (like central $p+Pb$) and create a superposition of the distributions with the number of participants in each binary collision category as weight. The curve obtained in this way can then be compared to the measured central $Pb+Pb$ data. If the $Pb+Pb$ data can be explained from $p+Pb$ in this manner it would be easy to understand that the stopping is higher in central $p+Pb$ collisions than in central $Pb+Pb$ collisions, because the central $p+Pb$ collisions would then form the subset of the $Pb+Pb$ collisions with the highest degree of stopping.

In Figure 2.5 the beam energy dependence of the rapidity distributions is shown. As the energy increases, a dip develops in the rapidity distribution at mid–rapidity. This indicates that in collisions at very high energies the stopping is not complete even in the most central collisions and that a picture similar to what is observed in $p+p$ collisions eventually will be recovered, as the bombarding energy increases. The collisions becomes *transparent* i.e., most net–baryons are detected at forward rapidities after the collision, away from the central production at mid–rapidity as it was assumed in the Bjorken picture, see section 1.3.2.

If the relative rapidity loss $\langle \delta y \rangle_{rel}$ is evaluated in central collisions at different beam energies an independence of beam energy is observed for a given collision system and centrality, see Figure 2.6. This is quite amazing since this means that the stopping is proportional to the projectile rapidity which grows *logarithmically* with bombarding energy, see Figure 2.7, whereas for stopping of charged particles in atomic matter, the energy loss dE/dx saturates at high energies. The observation that the stopping in central collisions follows $\langle \delta y \rangle_{rel} \approx 0.32$ allows the prediction that at RHIC the rapidity loss will be $\langle \delta y \rangle \approx 3.4$ [17], which can be tested with the BRAHMS detector.

For the relative rapidity distribution the maximal stopping is $\langle \delta y \rangle_{rel} = 0.5$ and full transparency is $\langle \delta y \rangle_{rel} = 0.0$. This definition of the maximum stopping and transparency makes it unlikely that it will ever be attained. Even if the baryons should loose all kinetic energy in the initial collisions, they are likely to scatter with some of the produced particles and retain some kinetic energy. The rapidity distribution of produced particles (e.g. pions) at low energy can be reasonably described with a thermal distribution. If the completely stopped

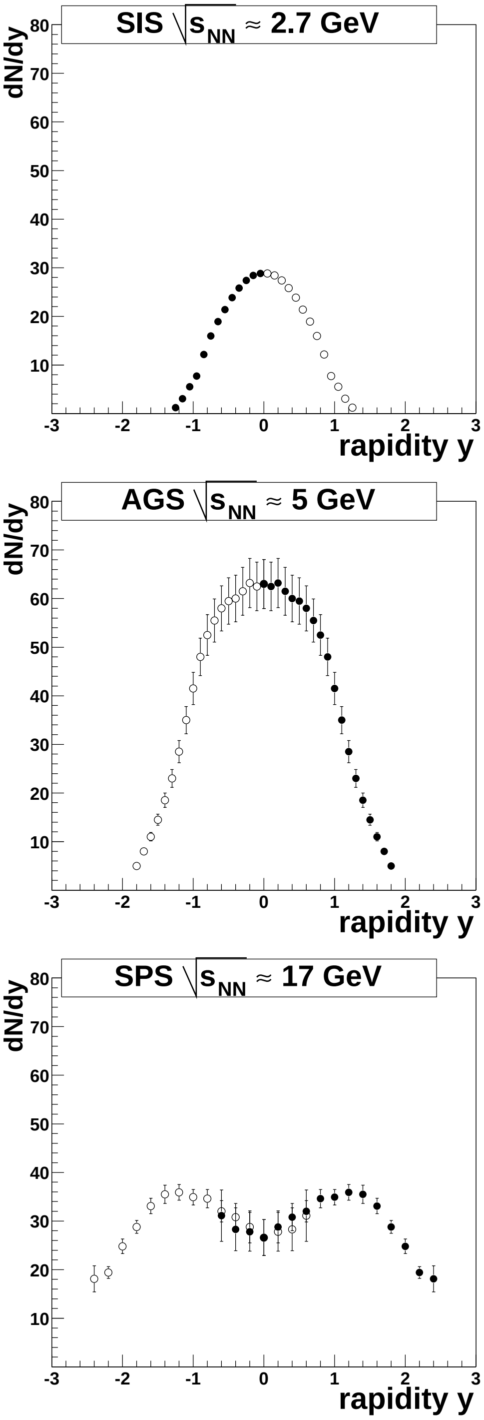

Figure 2.5: The energy dependence of the rapidity distributions for the most central collisions. As the beam energy increase the rapidity distribution broadens and finally seems to separate in 2 well defined peaks at SPS energies. SIS data (top) is central $Ni + Ni$ collisions [20], AGS data is central $Au + Au$ read of from plot in [21] (and errors are guesstimated to 8%), SPS data are central $Pb + Pb$ from [22]. The measurement at RHIC energy will be presented in this thesis.

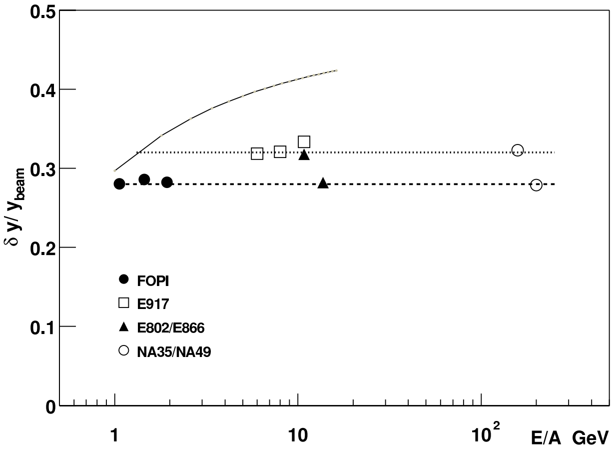

Figure 2.6: The average rapidity loss measured at different beam energies for different colliding systems. The two lines are drawn to guide the eye and the top one is close to the data points for large systems ($Au+Au$ and $Pb+Pb$) while the bottom one is close to the points for small collision systems ($Ni+Ni$ (FOPI), $Si+Al$ (E802), $S+S$ (NA35)). The long–dashed curve corresponds to the expectations from an isotropic Boltzmann distribution with temperature $T = 125$ MeV, see text. The figure is taken from [23].

baryons were to equilibrate with the created particles, in the short time before freeze–out they would ideally be described by a thermal distribution with the same temperature. In Figure 2.6 the predictions for a final thermal distribution with temperature $T = 125$ MeV is shown. The plot suggests that rescattering might be very important at low energy, but becomes less important as the bombarding energy increases i.e., at high energies a thermal source corresponds almost to full stopping.

So far the dependence of the stopping on the projectile and target nuclei have been ignored. In Figure 2.6 it can be seen that in collisions of lighter nuclei ($Ni+Ni$, $Si+Al$, and $S+S$) $\langle \delta y \rangle_{rel}$ is smaller than in collisions of heavier nuclei ($Au+Au$ and $Pb+Pb$), indicating the stopping increases with the size of the nucleus. This can again be understood by the difference in the number of binary collisions. In a heavier target nucleus, the projectile nucleons have to traverse a longer path with the same nuclear density as in the lighter nucleus and can therefore make more collisions. The detailed studies by NA49 (Figure 2.5) suggests that it is possible to disentangle the dependence on number of collisions by using different systems and using knowledge of the difference in collision geometry from e.g. the Glauber model.

2.3 Models

The theoretical challenge of modeling heavy–ion reactions is that there is no unique way of describing the hadron–hadron interactions. pQCD can be applied to describe *hard* processes

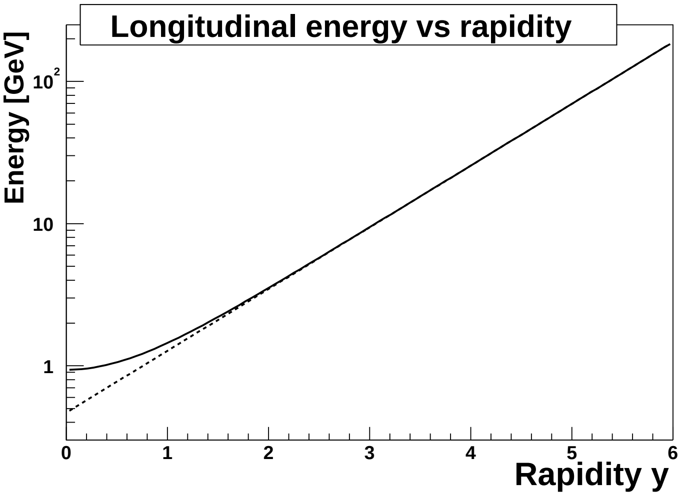

Figure 2.7: The energy of a proton with no transverse momentum as a function of rapidity ($E = m_p \cdot \cosh y$, where m_p is the proton rest mass). The expression approaches the dotted line ($1/2 \cdot m_p \cdot \exp y$) for $y \gg 0$, so the beam energy grows exponentially with rapidity at $y > 2$.

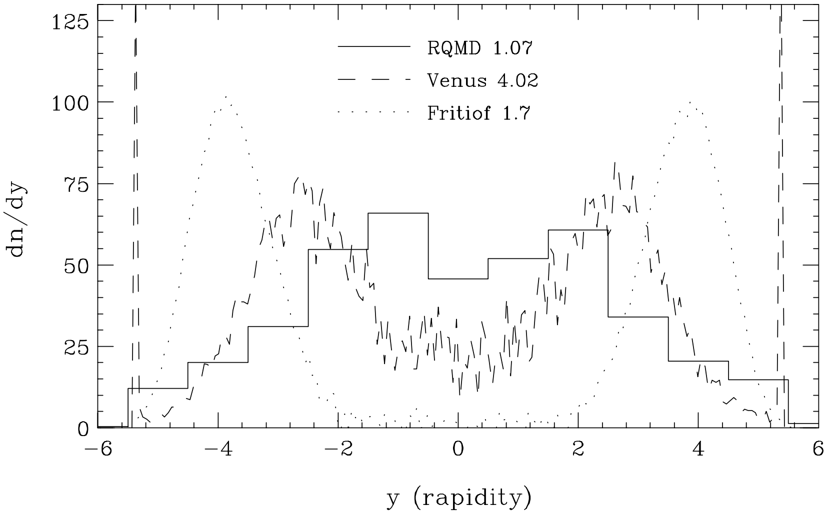

Figure 2.8: Early net–baryon model predictions taken from the BRAHMS Conceptual Design Report.

i.e., processes with a large momentum transfer, but most interactions are *soft* processes even, at RHIC energies, and there pQCD is not valid. Instead the interactions have to be described in terms of phenomenological models. In this section a few of these models will be presented and the physics important for stopping will be discussed.

In terms of stopping the dominant processes are the initial interactions, rescattering, and fragmentation. It has been shown, in the previous section, that nuclear geometry plays an important role in nuclear stopping and particularly the treatment of multiple collisions in the models will be investigated. Important quantities for multiple collisions are the formation time of produced particles and the cross sections for strings and for particles while they are forming (off–shell). For string decays the fragmentation process plays an important part. The fragmentation function describes how the string fragments into hadrons i.e., what particles are produced and especially what fraction of the energy is distributed on baryons compared to anti–baryons.

There are features in the models that are important for predicting the overall number of baryons and anti–baryons that are ignored here, because they have no relevance for net–baryons. This includes baryon-anti–baryon production and annihilation.

There are many models available today. The following three models have been chosen to represent different approaches.

- MCM[24, 25]. Describes only dN/dy distributions of net–protons after the collision. The net–proton distribution is build from fragmentation functions that only depends on the number of collisions. The weight of each fragmentation function is calculated from the collision geometry.

- HIJING[28, 31]. Strings are used to describe all nucleon–nucleon interactions. The strings can be excited or deexcited by multiple collisions. The strings decay after all collisions have taken place using the Lund string model [26] with no rescattering of the produced particles.

- UrQMD[32, 33]. This model is an updated version of RQMD which reproduced data from AGS and SPS quite well. It is a transport code using scatterings $\sigma_{12\rightarrow 34}$ and decays to model the collision. The physics of lower energies are incorporated in the model and there is significant rescattering.

2.3.1 Multi Chain Model

One of the first models used to describe stopping was the Multi Chain Model (MCM) in [24]. The description of the model is taken from [25].

If two nuclei A and B, with N_A and N_B nucleons respectively, collide, the net–proton rapidity distribution is assumed to be given by :

$$\frac{dN^{BA\to pX}}{dy} = r_B W_B \sum_{n=1}^{N_A} P_{B/A}(n) Q_n(Y-y) + r_A W_A \sum_{m=1}^{N_B} P_{A/B}(m) Q_m(y) \tag{2.3}$$

where W_B is the average number of participants in the nucleus B and r_B is the fraction of those that fragment into protons. $P_{B/A}(n)$ is the fraction of the W_B nucleons that interact with n nucleons in A ($\sum_{n=1}^{N_A} P_{B/A}(n) = 1$) and $Q_n(y)$ is the rapidity distribution of the proton after the collision ($\int Q_n(y)dy = 1$). W_B and $P_{AB}(n)$ are both calculated from Glauber theory, see section 1.3.1.

The main assumptions used in equation 2.3 is independence of the fragmentation of the target and the projectile and the lack of rescattering. All physics of the stopping have been separated from the nuclear geometry and are located in the fragmentation functions $Q_n(y)$, which specify the rapidity distribution of a projectile baryon that has suffered n inelastic collisions.

For $n = 1$ the fragmentation function should describe $p + p$ data and it is shown in [25] that $Q_1(y) = k(Y)e^{-y}$ where $k(Y)$ is the beam energy dependent normalization ($\int_0^Y Q_n(y) = 1 \Rightarrow k(Y) = \frac{1}{1-e^{-Y}}$). In the following the normalization is ignored and supposed to happen as the final step i.e. the calculations is done assuming that infinite rapidity loss is possible ($k(+\infty) = 1$) and finally renormalized to the actual rapidity range.

One can derive the expression for $Q_1(y)$ from assuming $dN/dx_F = \text{const}$ which is almost true (see Figure 2.4) and setting $m_T = m$ in equation B.8 :

$$\frac{dN}{dy} = \frac{dN}{dx_F}\frac{dx_F}{dy} = \text{const}\frac{2m}{\sqrt{s_{NN}}}\cosh(y) = \text{const}(e^{-y} + e^{y}) \tag{2.4}$$

where the two exponentials are identified with the target and projectile fragmentation functions.

In the simplest approach where one assumes that the multiple collisions consist of independent $p+p$ collisions with the same fragmentation function ($Q_1(y)$), the next fragmentation function $Q_2(y)$ is :

$$\begin{aligned} Q_2(y) &= \int_0^y Q_1(y1)Q_1(y-y_1)dy_1 \\ &= \int_0^y e^{-y_1}e^{-(y-y_1)}dy_1 \\ &= \int_0^y e^{-y}dy_1 \\ &= ye^{-y} \end{aligned} \tag{2.5}$$

but here the formation time has been ignored. In the MCM the formation time is included in multiple scattering by assuming that the $p + p$ fragmentation function in all collisions following the first is $Q_{mult}(y) = \alpha e^{-\alpha y}$. $\alpha = 1$ corresponds to no formation time, and $\alpha > 1$ results in a reduced rapidity loss because of formation time. α is the factor the cross section is reduced with, see equation 2.8.

The fragmentation function $Q_2(y)$ then becomes :

$$\begin{aligned} Q_2(y) &= \int_0^y Q_1(y1) Q_{mult}(y - y_1) dy_1 \\ &= \int_0^y e^{-y_1} \alpha e^{-\alpha(y-y_1)} dy_1 \\ &= \alpha e^{\alpha y} \int_0^y e^{-(1-\alpha)y_1} dy_1 \\ &= \frac{\alpha}{\alpha - 1}(e^{-y} - e^{-\alpha y}) \end{aligned} \tag{2.6}$$

for $\alpha > 1$ and in general the fragmentation functions for $\alpha > 1$ is :

$$Q_n(y) = \left(\frac{\alpha}{\alpha - 1}\right)^{n-1} \left[e^{-y} - e^{-\alpha y} \sum_{m=0}^{n-2} \frac{1}{m!}(\alpha - 1)^m y^m\right] \tag{2.7}$$

The fragmentation functions are universal. The sole parameter that changes when the collision energy is changed is the cut–off of the functions. All fragmentation functions are set to 0 outside the rapidity interval $[0; Y]$ and renormalized to unity in this interval. This is a problem particularly at low beam rapidities where the cut might remove more than just tails. Fragmentation functions for $\sqrt{s_{NN}} = 200$ GeV are shown in Figure 2.9 for two values of α.

In the approximation of infinite beam rapidity the fragmentation functions gives linear scaling of the mean rapidity loss with collision number n

$$\langle \delta y \rangle_n = 1 + (n - 1)/\alpha \tag{2.8}$$

This reveals exactly how α modifies the behavior of the fragmentation function and shows that this model does not have rapidity scaling of the stopping, since the average rapidity loss is only dependent on the beam rapidity cut–off for a fixed collision geometry.

The only parameter in the MCM is α which was fixed using data in [24] to $\alpha = 3 \pm 1$. In spite of only one parameter, MCM does a very good job of describing $p + p$, $p + A$, and $A + A$, see [25].

Figure 2.10 shows some predictions of the rapidity distributions and rapidity loss calculated in the MCM model [23]. The stopping in the model displays fairly good agreement where there is data. The prediction for RHIC is that the relative rapidity loss should have declined to about $\langle \delta y \rangle_{rel} \approx 0.25$.

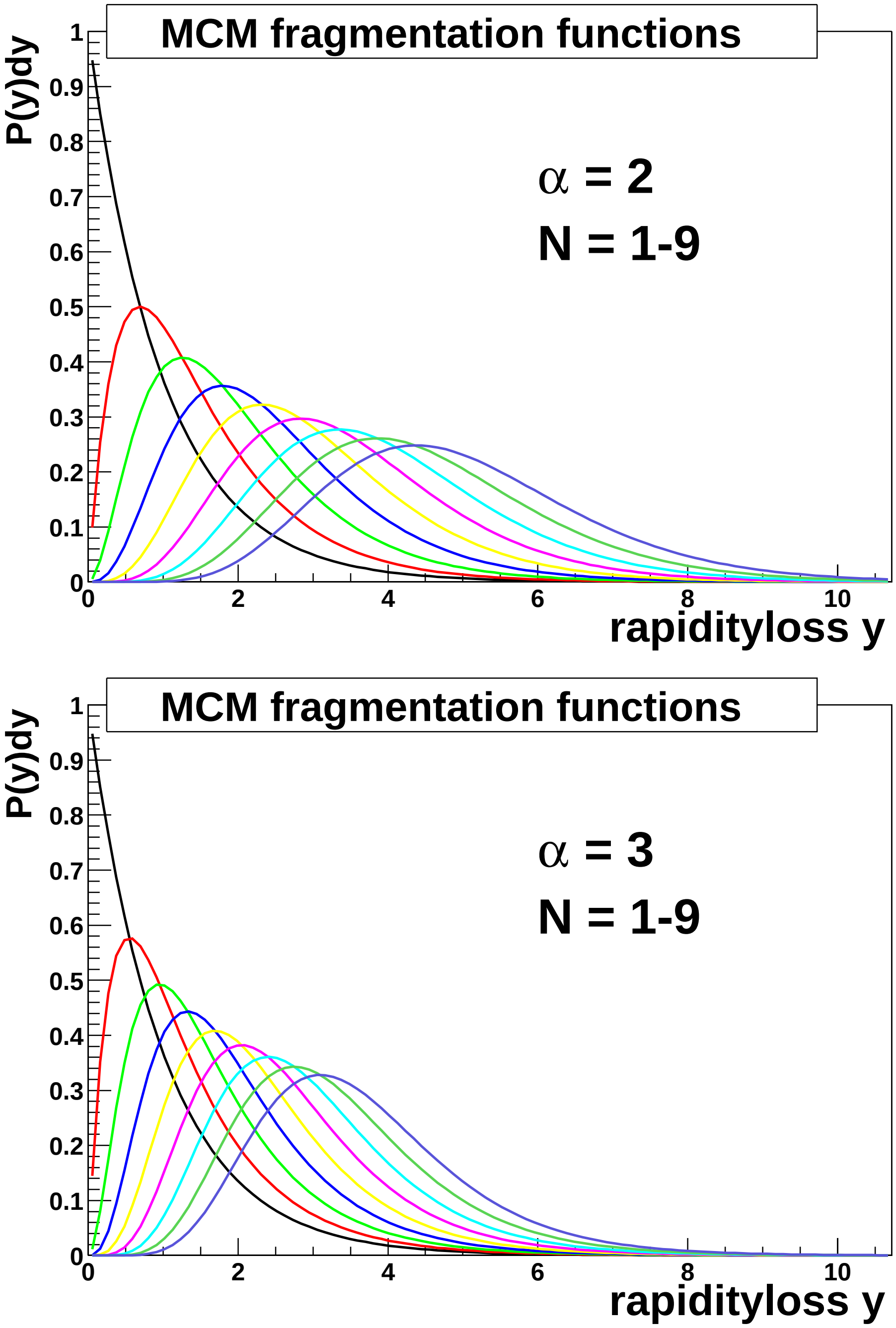

Figure 2.9: The first nine fragmentation functions in the MCM model for $\alpha = 2$ (top) and $\alpha = 3$ (bottom).

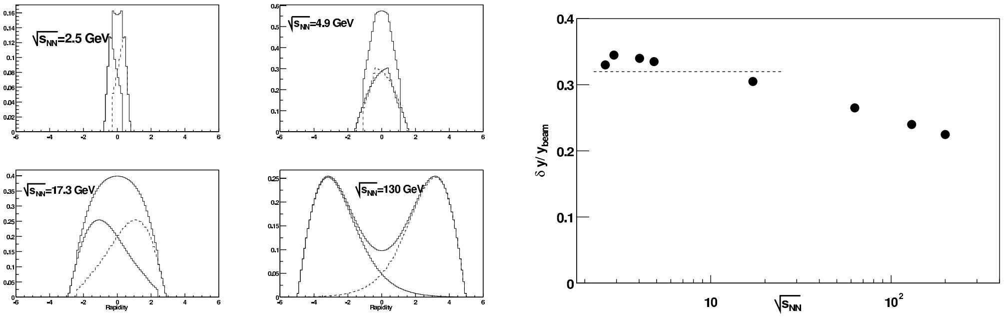

Figure 2.10: Left : Calculated rapidity densities from 4 CM energies using the MCM. The x–axis on all pictures is rapidity y. Right : Predicted energy dependence for the average rapidity loss in the MCM. The dashed line shows the near constant value observed in $A + A$ collisions at lower energies (see Figure 2.6). For both figures $\alpha = 1.3$ have been used at AGS energies and below, and $\alpha = 2.7$ for energies exceeding AGS values. The figures are taken from [23]

2.3.2 HIJING

Heavy–Ion Jet Interaction Generator (HIJING) is a model originally made to include pQCD mini–jet production and quenching in heavy–ion collisions at RHIC energies and above [28]. The success of HIJING was the prediction[1] of the charged multiplicity $dN/d\eta$ at mid–rapidity in $\sqrt{s_{NN}} = 56$ GeV and 130 GeV collisions at RHIC [29].

HIJING uses string fragmentation to model the soft production ($p_T < 2$ GeV/c) in the collisions. The typical interaction in string models are diquark-quark or anti–quark-quark strings, but some models also includes sea–quarks to simulate multiple collisions, see Figure 2.11 where some of the different strings are illustrated as well. In diquark-quark interactions the baryon number stays with the diquark, a single quark from a quark-anti–quark pair is added and the baryon emerges at the front of the collision as the particle with the largest fraction of the energy available (leading baryon), unless some scheme for diquark breakup is employed. The baryon junction, on the other hand, ties the baryon content to the gluonic junction, see Figure 2.11. When the string fragments, each of the gluons break up by quark-anti–quark creation and each of the constituent quarks pick, up an anti–quark and forms three (leading) mesons. In this string mechanism the baryon emerges with a smaller fraction of the energy available so the rapidity loss is larger.

In the HIJING model the number of binary collisions at a given impact parameter is determined from Glauber theory. First the possibility of hard pQCD scattering is considered. After subtracting the energy loss to hard scatterings, the soft interactions are calculated from the number of collisions which, in turn, is calculated according to geometric probabilities. In HIJING the first collision of two nucleons creates diquark–quark strings that are assumed to

---

[1] The multiplicity actually vary by a factor of 2 depending on what physical processes are turned on [30], but for the simplest setup (used by PHOBOS) it reproduced the data.

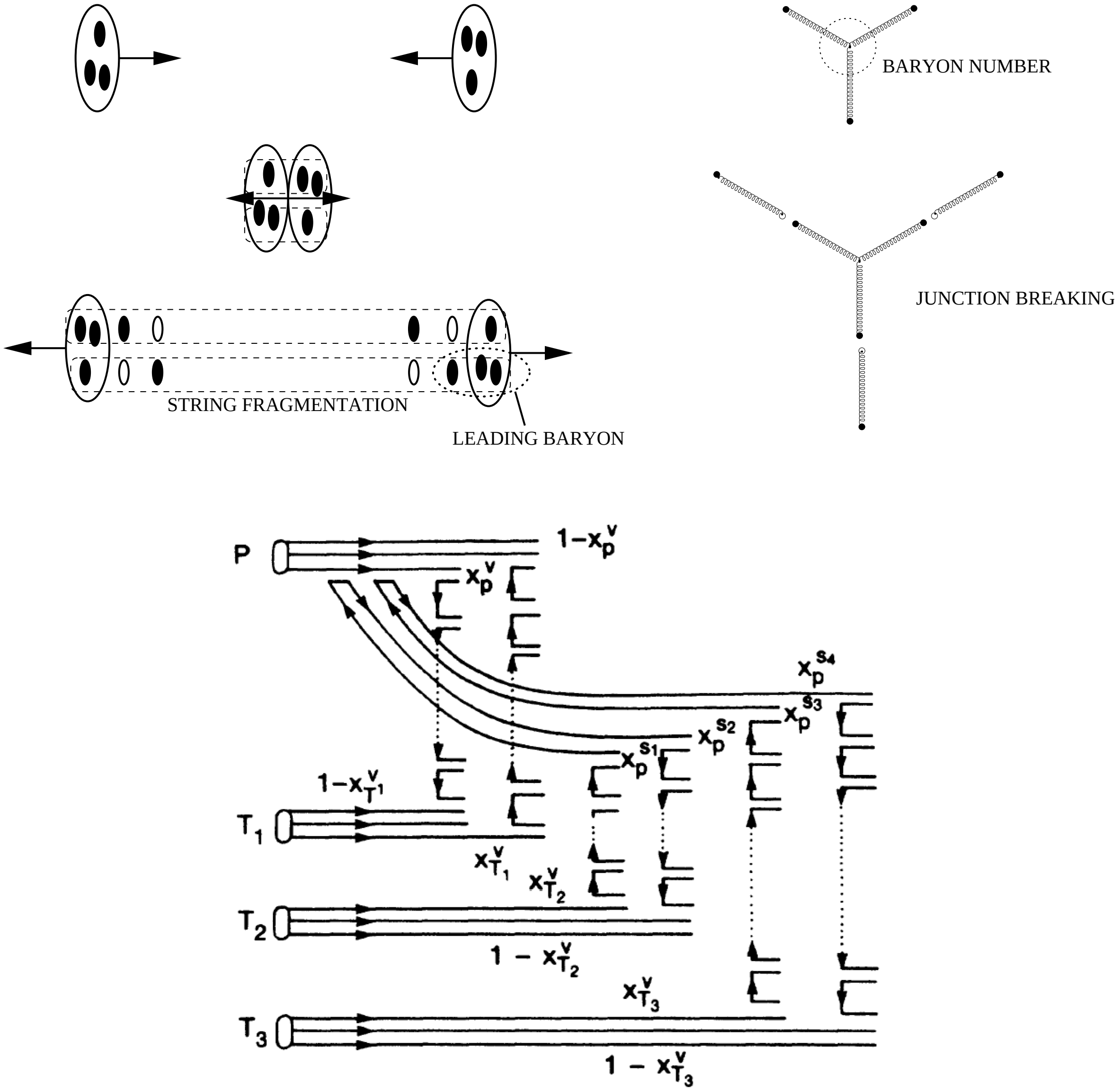

Figure 2.11: Models of string interactions. Top Left: The diquark–quark interaction. The baryon number is carried by the diquark. Top right: The baryon number is carried by the gluon junction. When the strings are stretched the three quarks fragment into three mesons. Bottom: Schematic picture of a single projectile nucleon interacting with three target nucleons through diquark–quark and sea–quark–diquark interactions. The last Figure is from [27].

decay with time–scales larger than the collision time. These wounded nucleon strings can interact in the same way as nucleons with other nucleons or strings, but the probability of exciting them further or deexciting them is modified. After the collision the strings then decay and the produced particles are free i.e., there is no rescattering.

In a later version of HIJING [31], baryon junctions were included to increase the stopping. In Figure 2.12 the predictions for the rapidity shifts are shown for HIJING with and without baryon junction. It is clear that if the fragmentation scheme is altered it is possible to increase the stopping in the collisions.

It is not clear to this author whether HIJING gives rapidity scaling or not at lower energies. The rapidity loss for net–protons derived from the calculations in Figure 2.12 is $\langle \delta y \rangle = 1.92$ for the standard version and $\langle \delta y \rangle = 2.76$ with baryon junction.

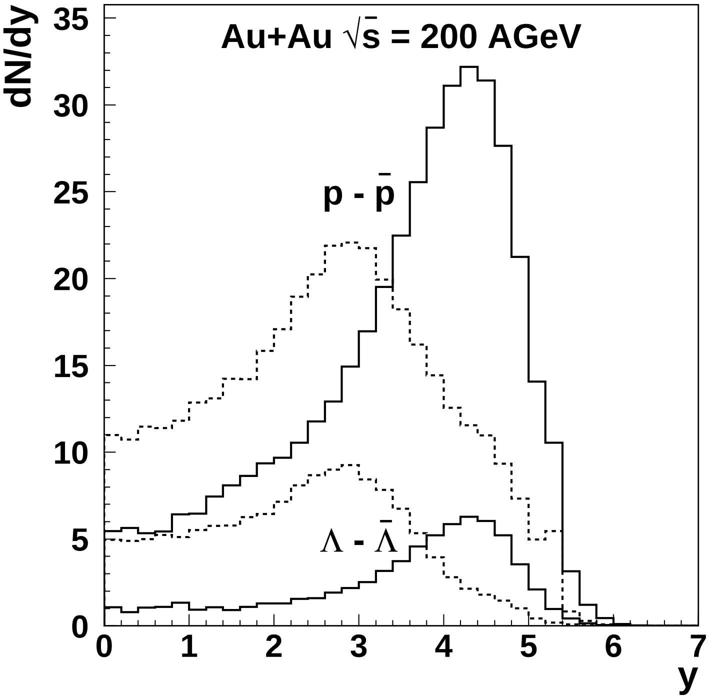

Figure 2.12: Predictions from HIJING for rapidity distributions of net–protons and net–lambdas. The solid (dashed) line is without (with) the baryon junction mechanism. The figure is taken from [31].

2.3.3 UrQMD

The Ultra–relativistic Quantum Molecular Dynamics (UrQMD) model has the ambition of describing the physics of all p+p, p+A, and A+A collisions from SIS energies ($\sqrt{s_{NN}} = 2$ GeV) to RHIC energies ($\sqrt{s_{NN}} = 200$ GeV) [32, 33]. UrQMD is based on transport theory, and hence not only produces the final state hadrons and their momentum distribution like HIJING, but it also follows the evolution of the collision in space and time and has the full phase space information of the particles at freeze–out. This is important in the estimation of HBT radii, nucleon coalescence, and other observables where the space–momentum correlations (flow) are important.

In UrQMD all particles propagate as free particles (straight trajectories) between scatterings and are not modified by the dense medium. Only decays and scatterings like $A + B \to C + D$ are included. Two particles scatter if $d < \sqrt{\sigma_{TOT}/\pi}$ where d is the impact parameter of the two particles and σ_{TOT} is the total cross section. The cross sections are either tabulated, parameterized or extracted from other cross sections using general principles. If a scattering does take place it always takes place at the point of closest approach and the nature of the scattering is decided by a Monte–Carlo. All calculations concerning the scattering are done in the center of mass frame of the two particles. In this way UrQMD steps through a collision in small time–steps keeping track of all particles and applying the correct conservation rules in all scatterings.

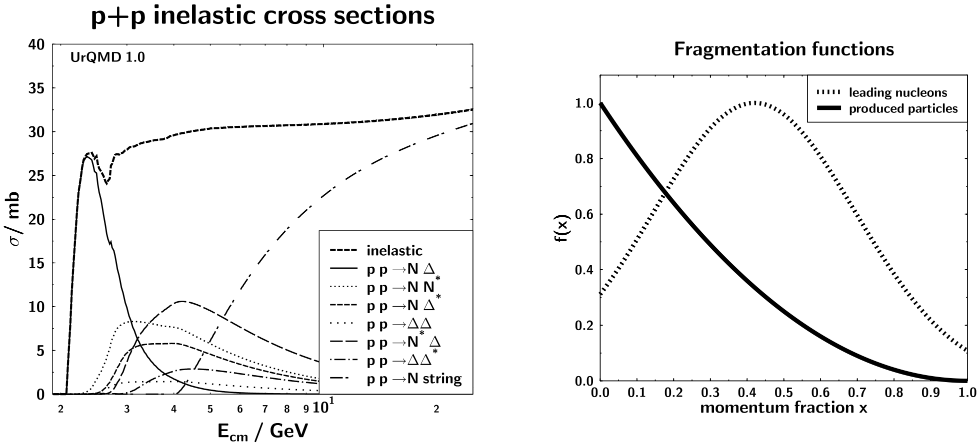

Figure 2.13: Left : Inelastic cross section subdivided into different sub–classes. At high energies string excitation is dominant. Right : UrQMD fragmentation functions for leading nucleons and produced particles. The figure is taken from [32].

One of the most interesting cross sections for baryon stopping is the $p + p$ inelastic cross section. This is shown in Figure 2.13. At high energies the formation of a string is dominant. In the same figure the fragmentation function for strings in UrQMD is shown. The string decays follow an iterative scheme, string ⇒ hadron + new string. Baryonic strings (di–quark-quark) can interact with other particles. The cross section for the diquark pair that forms the leading baryon in the string, is reduced to 2/3 of the baryonic cross section in the formation time interval, which is on the order of 1-2 fm/c.

The important points for stopping in low energy scatterings ($\sqrt{s} < 5GeV$) is that energy loss and particle production occurs through resonance excitations and decays only (a meson cannot be created directly) and even the build–up of transverse momentum plays a role in nuclear stopping. In high energy scatterings ($\sqrt{s} > 5GeV$) the excitation of color strings and their fragmentation is the dominant mean of stopping. The formation time, where the cross sections are reduced, and the amount of reduction plays a very important role for the stopping as does the string fragmentation function. The low energy physics is still important for rescattering.

It has been suggested that if a QGP is formed the (effective) string tension might increase to 5–12 GeV/fm. In a recent paper [34] the color string tension κ is varied in the UrQMD model from the common value $\kappa = 1$ GeV/c (see section 1.1) to $\kappa = 3$ GeV/c, and the effect on nuclear stopping is examined. It is found that the predicted $\bar{p}/p$ ratios with $\kappa = 1$ are too low compared to the measured, but increase with higher string tension, because the higher string tension enhances the production of heavier quark systems (e.g. strange quarks and anti–baryons). In Figure 2.14 the predictions of the rapidity shifts are shown for the two different string tensions. The major effect of increasing the string tension in terms of stopping seems to be that the formation time is decreased $t_{form} \sim 1/\kappa$. A second effect is that heavier baryon species are enhanced compared to the normal value of the string tension.

If the UrQMD has rapidity scaling or not is unclear, but its predecessor the RQMD did not have rapidity scaling [17]. The rapidity loss for net–protons derived from the calculations in Figure 2.14 is $\langle \delta y \rangle = 2.91$ for $\kappa = 1$ GeV/fm and $\langle \delta y \rangle = 3.25$ for $\kappa = 3$ GeV/fm.

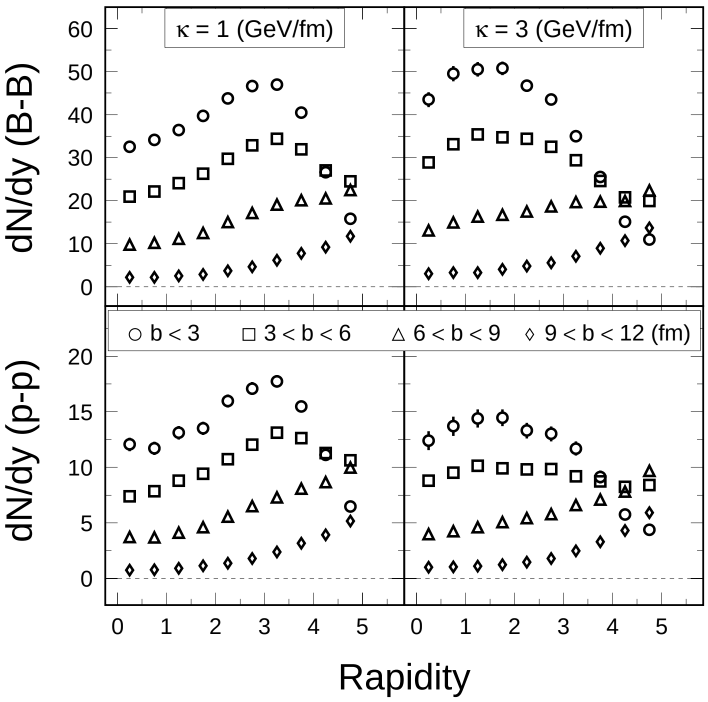

Figure 2.14: Predictions from UrQMD for rapidity distributions of net–baryons and net–protons. The calculations on the left uses a standard string tension ($\kappa = 1$ GeV/fm) and the calculations on the right uses a much stronger string tension ($\kappa = 3$ GeV/fm) that might be valid in $Au + Au$ collisions because of the overlapping color fields. The figure is taken from [34].

Chapter 3

The BRAHMS Experiment

The BRAHMS experiment is located at Brookhaven National Laboratory (BNL) and is one of the four experiments at RHIC. RHIC became operational in the summer of 2000 with Au+Au collisions at $\sqrt{s_{NN}} = 56$ GeV and 130 GeV. In the summer of 2001 RHIC achieved the design energy of $\sqrt{s_{NN}} = 200$ GeV and ran Au+Au collisions for four months. The results presented in this thesis are all obtained with data from this first production run.

3.1 The RHIC accelerator

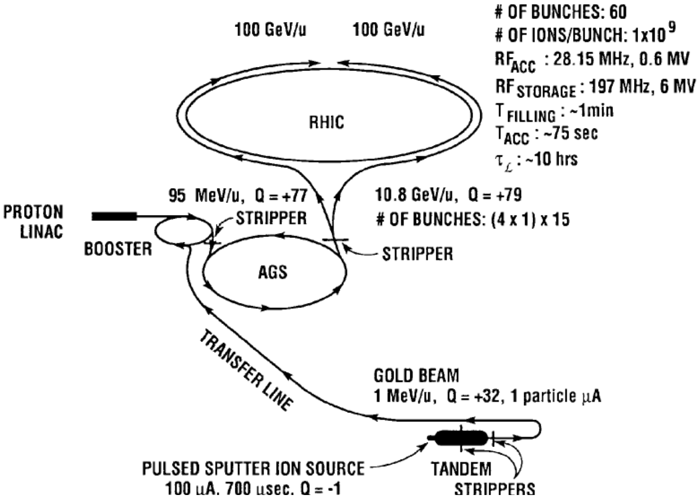

Figure 3.1: Schematic view of the RHIC accelerator complex. The tandem, booster, and AGS, are used to pre–accelerate the gold ions before they enter the RHIC ring.

In Figure 3.1 a schematic view of the RHIC accelerator complex is shown. The old accelerator complex (Tandem, Booster, AGS etc.) is used as a pre–accelerator before the beams are transferred into the RHIC ring where the beams are accelerated to their final energies. There are six experimental halls where the beams can intersect, of which four have been instrumented. The other experiments are STAR and PHENIX both with 300+ physicists, and PHOBOS which is of the same scale as BRAHMS (~ 50 physicists).

RHIC is the first heavy–ion collider in the world. In a collider the center of mass system and the laboratory system can coincide as it does at RHIC for mass symmetric reactions and the full kinetic energy is in principle available for particle production. The RHIC collider has two independent rings which means that in asymmetric collisions, like the d+Au collisions in the current run, the magnets in the two rings can be adjusted to compensate for the different charge to mass ratios so the momentum per nucleon is the same in both beams.

The Au beams at RHIC are designed to be divided in 60 bunches in each ring with $10^9 Au$ nuclei per bunch. The reaction rate R can be calculated as :

$$R = \mathcal{L} \cdot \sigma \tag{3.1}$$

where $\mathcal{L}$ is the luminosity and σ is the cross section. The design luminosity of RHIC is $2{\cdot}10^{26}\,\mathrm{cm}^{-2}\mathrm{s}^{-1}$ which gives a reaction rate of approximately 1200 Hz. Accordingly the reaction rate for a bunch is 20 Hz and, since a bunch makes $\sim 100,000$ revelations per second, the probability for a single interaction is ~ 0.02 %, which implies that the ratio of collisions with two or more interactions to collisions with one interaction is $\sim 0.01\%$, so multiple collisions is not a problem.

The RHIC accelerator complex is described in [35].

3.2 The BRAHMS detector

The BRAHMS detector consists of two magnetic spectrometers that can be rotated in the horizontal plane from $2.3^\circ \leq \theta \leq 90^\circ$ (where θ is the polar angle with the beam line direction) and detectors for event[1] characterization. In Figure 3.2 the layout of the BRAHMS experiment is shown. The requirements for Particle Identification (PID) in very different ranges in momentum at mid–rapidity and forward rapidities led to the design with two spectrometers. The Mid Rapidity Spectrometer (MRS) covers $30^\circ \leq \theta \leq 90^\circ$ and the Forward Spectrometer (FS) covers $2.3^\circ \leq \theta \leq 30^\circ$. The FS has a front part, the Front Forward Spectrometer (FFS) that can be rotated in the full range, and a back part (from T3), Back Forward Spectrometer (BFS), which can only be rotated in the range $2.3^\circ \leq \theta \leq 15^\circ$.

The BRAHMS detector systems has been described in [36], consequently the focus here will be to establish an overview of the reconstruction of event features like centrality and Interaction Point (IP), and tracking and PID with the spectrometers. At the conclusion of the chapter there is a description of the Time Projection Chamber (TPC) clustering and tracking algorithm.

---

[1] Events will in the following be used both in the meaning of a collision and in the meaning of the data recorded for a collision (trigger).

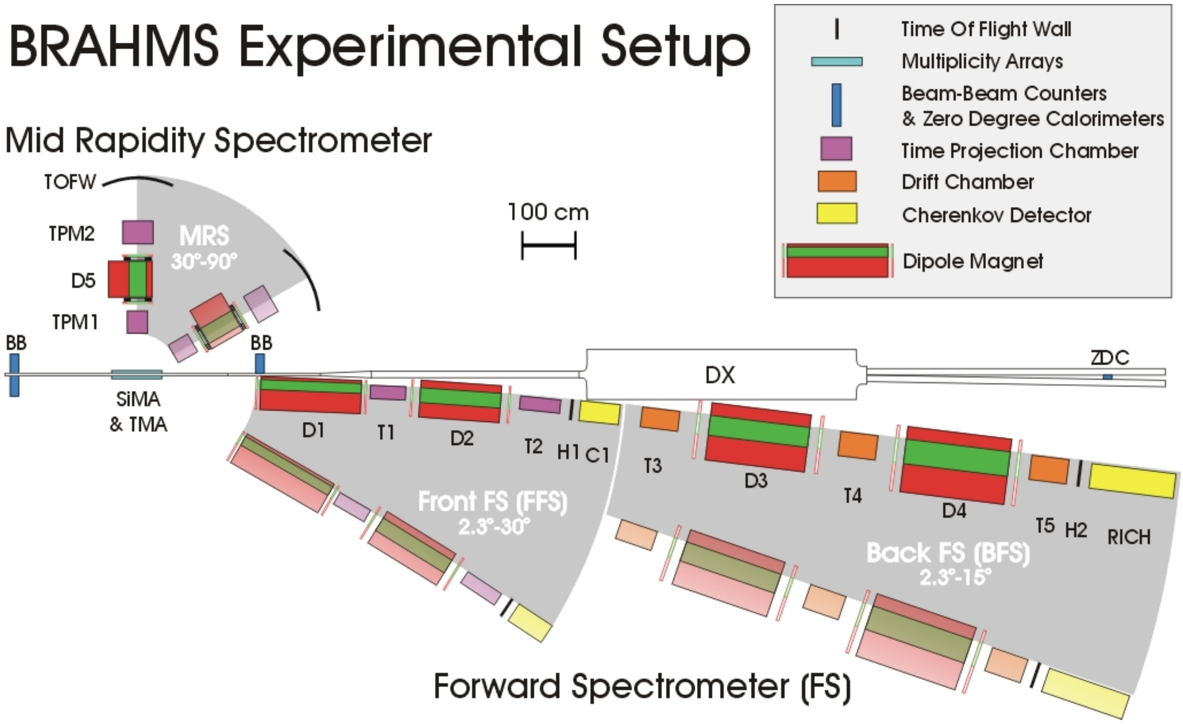

Figure 3.2: Schematic top view of the BRAHMS detector. The range of angular settings are illustrated with the grey shading.

3.3 Global Detectors

The detectors designed to measure features of the events like IP, multiplicity etc. are referred to as global detectors i.e., they measure global properties of the event. The global detectors are the Beam Beam Counters (BB), Multiplicity Array (MA), and the Zero Degree Calorimeters (ZDC). They are all shown in Figure 3.3.

Beam–Beam Counters

At RHIC the beams are parallel when they are brought to collide, so the IP distribution is determined by the longitudinal density of the bunches. The nominal IP is the point where the beams would cross if they had vanishing length. The IP distribution is roughly Gaussian with a width of $\sigma \sim 20$ cm. The IP position is therefore an important quantity to measure event–by–event, because it determines the geometrical coverage of the detectors.

The BB counters are designed to measure the IP of the collision. They consist of two arrays of Cherenkov detectors positioned 2.2 m on either side of the nominal IP. The forward going charged particles produced in the collision ($\beta \approx 1$) emit Cherenkov light that is amplified by Photo Multiplier Tubes (PMT) at the back of the detectors. Two sizes of detectors are used, large (51 mm diameter, 3 cm radiator) and small (19 mm diameter, 4 cm radiator). The time

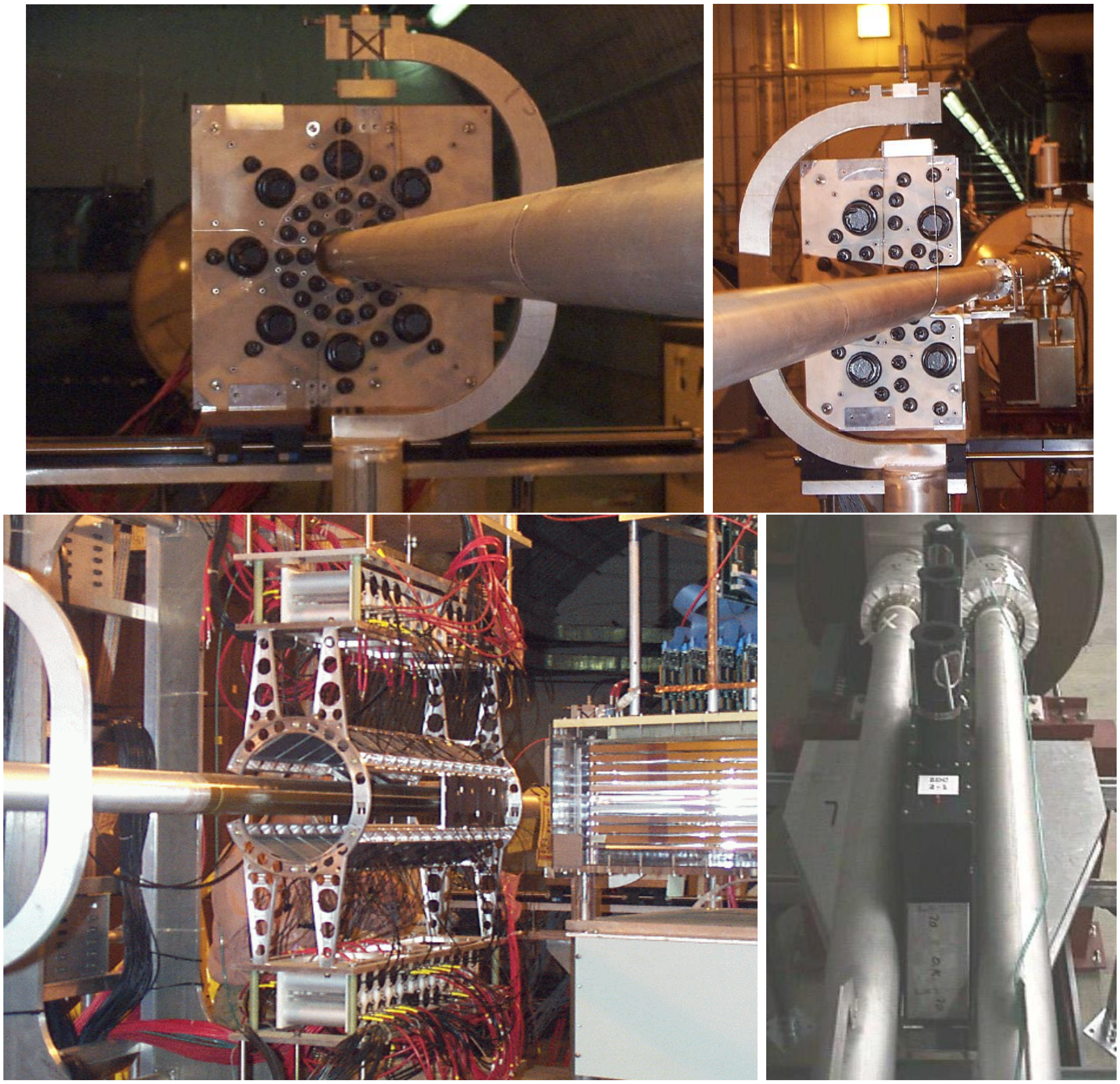

Figure 3.3: Photographs of the global detectors. In the top pictures the BB detectors are shown. Bottom pictures show the MA (Left) and the ZDC (Right).

signals are used to get the IP and as Start Time (T0) for the Time Of Flight (TOF). All the time signals recorded for both arrays are in a 5 ns window. The assumption that the particle travels with the speed of light toward both arrays allows the flight time to be converted into a distance from which the time of the collision T0 and the IP can be determined. The energy signals are used to eliminate noise by requiring signals above threshold. When there are multiple hits in each array, as is almost always the case in central collisions, the time signals for each array can be compared, and the time signals that are far from the others, which presumably comes from slow or background particles, can be removed from the average. In Table 3.1 the three methods for estimating the IP and T0 are explained. The resolution of the IP position is $\sigma_{IP} = 0.7$ cm, and the resolution of the T0 is $\sigma_{TOF} = 65$ ps. Both resolutions depend on the number of tubes used, but is constant for the centrality selection used in this thesis [40].

The energy deposit measured by the BB tubes can be related to the number of charged particles passing through the tubes when the energy deposit of a Minimum Ionizing Particle (MIP) is known and the geometry and the secondary production is corrected for. That way the BB counters were used to measure the multiplicity of primary charged particles as a function of pseudorapidity $dN/d\eta$ at forward pseudo rapidities [37, 38], see Figure 3.5. The design of the BB counters is described in [39], and the reconstruction algorithm is described in [40].

BB IP method	Tubes used
1	Only large tubes
2	Only small tubes
3	Fastest tube

Table 3.1: The IP is estimated in up to three ways using the BB. The best IP determination is obtained with method 2, and the resolution is slightly poorer for method 1. Method 3 only uses the signals in the fastest tubes on either side and is much more prone to background, but also the most efficient. In the analysis presented here method 2 is used if available (99.9% in the centrality selection used) and method 1 is used otherwise (0.1%). If only method 3 is available the event is ignored($< 0.01\%$) [40].

Multiplicity Array

The MA measures the deposited energies of the charged particles traversing the detectors. The MA has good coverage : $-2.2 < \eta < 2.2$, and almost 2/3 of the azimuthal angle. The MA design and software is described in [41]. The energy deposit measured by the MA can be related to the number of charged particles in the same way as outlined above for the BB counters, allowing the full $dN/d\eta$ distribution to be measured (Figure 3.5 [37, 38]). In addition the MA has been used to study event–by–event fluctuations [42, 43]. In the analysis presented

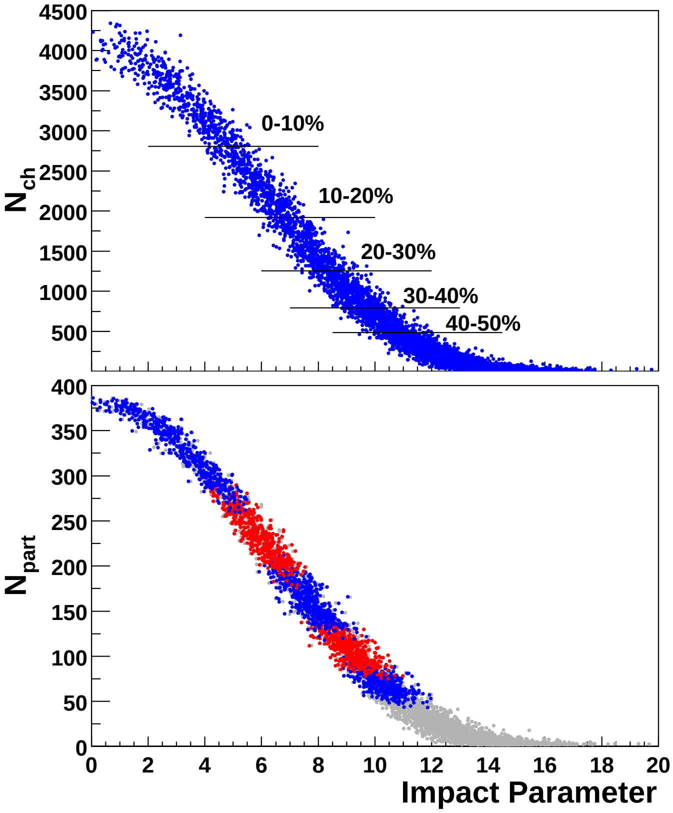

Figure 3.4: The top panel shows the number of charged particles versus the impact parameter in a HIJING simulation. The centrality cuts are applied to the total multiplicity. The bottom panel shows the number of participants and impact parameter selection when these cuts are applied. The centrality cuts are indicated by the different colors of the histogram. The simulation is from $\sqrt{s_{NN}} = 130$ GeV, but the principle is the same at $\sqrt{s_{NN}} = 200$ GeV.

in this thesis the multiplicity obtained from the MA is used to make cuts in centrality, based on the principle shown in Figure 3.4.

Zero Degree Calorimeters

The idea behind the ZDCs was that all RHIC experiments should have one detector in common for characterizing the collisions. The two ZDCs are lead–tungsten calorimeters positioned behind the DX focusing magnets 18 m on either side of the nominal IP. Since the calorimeters are positioned behind the DX magnets, charged particles produced in the collision, with momentum parallel to the beam line, are bent away from the ZDCs, so the calorimeters only measure the energy deposited by stripped spectator neutrons. The ZDCs provide an energy in addition to a timing signal. The timing signals can be used to determine the IP position ($\sigma_{IP} = 2.8$ cm). By requiring that it coincides with the BB IP, events where the IP positions are inconsistent, supposedly because of background signals, can be identified and rejected off-line. The energy signal has been used to study mutual Coulomb dissociation in Au–Au collisions [44]. An interesting difference between inelastic collisions and mutual Coulomb dissociation, is the correlation between neutrons in the two calorimeters. In inelastic collisions, they are strongly correlated (the number of spectators is the same), whereas in mutual Coulomb disassociation events the signals are almost independent. The design of the ZDCs has been described in detail in [45].

In addition to this the ZDCs are used by the accelerator crew to monitor the beam luminosity in the different experimental halls.

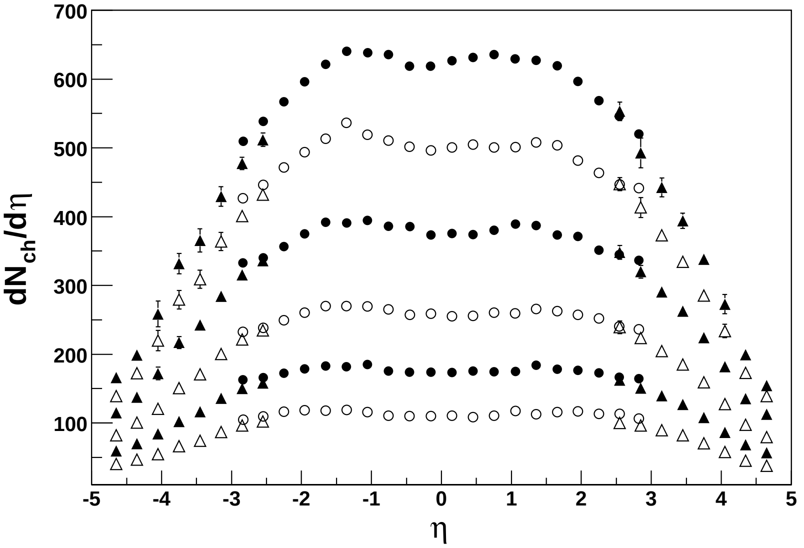

Figure 3.5: The multiplicity of primary charged particles produced in $Au + Au$ collisions at $\sqrt{s_{NN}} = 200$ GeV [38] measured with MA (circles) and BB (triangles). The curves correspond to different centrality selections. From the top it is 0-5%, 5-10%, 10-20%, 20-30%, 30-40%, and 40-50%.

Trigger

All global detectors are part of the trigger system described in Table 3.2. For a majority of the events used for data analysis in this thesis, trigger 6 was required, selecting central collisions in a narrow IP interval. The narrow IP interval was employed to make sure the spectrometer performance was good and the centrality cut ascertained that most events had tracks in the spectrometers and decreased the dead time of the DAQ. The centrality cut limited the study of the centrality dependence to the 20 % most central events in this thesis.

Trigger	Condition
1	BB coincidence $N_L \geq 2$ and $N_R \geq 2$.
2	BB coincidence $N_L \geq 1$ and $N_R \geq 1$.
3	**Multiplicity** trigger TMA — energy threshold ($\sim$ 20% centrality).
4	ZDC coincidence, energy threshold > 25 GeV, and > 4 "hits" in TMA *Minimum bias* trigger.
5	**Vertex** trigger (narrow BB coincidence selecting $-25 <$ cm IP < 20 cm.
6	**Vertex** and **Multiplicity** (trigger 3 and 5).
7	Pulser trigger for pedestal runs.
8	1 Hz synchronization trigger. Can be used for background studies.

Table 3.2: The triggers used in data taking. N_L and N_R is the number of tubes with hits in the left and right BB array respectively. The minimum bias trigger requires signals in the TMA to reject Coulomb dissociation events.

3.4 Tracking Detectors

Both spectrometer arms consist of dipole magnets, tracking chambers, and PID detectors. In this section the reconstruction of the charged tracks will be described.

First, tracking is done in all tracking chambers. The charged particle tracks found in the tracking chambers are called local tracks. Secondly the local tracks are matched across the dipole magnets using simple geometrical constraints and an overall track is identified as a collection of consistent local tracks. From the bending angles through each magnet the momenta p can be calculated.

All the magnets (D1, D2, D3, D4, D5) are dipole magnets with vertical fields. The magnets in the FS, D1–D4, are positioned on the circumference of a circle arc. The D1 magnet is positioned in front of the FFS and bends particles of one charge sign away from the beam–line and into the FFS and particles of the opposite charge sign toward the beam–line and out of the FFS, depending on the field polarity (Polarity A (B) select negative (positive) particles). For a given run the magnets in the FS have the same polarity, and the FS therefore only measures one charge sign in a setting, whereas the MRS can measure both charge signs at a given setting.

The magnets and tracking chambers in the FS have been designed so that the vertical acceptance is limited by the D1 magnet vertical aperture only. D1 also has a trapezoidal block of copper (non–magnetic) inside the gap that is slightly wider at the opening and smaller at the exit to limit the background from particles of the non–preferred charge sign.

Two types of tracking chambers are used, TPCs (TPM1, TPM2, T1, T2) and Drift Chambers (DCs) (T3, T4, T5). In the TPC, charged particles ionize the gas and electrons starts to drift toward the top in the homogeneous electric field inside the box. At the very top the electrons are quickly accelerated toward an anode wire at +1200 V to create a shower,

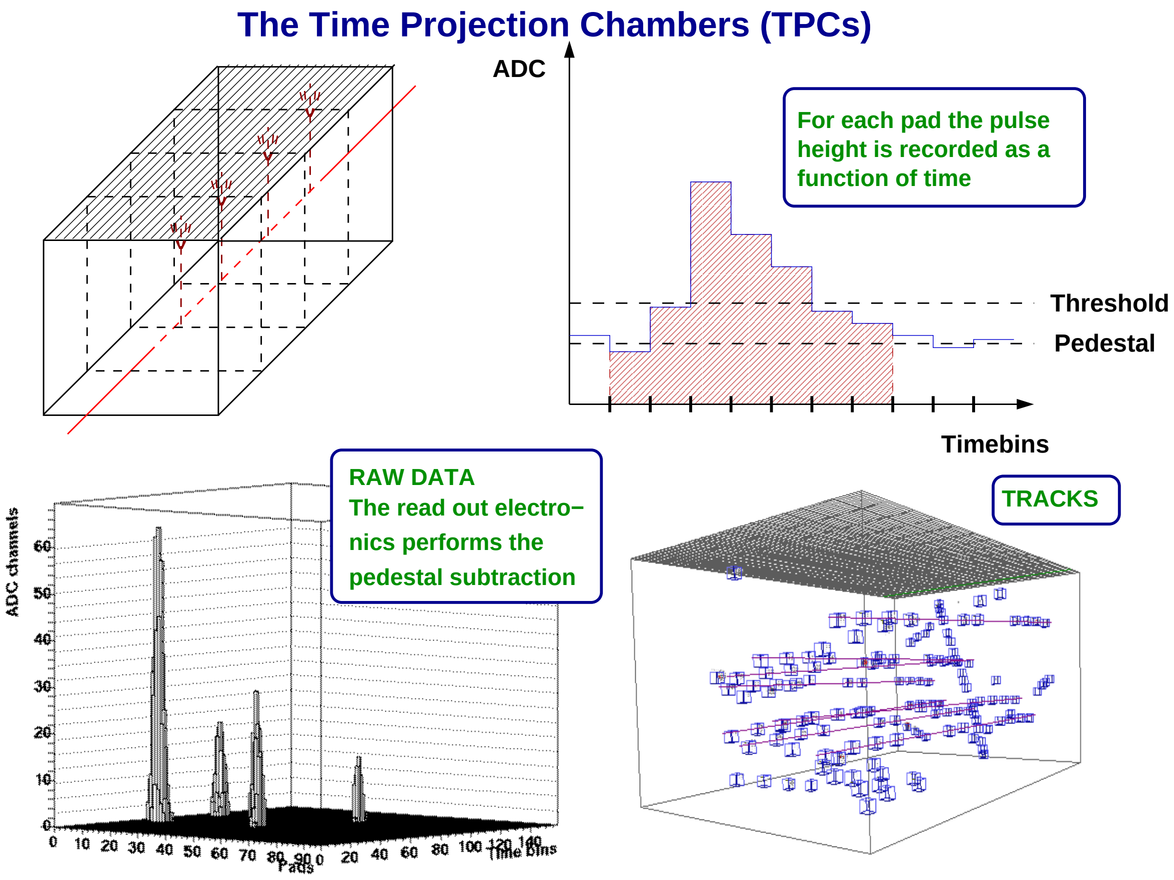

Figure 3.6: As charged particles traverse the TPC the gas is ionized and electrons drift toward the readout plane (Top Left). Each pad measures the deposited energy as a function of time and ADC values are stored when the signal has been above threshold (Top Right). The raw signal distribution in a pad row plane after the on–line pedestal subtraction by the front end cards (Bottom Left). Local hits and tracks in the TPC TPM1 (Bottom right).

and the signal is induced on Cu pads placed on G10 boards located 4.5 mm above the anode wires. The TPC is divided in rows (12–20, 8–12 instrumented) and each row has many pads (96–144). The signals from the pad is connected to a pre–amplifier and shaper circuit and then gated into a switch capacitor array in 100 ns time intervals. When the velocity of the drifting electrons (drift velocity) is constant, the drift time is proportional to the drift distance and the mapping of row, pad, and time gives rise to 3–dimensional space points. The basic principles of the TPC is illustrated in Figure 3.6. The performance and design of the TPCs have been studied in [46].

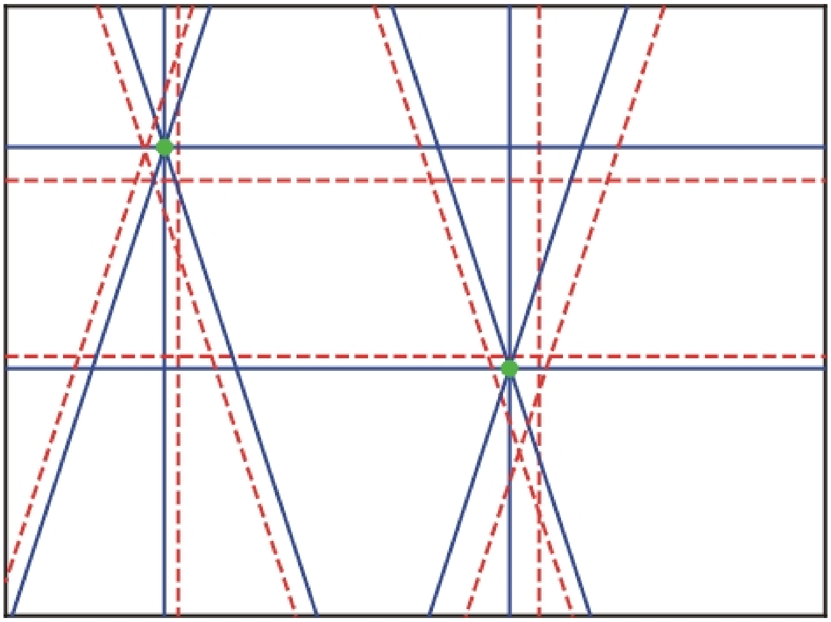

Figure 3.7: Tracking in the DCs in an ideal situation with two tracks and four views. The DC is viewed from the front and the views are x (horizontal), y (vertical), while u and v are angled. Each hit gives rise to two lines in the picture, before the left/right ambiguity is solved, dashed is false and solid is true. The two tracks are defined by the intersection of the solid lines (green dots).

The Drift Chamber (DC)s are wire chambers. Each DC consists of 3 modules with 8–10 planes arranged in 1 of 4 different "views" (azimuthal wire orientation). DCs are gas detectors like TPCs, but rather than a global homogeneous electric field there is a set of anode (+) and field wires (0V) which attract the electrons. When the correspondence between drift time and drift distance to the wire has been established, each hit in a view gives a line parallel with the view direction (wires), however at least 2 planes with the same view are needed to resolve the hit ambiguity i.e., on which side of the wire the charge particle passed. By combining the different views one obtains the tracks as the intersection of the wires that were hit, see Figure 3.7. The design, performance, and tracking in the DCs are described in more detail in [47, 48].

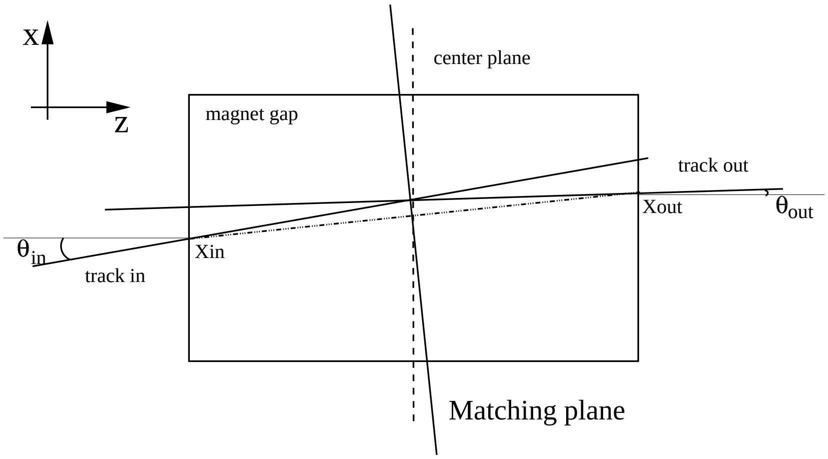

Figure 3.8: The definition of the matching plane. The length and width of the magnet are not drawn to correct scale to make the plot easier to understand.

After local tracking in the TPCs and the DCs, the local tracks in each detector are reconstructed, they have to be grouped and the momentum has to be derived. For all the magnets the *effective edge* approximation is used i.e., the magnetic field outside the physical gap is approximated with the same constant magnitude field as inside, having the same integral Bdl as the measured field. Vertical focusing has been ignored since the effect is very small for the angle of incidence dealt with here. This allows the local tracks in two consecutive tracking chambers to be combined by simple geometric matching in the intervening magnet in the following manner. When the entrance and exit point of the magnet is known for a pair of tracks, a matching plane is centered at the mid–point between the entrance and exit, perpendicular to the horizontal component of a line drawn between the entrance and exit, see Figure 3.8. Each local track is projected (straight line) to the matching plane and the vertical position y, the vertical slope a_y and the polar angle of the track with respect to the matching plane θ is calculated. The tracks are matched in the vertical position($\Delta y = y_2 - y_1 = 0$), the vertical slope ($\Delta a_y = a_{y2} - a_{y1} = 0$), and the angle of intersection with the matching plane ($\Delta Ang = \theta_2 - \theta_1 = 0$). The horizontal ($x$) position is used to define the matching plane and therefore not used as a matching parameter. The matching is done by requiring that all variables are within a 3-σ cut. For each matching distribution the width σ is found by fitting the peak of the raw distribution (without matching cuts) with a Gaussian.

If the tracks match up the momentum can be calculated assuming a unit charge as :

$$p = \frac{Bdl}{(\sin\theta_{OUT} - \sin\theta_{IN})\sqrt{1-\alpha_y^2}} \tag{3.2}$$

where B is the magnitude of the vertical magnetic field, l is the length of the magnet, θ_{OUT} and θ_{IN} is defined on Figure 3.8, and α_y is the averaged vertical slope of the tracks (should be identical). In the MRS D5 is used to determine the momentum, and in the FFS the momentum determined by D2 is used. For the full FS the momentum determined by D4 is used.

In the small angle limit equation 3.2 reduces to $p \approx Bdl/\Delta\theta$, where $\Delta\theta$ is the bending angle, and the momentum resolution is then given as :

$$\frac{\sigma_p}{p} = \frac{\sigma_{\Delta\theta}}{\Delta\theta} = \sigma_{\Delta\theta}\frac{p}{Bdl} \tag{3.3}$$

The angle resolution can be determined from 0–field runs. In the FS D1 is applied a large field to sweep away low momentum particles where multiple scattering might be a problem, while in the MRS tracks are required to point to within a narrow region of the IP and to have a hit in the TOFW to limit the effect of multiple scattering. For the field settings used here typically values of the resolution $\sigma_{res} = \sigma_{\Delta\theta}/Bdl$ are then $\sigma_{res} \sim 0.02$ c/GeV in the MRS, $\sigma_{res} \sim 0.009$ c/GeV in the FFS, and $\sigma_{res} \sim 0.005$ c/GeV in the FS for the settings where H2 is used for PID, and $\sigma_{res} \sim 0.002$ c/GeV for the settings where the RICH is used for PID. In addition multiple scattering plays a role for momentum resolution, see Appendix D.

Tracks in the MRS are required to have TPM1 and TPM2 local tracks. In the FFS, tracks are required to have T1 and T2 tracks, and in addition T4 and T5 tracks are required for a full FS track, but T3 is not required because the efficiency in T3 was very low due to a large background. The DCs are presently much better shielded and the performance of T3 should be better in the next $Au + Au$ run.

Finally the track is projected to find the hit position in the PID detectors. Some photos of the spectrometers are shown in Figure 3.9.

3.5 PID Detectors

Two types of PID detectors are used in the experiment, TOF detectors and Cherenkov detectors.

The TOF detectors H1, H2, and TOFW, see Figure 3.2, are all hodoscopes. They consist of stacked rectangular scintillator slats wrapped in aluminum foil to guide the light and with dark tape working as light insulation. At each end a PMT is attached to read out the energy deposited along with the time signal. When the path length l of the track (from the IP to the TOF slat) is known and the TOF has been measured, the velocity can be calculated as $\beta = l/t$, where $t \equiv$ TOF. Having established the momentum and the velocity, the mass squared m^2 can be calculated as :

$$m^2 = p^2 \cdot (\frac{1}{\beta^2} - 1) \tag{3.4}$$

Due to detector resolution, velocities may be calculated to be greater than the speed of

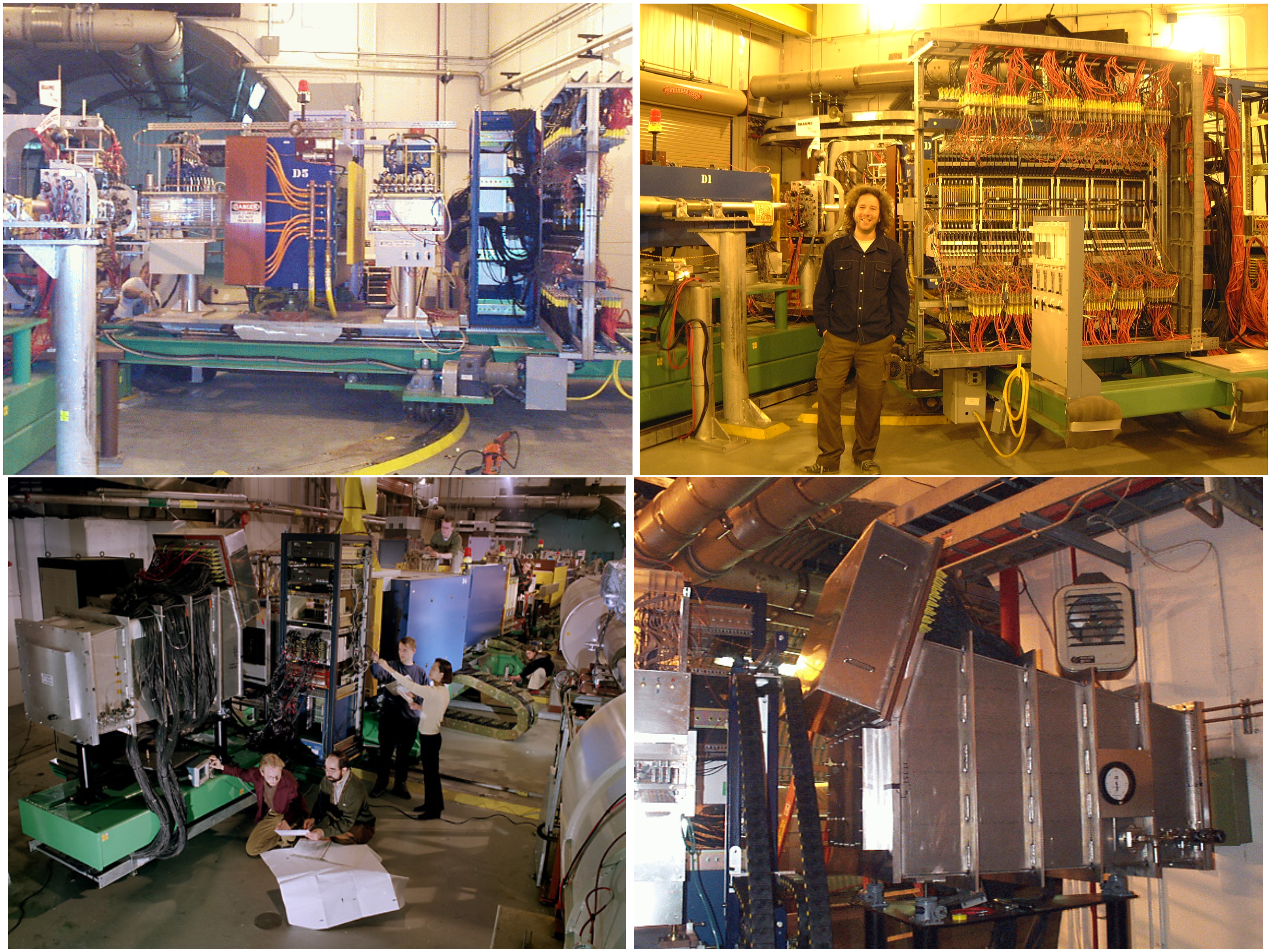

Figure 3.9: The Mid–Rapidity Spectrometer (Top Left). The TOFW seen from behind the MRS (Top Right). The Forward Spectrometer (Bottom Left) and the RICH seen from the side (Bottom Right).

light ($\beta > 1$) yielding a negative mass squared.

In a Cherenkov detector a light shock wave is formed when the velocity of the charged particle exceeds the speed of light in the medium c/n (where n is the refractive index). The angle of emission (Cherenkov angle θ_{ch}) is

$$\cos\theta_{ch} = \frac{1}{\beta n} \tag{3.5}$$

BRAHMS has two Cherenkov detectors. C1 is a moderately segmented Cherenkov (32 tubes). The charged tracks are pointed to the back plane of the detector and correlated with the light collected in the closest tubes. C1 functions as a threshold Cherenkov, meaning that the information obtained is whether the charged particle had a velocity higher than c/n or not. C1 can be used to discriminate pions from kaons and protons (because of the pions lighter mass) when the momentum is above the pion threshold ($p > 3.1$ GeV/c) and below the kaon threshold ($p \sim 9$ GeV/c).

At the back of the FS the Ring Imaging Cherenkov (RICH) is situated, see Figure 3.10. In the RICH the produced Cherenkov light is focused by a spherical mirror at the back of the detector as a circle onto a finely segmented readout plane (320 pixels), and a set of points on a circle may be registered. The radius of the circle is proportional to the Cherenkov angle, so the velocity can be derived from Equation 3.5 and the mass squared can be derived from Equation 3.4. The RICH design and performance is shown in Figure 3.10. The ability to distinguish particle species at very large momenta ($p >$ 4GeV/c and$p <$ 30GeV/c) enables BRAHMS to measure identified particle spectra at forward rapidities.

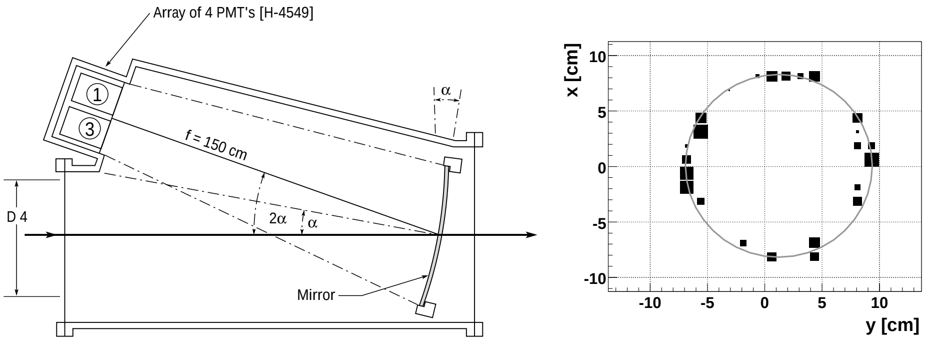

Figure 3.10: Left: RICH design. Right: Ring found in the RICH. The rings are clear and the background is low.

3.6 Acceptance

Both spectrometers have many possible angular and field settings. For a given setting both spectrometers have small solid angle coverage, 6.5 msr for the MRS and 0.8 for the FS.

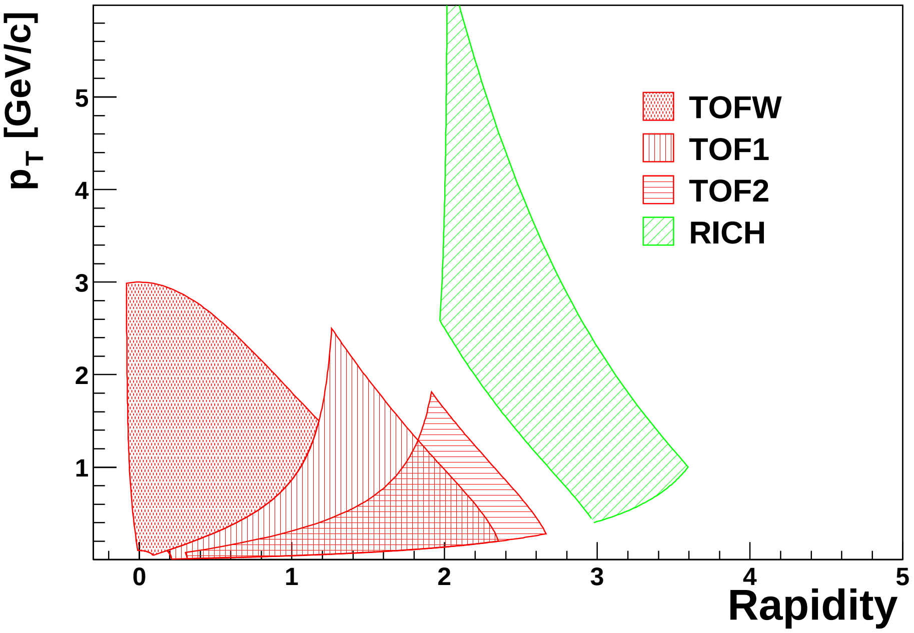

Figure 3.11: The (anti–)proton acceptance for the PID detectors used in this thesis. The acceptance is calculated for protons emitted from the nominal IP and the spread in IP in the data will increase the acceptance slightly. The acceptance of the RICH is shown with a lower momentum threshold of 10 GeV/c, see section 4.1.5.

However, by combining many different settings the phase space coverage is very big because of the polar angle coverage.

The PID capabilities of the spectrometers are designed to match the different requirements at forward rapidity (high momentum, $2 < p < 25$ GeV/c) and mid–rapidity(low momentum, $0 < p < 3$ GeV/c). Consequently π, K and p can be identified for low transverse momenta ($p_T < 2$ GeV/c) over most of the rapidity interval covered by the spectrometers.

Figure 3.11 shows the acceptance of the BRAHMS experiment for protons and anti–protons, based on the performance of the PID detectors. With these detectors it is possible to obtain rapidity densities dN/dy at selected rapidities $0 < y < 3$. The broad rapidity coverage is a unique feature of the BRAHMS experiment. The other RHIC experiments only have good tracking and PID capabilities for hadrons around mid–rapidity ($-1 \leq y \leq 1$).

Subsequently BRAHMS is the only experiment that has the opportunity of studying stopping at RHIC.

3.7 Reconstructing Tracks in the TPCs

This section describes the software and the algorithms used to reconstruct tracks in the TPCs. For each TPC row a charged track ideally has an associated hit. The hit is reconstructed based on the drift–time of the ionized electrons. The signal of the electrons is distributed over more than one pad and time bin. First step in the reconstruction is therefore to group the ADC signals together in clusters. If two tracks are close, clusters may overlap and have to be deconvoluted i.e., separated into two or more clusters. The clusters are then converted to a local hit that is used as input for the local tracking. In this section the details of these steps will be explained in more detail. All C++–classes in BRAT (see Appendix C) are typeset in **bold**.

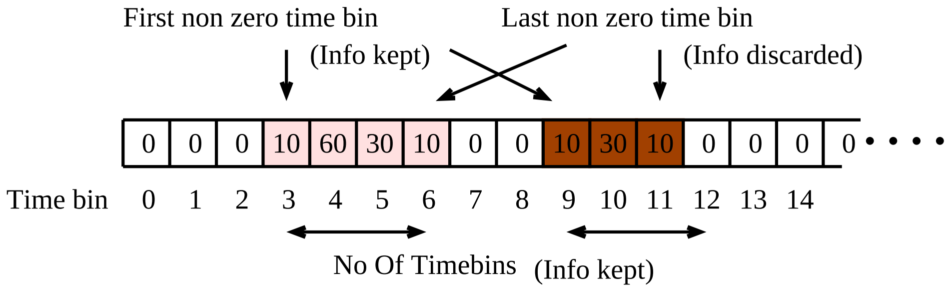

Figure 3.12: Two *ideal* TPC segments. For a given row and pad only the segment with non zero ADC values are kept.

The data that is read out from the TPCs and stored are TPC segments (**BrTpcSequence**). The TPC segment contains the row number, pad number, the first time bin, the number of time bins in the sequence and a pointer to the ADC values. The content of a TPC segment is illustrated in figure 3.12. A segment is created if two or more consecutive time bins have ADC values above pedestal + cut. The ADC values in the two time bins before the signal rise above threshold and two time bins after it drops below threshold. These time bins can have zero and negative values (after pedestal subtraction) and the segments are stripped of these (**BrTpcSequencePPModule**), to make sure there are only strictly positive ADC values in a segment. The segments are finally sorted so that :

$$i < j \Rightarrow (\mathrm{ROW}_i < \mathrm{ROW}_j) \vee (\mathrm{ROW}_i = \mathrm{ROW}_j \wedge \mathrm{PAD}_i \leq \mathrm{PAD}_j). \tag{3.6}$$

3.7.1 Clustering and Deconvolution

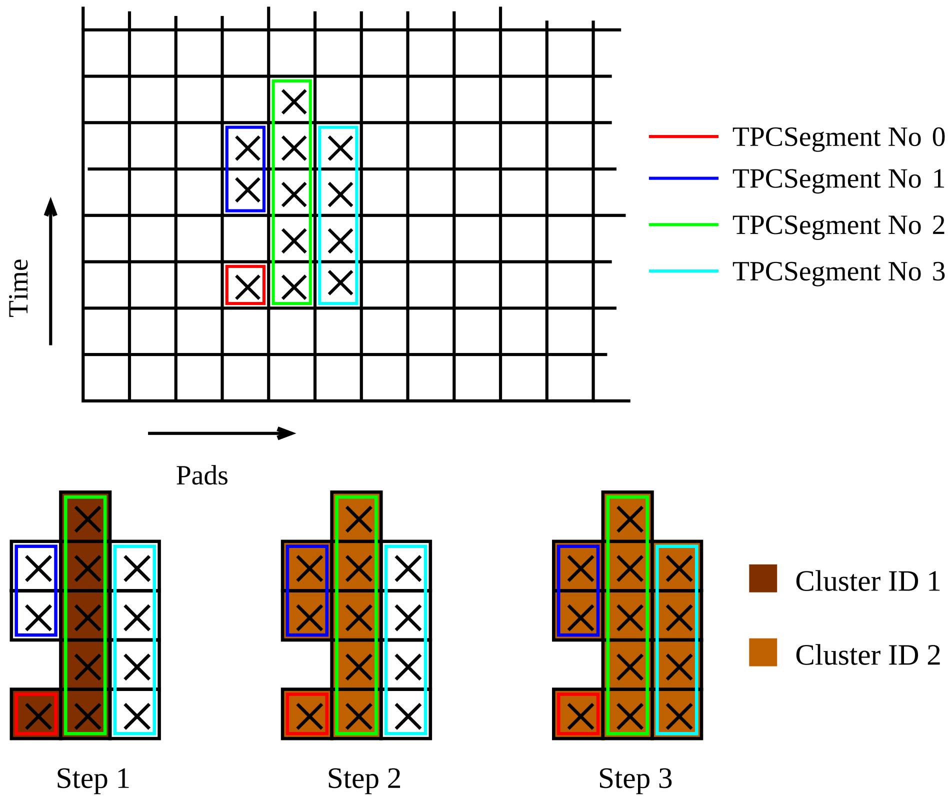

Figure 3.13: Top : A three pad cluster in the pixel array. For each pad in a row, data are stored in segments with continuous ADC signals. Bottom : The cluster in the top picture is built by grouping the segments together. The example is special because there is a hole in the time–bin spectrum, but it illustrates how two clusters are merged and the ID is changed.

The clustering is done in a loop over rows. In a pad-time array the cluster can be visualized as an island, see Figure 3.13. The algorithm for clustering therefore groups all segments that can be connected horizontally in the pad-time array, row–by–row. This is done in a loop over pads and their segments. Each segment is inserted into a new cluster (**BrTpcCluster**) if it is not assigned one already. The next pad is then examined for segments with overlapping time intervals (t_{first}, t_{last}). Any segments found are inserted in the same clusters. If the segment was already a member of another cluster the old cluster is deleted and all segments inserted in the new. The algorithm is illustrated in Figure 3.13. Notice that in step 2 cluster 1 is deleted and the members are inserted into cluster 2.

When the clustering is done the position (mean), width (spread) and energy of the cluster is calculated.

$$\begin{aligned}
\mu_p &= \frac{\sum \text{pad\#} \times \text{ADC}}{\sum \text{ADC}} \\
\sigma_p^2 &= \frac{\sum (\text{pad\#})^2 \times \text{ADC}}{\sum \text{ADC}} - \mu_p^2 \\
\mu_t &= \frac{\sum \text{time\#} \times \text{ADC}}{\sum \text{ADC}} \\
\sigma_p^2 &= \frac{\sum (\text{time\#})^2 \times \text{ADC}}{\sum \text{ADC}} - \mu_t^2 \\
\text{dEdx} &= \sum \text{ADC}
\end{aligned}$$

Each cluster is now assigned a status according to their width (σ_p, σ_t). The shape of the distributions are independent of the pulse height, so fixed cuts ($\sigma_{p,low}$, $\sigma_{p,high}$, $\sigma_{t,low}$, and $\sigma_{t,high}$) are used to identify single hit clusters.

$$\text{Status} = \begin{cases} \text{Noise Cluster} & \text{if } (\ \sigma_p < \sigma_{p,low}\ ) \vee (\ \sigma_t < \sigma_{t,low}\ ) \\ \text{Single Cluster} & \text{if } (\ \sigma_p < \sigma_{p,high}\ ) \wedge (\ \sigma_t < \sigma_{t,high}\ ) \\ \text{Multi Cluster} & \text{else} \end{cases}$$

To remove noise fluctuations, a cluster is considered as noise, if the highest ADC value in the cluster is below a low threshold (less than 10% of the mean).

The clusters with status of multi cluster are deconvoluted using a simple algorithm shown in Figure 3.14. Peaks are identified as the centers of the original clusters. Following this step a new status is assigned to the many sub–clusters. Noise clusters are still thrown away, while hits that remain multi hits are kept. As can be seen from the figure the deconvolution routine is not optimal. If information about the shape of good clusters were used, it might be possible to refine the method. This would be important in an analysis where the two-track resolution is crucial e.g. HBT interferometry.

Finally the position of the cluster (pav, tav) is converted to a local TPC position (x, y) using the pad geometry (x) and the TPC drift velocity (y) (**BrTpcHit**). The resolution of the hit positions have been evaluated by the track residuals and found to be 300–400 μm in

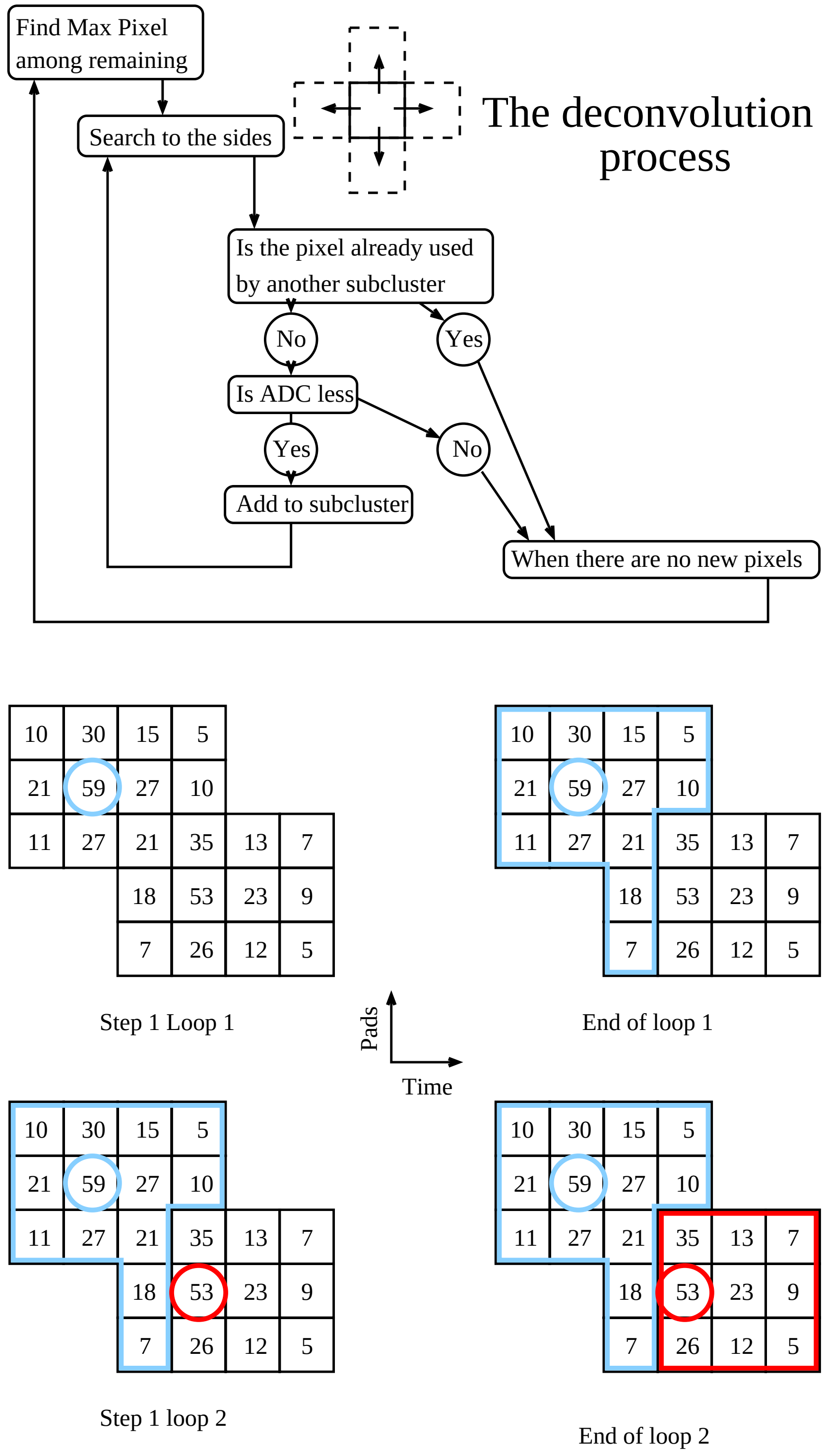

Figure 3.14: Deconvolution. Top: Algorithm for deconvolution. Search to the side of a pixel means comparing to (pad+1, time), (pad-1, time), (pad, time+1), and (pad, time-1). Bottom: An example where two overlapping clusters are deconvoluted according to this algorithm.

x and 400–500 μm in y.

3.7.2 Tracking

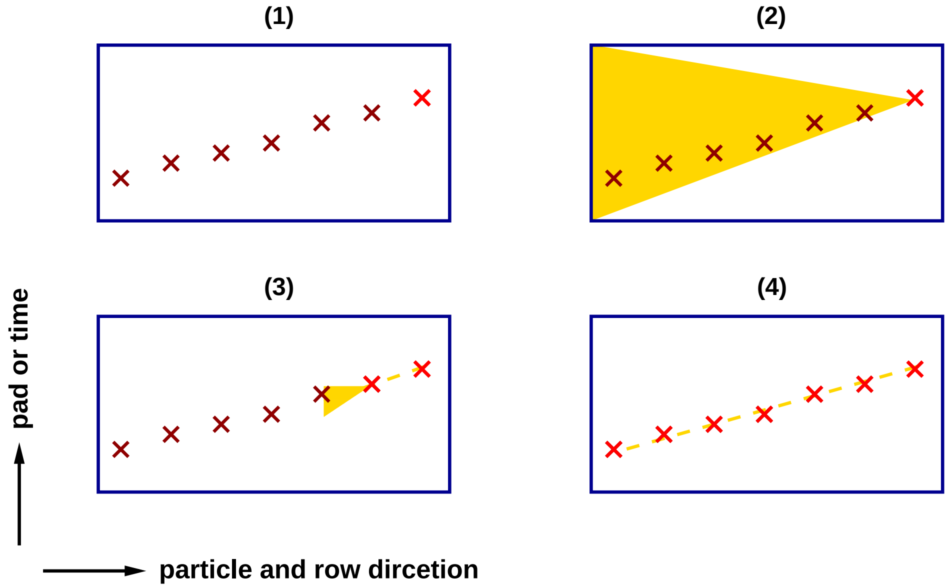

Figure 3.15: An example of how the track finding algorithm works from the back to the front. The search for hits is conducted in a limited area in each row.

The track finding is done with a "follow your nose" algorithm and begins at the back of the detector where the track density presumably is lowest. The principle is outlined in Figure 3.15, and the details are explained below.

The tracking is done in a loop over instrumented rows, starting from the last row. All hits in the back row are assigned as track candidates (**BrTpcTrackCandidate**). For each track candidate the front rows are searched for hits. The track segment is fitted with a straight line which is used to project to the previous row. Hits are then accepted if they fall within a small fixed fiducial cut and the track is refitted. If the track segment contains only one hit, the same local position is used as a guess in the next row, but the search width is broader, covering the entire front of the TPC.

If more than one hit is found, new track segments are created for each of the hits and the tracking algorithm is continued in the next row separately for each segment.

Due to inefficiencies, tracks do not need to have hits in all rows, but are allowed to miss a few rows (typically 2–4). After tracking has been done for the hits in the back row, tracking is therefore continued starting with the hits in the next rows. This is maintained as long as it is possible to have enough hits in a track. Only hits that have not been used in earlier tracks (after the back row most hits will already have been used) are assigned as track candidates.

Following the completion of the tracking, ghost tracks are eliminated by requiring that tracks share no more than half the hits. The tracks that share more than half the hits are grouped (**BrVirtualTrack**) and the track candidate with the least χ^2 is selected.

The best track in each group is fitted with a linear fit and the local tracks (**BrTpcTrackCandidate**) are the final output.

3.7.3 TPC Calibrations

During the work with the clustering and tracking software, calibration software was developed that could identify bad pads, measure the drift velocity, and correct for non–linearities in the drift velocity [49].

The front end read out cards performs the pedestal subtraction on–line. Every 8 hours a calibration run for the TPCs is done. The pedestals are then transferred to the read out cards and thresholds are set.

There are three offline calibrations done.

- **Pad performance**. Pads that are noisy or dead are identified and ignored in the tracking.
- **Drift non-linearities**. The drift velocity in the pad–rows closest to the front and the back, has significant non-linearities that are corrected for.
- **Drift velocity**. Because of pressure changes in the gas the drift velocity changes with time.

The non-linearities in the drift velocity were corrected by studying tracking in the horizontal direction only followed by comparison of the vertical deviations of the hits from the tracks. The non-linearities are largest in TPM2 and smallest in TPM1. There has been a lot of speculation about the possible causes, but so far no cure has been found. The calibration is rather stable and only changes significantly if a TPC has been moved from the platform to be repaired. The vertical dependence of the non-linearities in the drift velocity is the largest and the only non–linearity corrected for. The horizontal dependence has been studied by other collaborators and was found to be largest at the edges of the TPC but no corrections have been applied to the data.

The drift velocity monitors did not work correctly for the data used in this analysis, instead the drift velocity was first calibrated by using several vertical scintillating fibers mounted at the front and back of TPM2, at the front of T1 and at the back of T2. The energy signals in a fiber can be used to select events where it was hit by a charged track. The average position of tracks pointed to the fiber plane over many events can then be compared to the known fiber position and by using several fibers the drift velocity can be deduced. For TPM1 the fibers at the front of TPM2 were utilized. Later when DC calibrations had been carried out

T1 and T2 were recalibrated using DC tracks. The change in the drift velocities with the recalibration was of the order 2–3% and the same resolution of the drift velocity is probably obtained in the MRS.

The vertical resolution of tracks in the MRS and FFS is primarily determined by the linearity and quality of the drift velocity and, as pointed out several points might be refined by spending a lot more time. For longer drift times the problems are in general worse than for shorter because of diffusion and absorption of electrons in the gas.

Chapter 4

Analysis

The goal of this analysis is to determine the multiplicity of protons and anti–protons as a function of rapidity. This will make it possible to measure the shape of the net–proton (net–baryon) rapidity distribution resulting from $\sqrt{s_{NN}} = 200$ GeV $Au + Au$ collisions.

Constructing the invariant yield involves many steps. The methods used in the different steps are almost the same for the MRS and the FS. The procedure can be outlined as follows :

- **Event selection**. Select “clean” events.
- **PID**. Select proton and anti–proton tracks.
- **Efficiency correction**. Correct for detector and software (algorithm) inefficiencies.
- **Acceptance correction**. Correction for the geometrical acceptance of the spectrometers.
- **Other corrections**. Absorption and multiple scattering.
- **Calculate multiplicity**. Combine the above to obtain spectra. Fit spectra and extrapolate to get rapidity densities.

Each of the above steps will be discussed in the following. Finally, systematic errors will be discussed.

In this chapter the momentum axis on most plots have both positive and negative values. Positive values corresponds to positively charged particles, and negative values corresponds to negatively charged particles.

4.1 Data Selection

The event selection and PID will be discussed in this section.

After track reconstruction has been performed (Chapter 3 and [40]) three steps are taken to select the proton and anti–proton tracks. First, events are selected based on global observables (*global cuts*), secondly tracks with bad characteristics within these events are rejected (*track cuts*). Finally the protons are identified based on signals in the PID detector (*PID cuts*).

4.1.1 Event Selection

The selection criteria for clean events are the same for the analysis of data from MRS and FS. Four cuts are applied to select good events.

- Centrality. Events are grouped and analyzed according to the centrality calculated from the MA. Here only the top 20% is studied because of the limitation of the online trigger (section 3.3) used.
- BB method. The fastest tube method has poor resolution and events with only this type of IP determination are rejected (see Table 3.1).
- IP selection. The trigger efficiency limits the IP positions that can be used for analysis.
- ZDC and BB coincidence.

The data set has been divided into three groups according to centrality and the analysis is done independently for each group. The three centrality groups are 0–5%, 5–10%, and 10–20%.

Trigger 6 (described in Table 3.2) is designed to accept only a narrow IP range and becomes inefficient at the edges of this range. This occurs when the distance from the IP to the nominal IP (Δ_{IP}) becomes larger than 20 cm. This trigger was used while collecting most of the data and this limits the analysis to require $\Delta_{IP} < 20$ cm. In the MRS the cut is narrowed further to ±15 cm because it was found in early analysises that the results from data outside this range were inconsistent with results inside this range. The performance of TPM1 is also better for tracks parallel with the pads and the MRS geometry is more sensitive to the IP because it is closer to the IP than the FS.

By requiring that the IP determined by the ZDC and BB coincides, events where background particles may have caused bad timing signals in one of the counters, can be rejected. The distribution of the differences ($z_{BB} - z_{ZDC}$) is Gaussian and a 3σ cut is applied.

4.1.2 Track Selection

The MRS and FS tracks selection is performed similarly. There are two cuts.

- IP cut. The track has to point back to the IP. This is particularly important for protons since there is quite a large background of protons knocked out from detector material.

- Magnet fiducial cut. A fiducial cut is applied on the helix of the reconstructed track to ensure that it does not intersect the magnet iron.

The IP cut is used to remove tracks with an origin that is not from the IP determined by the BB i.e., to remove particles that are not from the primary collision. Tracks are pointed back to the IP (see below) and required to originate within a given distance from the IP. To determine the resolution of the pointing, all tracks are projected back to a plane containing the BB IP. For the MRS, this plane is defined as the $y - z$ plane (see Figure B.1) and for FS tracks the $x - y$ plane containing the IP is used. The use of two different planes is merited by the worsening of the resolution along z as the polar angle of the tracks decreases. In both cases the projections of the tracks are compared to the IPs and the residuals (two dimensions) are fitted with a Gaussian to obtain the means and standard deviations. Finally an elliptical cut was applied to remove secondary and background tracks, see Figure 4.1. The elliptic cut used was 4σ and was chosen so wide to avoid losses due to drift velocity calibration problems, as detailed in section 3.7.3.

In the MRS, the mean and standard deviations are μ_Y, μ_Z, σ_Y, and σ_Z. The resolution in y is determined by the TPM1 track resolution and the resolution in z is dominated by the BB resolution. Typical values are $\sigma_Y \approx 0.4$ cm and $\sigma_Z \approx 0.8$ cm. In Fig 4.3 the distribution of residuals $\sigma = \sqrt{(\delta x/\sigma_x)^2 + (\delta y/\sigma_y)^2}$ as a function of momentum and the effect of the cut on measured anti–protons and protons is shown. It is clear that there are many more protons at large $N\sigma$ than anti–protons for $p_T < 1.3$ GeV. If these protons stem from decays the anti–proton background should be large as well, but since this is not the case these protons are most likely produced in material (beam pipe, air, etc.) and are therefore rejected as background. The pointing cut is seen to be extremely important for measuring the proton yields in the MRS. In the FS only a small difference is observed between anti–protons and protons.

The deviation of the pointing could depend on the momentum because the effects of multiple scattering is worse at low momentum. By comparing the distribution of pointing deviations for different momentum intervals the resolution of the pointing was found to be nearly independent of the momentum, see Figure 4.1. This may be because the tracks are required to propagate all the way through the spectrometer and be properly matched. The background that is removed by the cut has a clear momentum dependence and is largest at low momentum.

In the FS the pointing resolution only depends on the tracking resolution and typical values are 0.6 cm in both horizontal and vertical direction. No significant momentum dependence is observed, see Figure 4.2.

When the local tracks are matched in a magnet (see section 3.4) the tracks are required to propagate through the magnet without getting closer than 1 cm to the side of the magnet gap (fiducial cut). The effect of this cut is shown in Fig. 4.4 for the D5 magnet in the MRS.

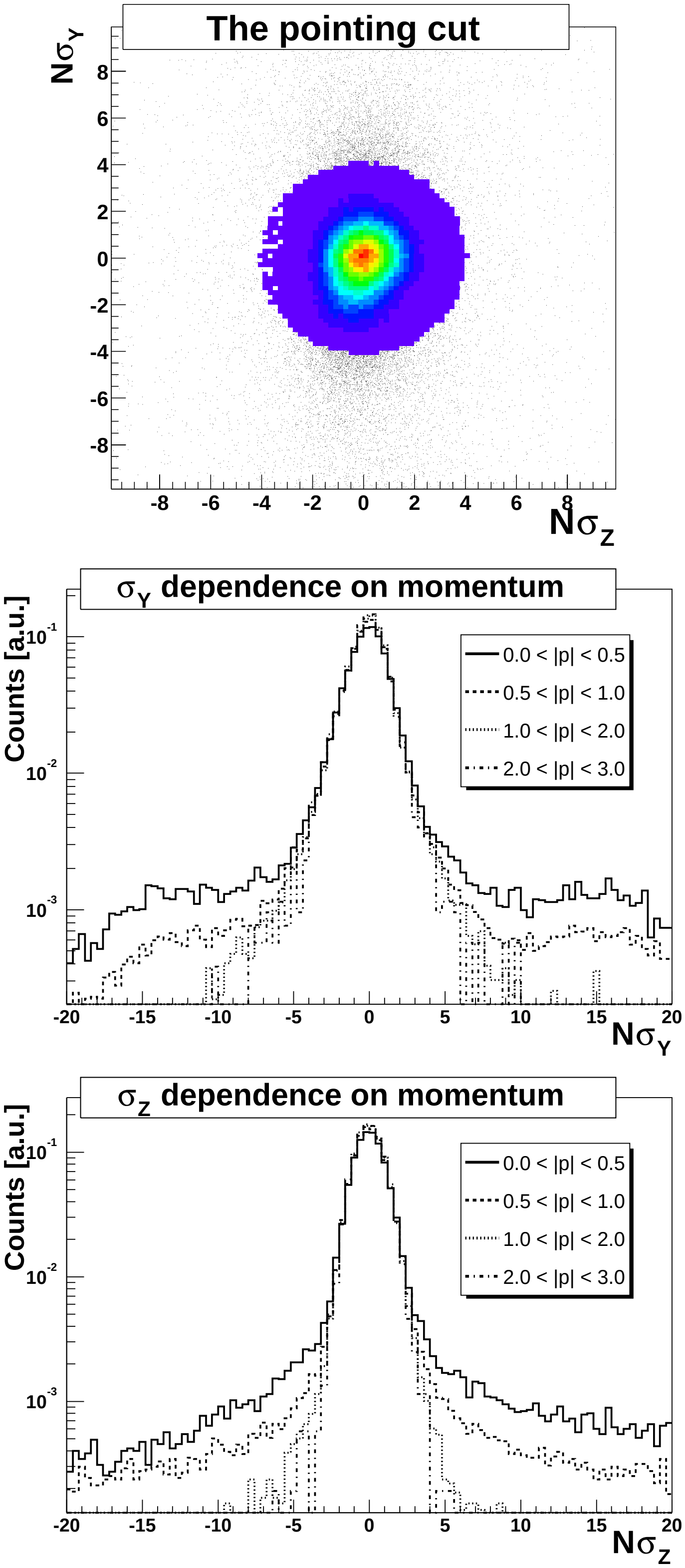

Figure 4.1: Top: The scatter plot is the distribution of pointed tracks measured in standard deviations. The colored circle is selected by the cut. Lower: The plots show the momentum dependence of the standard deviation distributions. The background depends on the momentum and is almost negligible at momentum above 1.0 GeV.

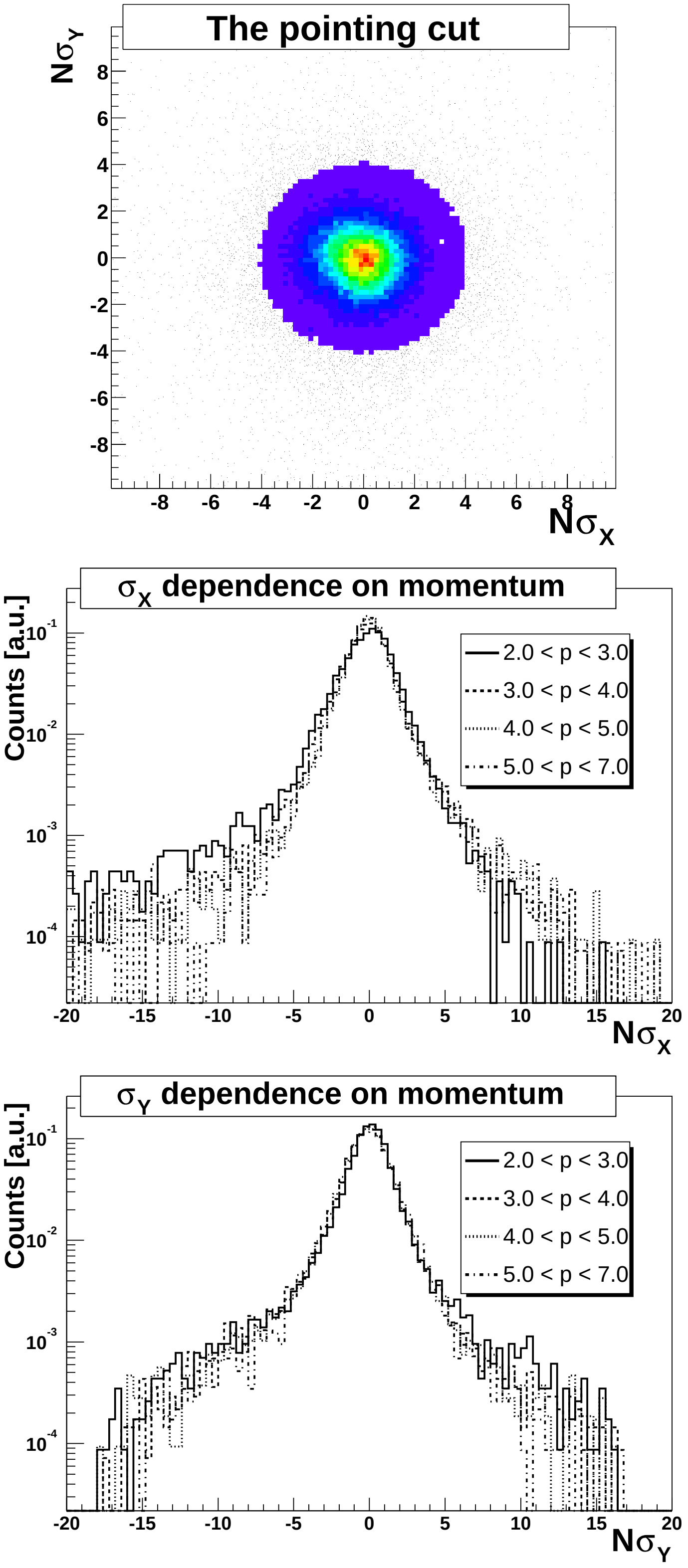

Figure 4.2: Identical to Figure 4.1 except it is for the FFS. The background is almost independent of the momentum.

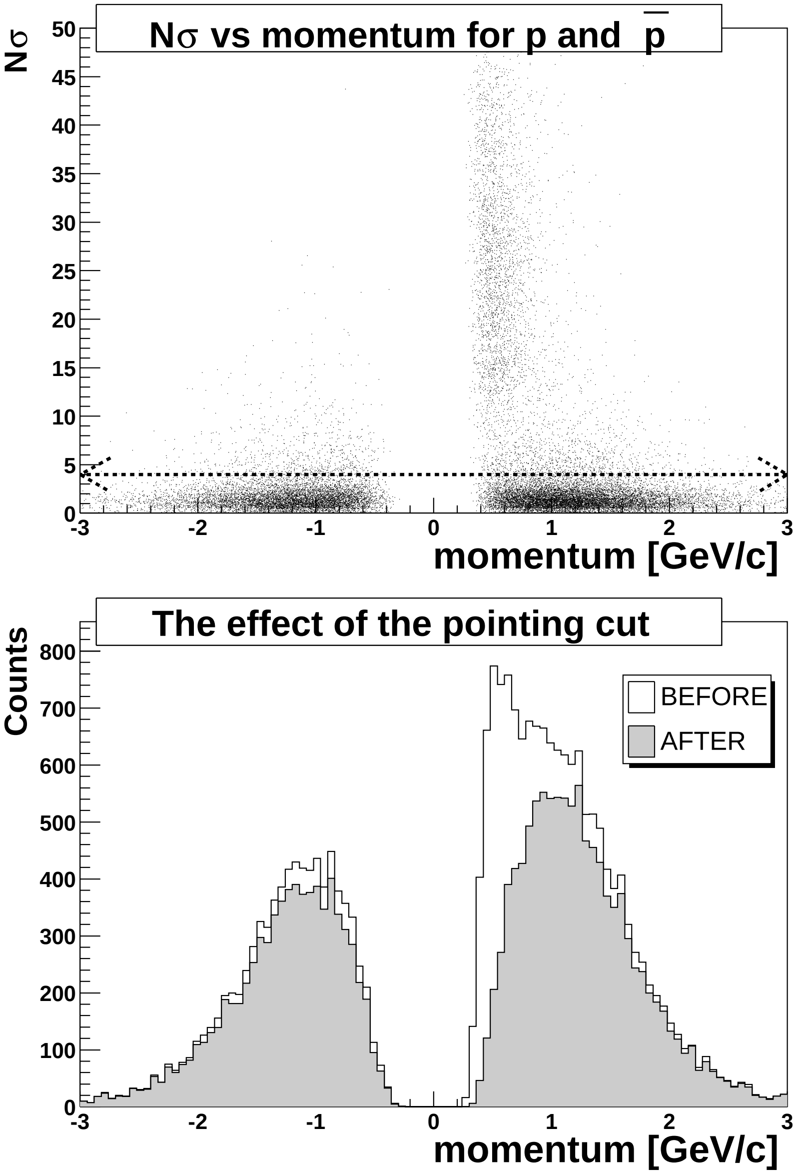

Figure 4.3: Top: The deviation of proton ($p > 0$) and anti–proton ($p < 0$) tracks when pointed back to the IP, measured in units of the standard deviation σ as a function of momentum. Note that the background is much larger for the protons than for the anti–protons. The cut applied to the data is illustrated with a double–arrow. Bottom: The effect of the pointing cut on protons and anti–protons. The shaded distribution is after the cut.

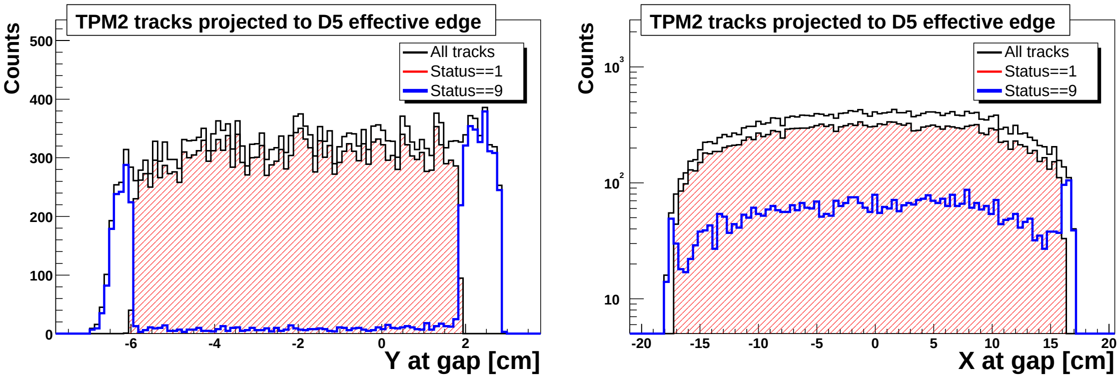

Figure 4.4: The effect of the magnet fiducial cut. For an identified MRS track the TPM2 track has been projected to the back of the D5 magnet. The plot shows the vertical (left) and the transverse (right) position calculated in the reference frame of TPM2 where the magnet center is at $y \sim -2.05$ cm. Tracks with status 1 (hatched) are accepted and status 9 tracks (blue) are rejected by the magnet fiducial cut. The left figure also shows that there is an efficiency loss at large drift distances since the distribution should be symmetric.

Since the height of the D5 magnet aperture is $\sim$ 10 cm the effect of cutting out 2 cm is a reduction of the data by $\sim$ 20 %. It would be good if a smaller fiducial cut could be applied, but the current quality of the match–up in the vertical (y) direction currently does not allow this. This can be seen in the vertical cut plot, Figure 4.4, where the lower cut (affecting tracks with the longest drift time) cannot be reduced. This is associated with the inhomogeneities in the drift velocity discussed in section 3.7.3.

In the FS the situation is similar to the MRS except for some minor details. Once the momentum of the track is known it can be projected back through the D1 magnet to point to the IP and ensure that it does not intersect the edges of the magnet gap. Since the vertical acceptance is determined by the D1 aperture, few tracks are removed by vertical fiducial cuts in the rest of the FS.

4.1.3 MRS PID Selection

In the MRS, particles are identified based on cuts in m^2, as calculated from the TOF measured by the TOFW and the D5 momentum p (section 3.5). The momentum dependence of the m^2 resolution was parameterized for pions, kaons, and protons (see Appendix D) and used to make 2σ cuts to identify protons. The data selection is illustrated in Figure 4.5. There is a slight asymmetry in the masses between particles and anti–particles in the MRS settings, and for each particle species the mass squared distribution was fit with a Gaussian and the mean used to fix the mass

The proton and kaon 2σ curves are typically separated up to $p = 3$ GeV/c. Since most of the proton yield is in the p_T range $0.5 < p_T < 1.5$ GeV/c the MRS ($35° < \theta < 90°$) has good

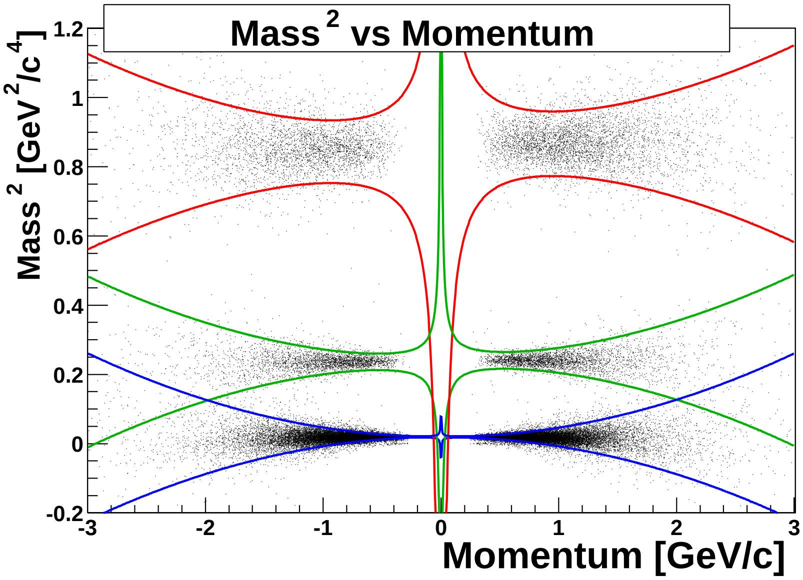

Figure 4.5: The m^2 measured by TOFW vs. momentum p at 90 degrees. The width of the m^2 distribution increases with p. The red curves display the cuts used to identify protons.

coverage.

Type	Cut	Explanation
GLOBAL	$\Delta_{IP} < 15$ cm	Trigger efficiency
GLOBAL	BB Method = 1 or 2	BB Method 3 has bad resolution
GLOBAL	$\lvert \mathrm{BB}_{IP} - \mathrm{ZDC}_{IP} \rvert < 3\sigma$	Reject background events
TRACK	D5 Status = 1	Magnet fiducial and ghost cuts
TRACK	slat > 25 and slat < 103	Poor TOFW calibrations
TRACK	slat $\neq$ 31, 76, 92	Bad TOFW slats
TRACK	Δslat ≤ 1	Point to TOFW slat
TRACK	Δy slat $< 3\sigma$	Point to TOFW hit
TRACK	$\sigma < 4.0$	Point to IP
PID	$p < 3.0$ GeV	PID momentum cut
PID	$\Delta m^2 < 2\sigma$	Proton cut

Table 4.1: Summary of cuts used in the MRS to select protons and anti–protons. In addition to this a global centrality selection was done.

The cuts used in the MRS analysis are summarized in Table 4.1. Only the TOFW cuts remains to be discussed. As, it turned out, some of the slats in the TOFW fell outside the acceptance and others had very few hits which decreased the quality of the calibrations. Tracks with a hit in one of these slats are ignored. This, in effect, cuts off the acceptance at low momentum. There are also slats where the signals are missing or bad and these have been similarly ignored. The missing panels and slats are corrected for in the acceptance maps, see section 4.3. The pointing of tracks to the slats has finite resolution and it is accepted that a track may be correlated with a hit in a neighboring slat. The final check is of the agreement between the vertical position of the projection and the horizontal slat position calculated from the time–difference of the top and bottom PMT. The distribution is Gaussian and a 3σ cut is applied. A typical value of the width is ≈ 0.9 cm for the TOFW (and ≈ 0.6 cm for H1 and ≈ 0.8 cm for H2).

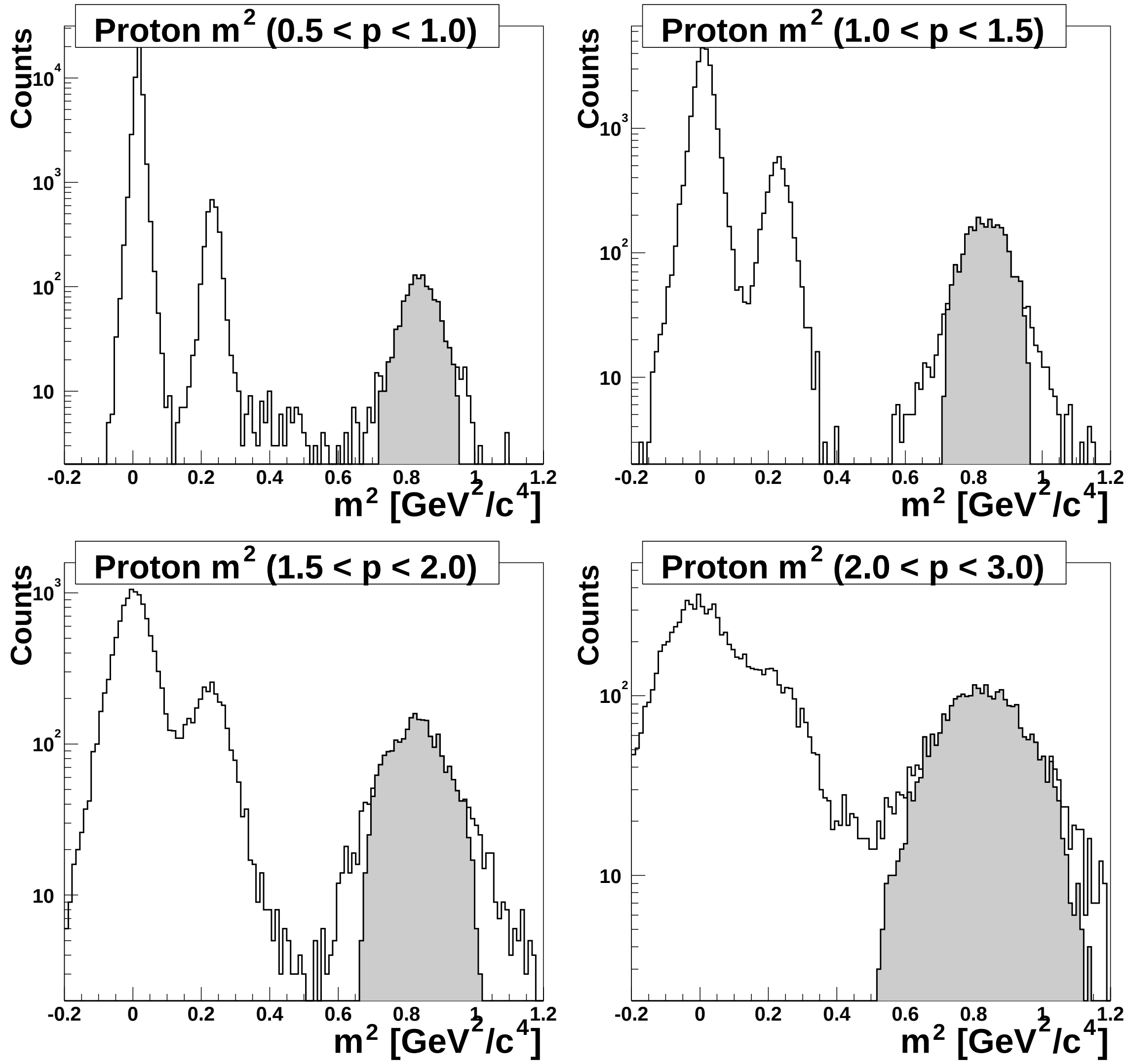

Figure 4.6: TOFW PID at 35 degrees. The open histograms are the m^2–distribution after all track cuts have been performed, while the filled histograms show the protons selected by 2σ m^2 cuts.

The protons selected in a 35 degree setting are shown in Figure 4.6. The m^2–resolution is worse at low polar angles, but in all MRS settings the background is negligible.

4.1.4 FFS PID Selection

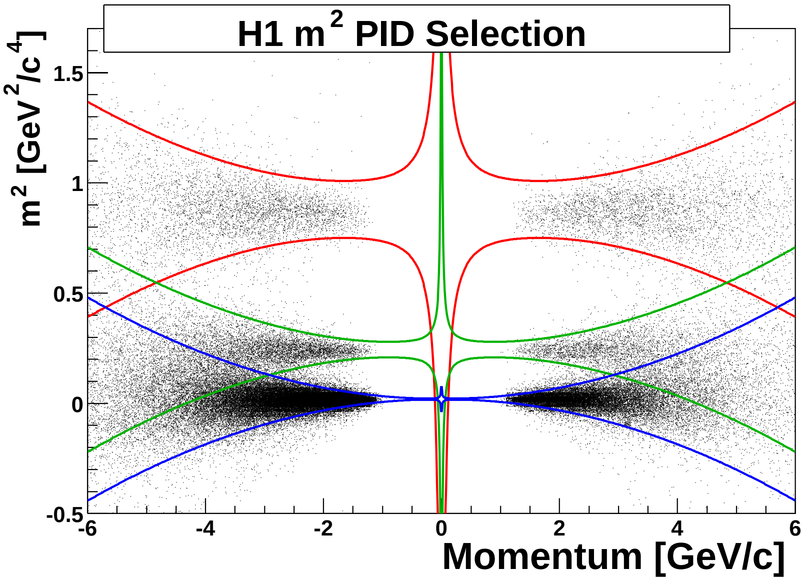

Figure 4.7: The m^2 measured by H1 vs. momentum p. The blue, green, and red curves are the 2σ curves used to select pion, kaons, and protons, respectively.

In the FFS the PID of protons and anti-protons is done with TOF using H1. In the FFS where the polar angles are smaller it is important to press the PID to as high momentum as possible to obtain good p_T coverage. The momentum dependence of the m^2 resolution was parameterized for pions and protons similarly to what was done in the MRS, see Figure 4.7. The kaons were not used to fit the parametrization because of the low range where there is $\pi - K$ separation, but the parametrization still appears to describe the kaons well, as it should.

For most settings the kaon and proton 2σ bands are separated up to 5 GeV/c, but in the 4-degree setting the separation only reaches to 4 GeV/c. This is discussed in section 4.2.3.

By comparing the 2σ selection with a 4σ selection it was found that the ratio showed no momentum dependence (before kaons and pions starts to contaminate) and that the ratio was within 2–3% of the 95.5% expected from a Gaussian distribution.

All the cuts applied to the data are shown in Table 4.2.

The protons selected in a 12 degree setting are shown in Figure 4.8.

4.1.5 FS PID Selection

In the FS two different PID methods have been used. For low magnetic field settings, H2 can be used to identify protons up to $p \sim 7$ GeV/c. For high field settings, the RICH can be used to identify protons above $p = 10$ GeV/c.

Type	Cut	Explanation
GLOBAL	$\Delta_{IP} < 20$ cm	Trigger efficiency
GLOBAL	BB Method = 1 or 2	BB Method 3 has bad resolution
GLOBAL	$\lvert \mathrm{BB}_{IP} - \mathrm{ZDC}_{IP} \rvert < 3\sigma$	Reject background events
TRACK	D1 and D2 Status = 1	Magnet fiducial and ghost cuts
TRACK	Δy slat $< 3\sigma$	Point to H1 hit
TRACK	$\sigma < 4.0$	Point to IP
PID	p < 4.0–5.0 GeV	PID momentum cut
PID	$\Delta m^2 < 2\sigma$	Proton cut

Table 4.2: Summary of cuts used in the FFS to select protons and anti–protons.

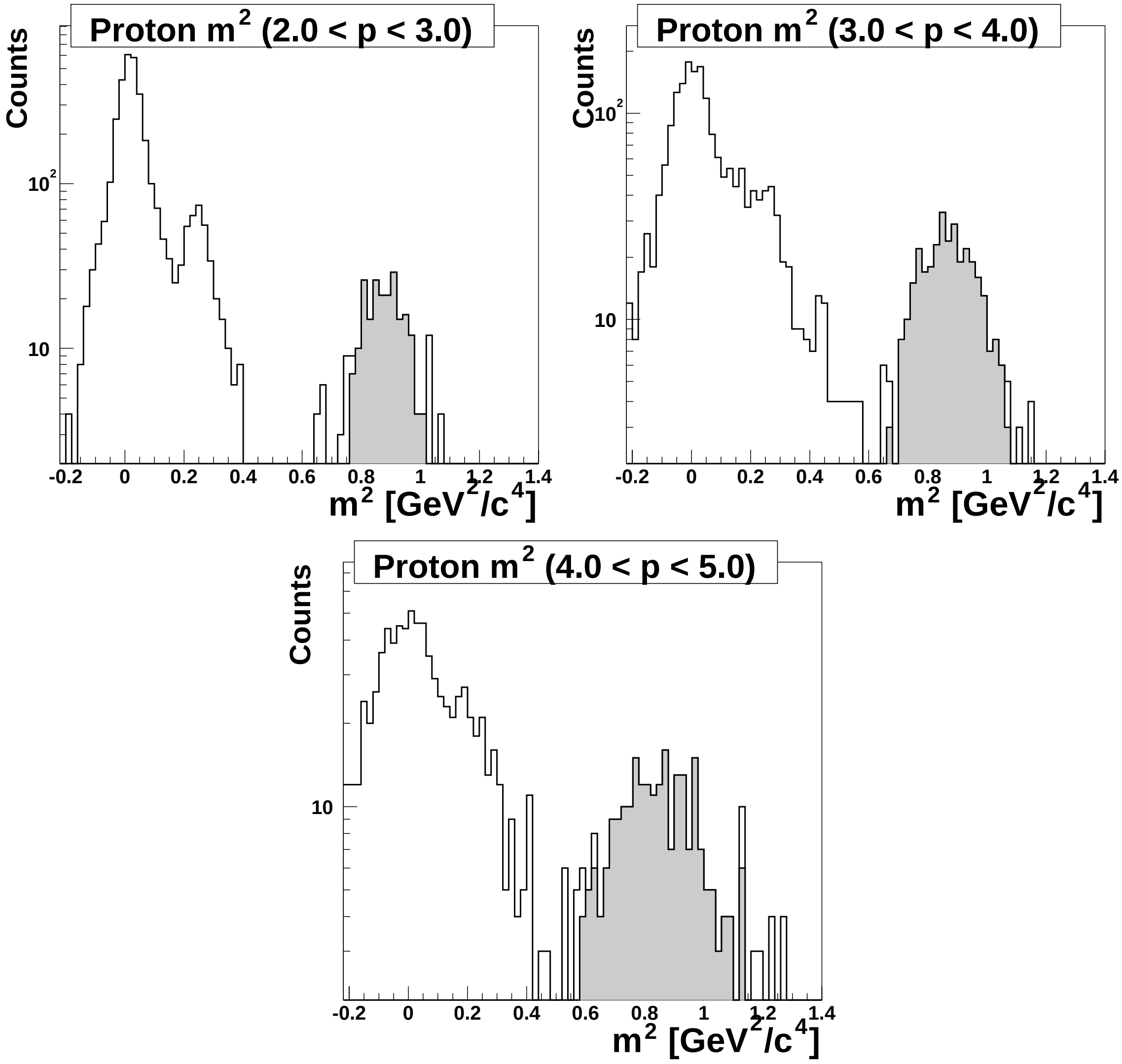

Figure 4.8: H1 PID at 12 degrees. The open histograms are the m^2–distribution after all track cuts have been performed, while the filled histograms show the protons selected by 2σ m^2 cuts.

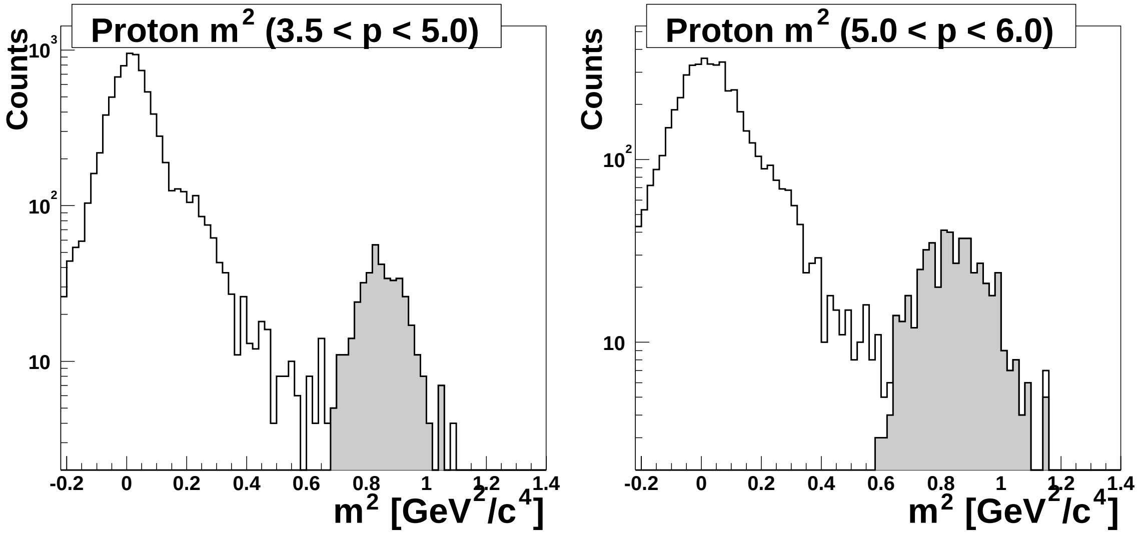

Figure 4.9: H2 PID at 4 degrees. The open histograms are the m^2–distribution after all track cuts have been performed, while the filled histograms show the protons selected by 2σ m^2 cuts.

The H2 identification is performed similarly to the H1 identification described in the last section, and the cuts are identical to those in Table 4.2, with the exception of the magnet status, which is also checked for D3 and D4, and for the momentum cuts which are $p < 6.0$ GeV/c (4 degrees) to $p < 7.0$ GeV/c (8 and 12 degrees). The protons selected in a 4 degree setting are shown in Figure 4.9.

In the following the PID with the RICH will be described. The Cherenkov threshold for protons in the RICH is $p \sim 15$ GeV/c, see Figure 4.10. This corresponds to a transverse momentum $p_T \sim 1.1$ in a 3 degree setting (where the average polar angle is $\theta \sim 4.35^\circ$). Figure 3.11 shows that H2 can not be used to extend coverage to low momentum in the very forward rapidity region ($y \sim 3$) where the RICH has good coverage. However, the RICH can be used to veto electrons, muon's, pions, and kaons for tracks with momentum above the kaon threshold ($p > 10$ GeV/c). Except for protons and very few light clusters and anti–clusters (deuteron's, triton's) this is all the particles observed, so protons can be identified as particles with momentum above kaon threshold that do not produce a signal in the RICH (the RICH is used to *veto* lighter particles).

Protons are identified in two ways with the RICH. The first way is the direct way also used to identify pions and kaons. Figure 4.10 shows the phenomenological curves used to identify pions, kaons and protons. The curves have the shape :

$$r = L\tan\left(\cos^{-1}\left(\frac{1}{n}\left[1+\frac{m^2}{(p\pm\delta p)^2}\right]\right)\right) \pm \delta r \tag{4.1}$$

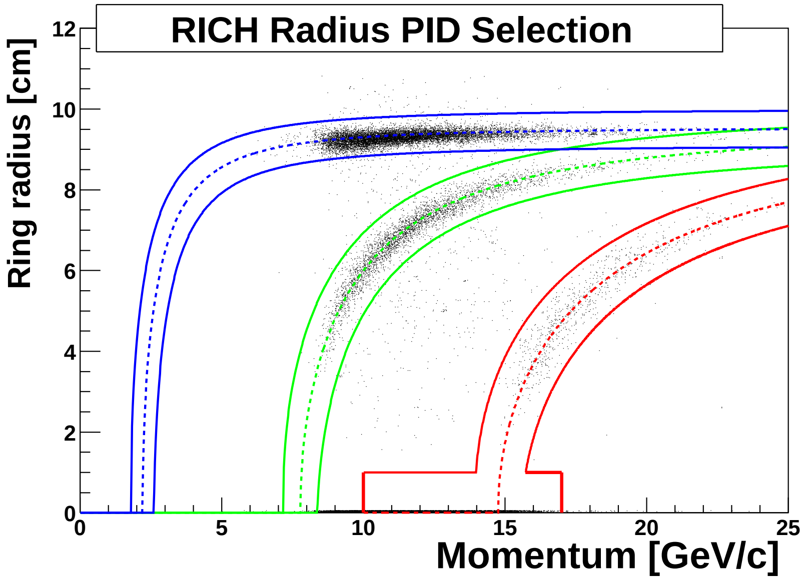

Figure 4.10: The ring radius measured by the RICH vs. momentum p.

where $L = 150$ cm is the focal length of the spherical mirror and $n \approx 1.00202$ is the refractive index. For $\delta p = 0$ and $\delta r = 0$ equation 4.1 expresses the theoretical relation between r, p, and m. The two extra parameters δp and δr are used to mimic the momentum and ring radius resolution. In Figure 4.10 the values used are $\delta r = 0.45$ cm and $\delta p = 0.4, 0.6, 0.8$ for pions, kaons, and protons, respectively. The $(+)$ in equation 4.1 corresponds to the top curve and the $(-)$ corresponds to the lower curve for each particle species. The δp value is most important near the threshold of each particle, where the ring radius is increasing rapidly, so that the δp used for pions reflect the momentum resolution around $p \sim 2 - 3$GeV/c, $p \sim 8 - 9$GeV/c for kaons, and $p \sim 15 - 16$GeV/c for protons. Since the momentum resolution depends on momentum $\delta p/p \propto p$, a bigger δp is needed for protons than for kaons and pions.

The second way of identifying protons is the indirect way. When the ring radius is zero and the momentum is in the interval beginning above the kaon threshold to the proton threshold, the particle is identified as a proton. The lower momentum cut of $p > 10$ GeV/c was chosen to be far from the kaon threshold, and the high momentum cut $p < 17$ GeV/c was chosen to have a continuous momentum spectrum in the region where the two methods overlap. The ring finding algorithm was found to be ineffective close to the threshold, so the indirect method had to be extended into the region where the protons could have been identified directly.

This indirect method could introduce contamination in the data from the following sources

- Inefficiency. A ring from e.g. a pion that is not found would cause the pion to be identified as a proton.

- Absorption and decays. A particle that has a track all the way through the FS but is

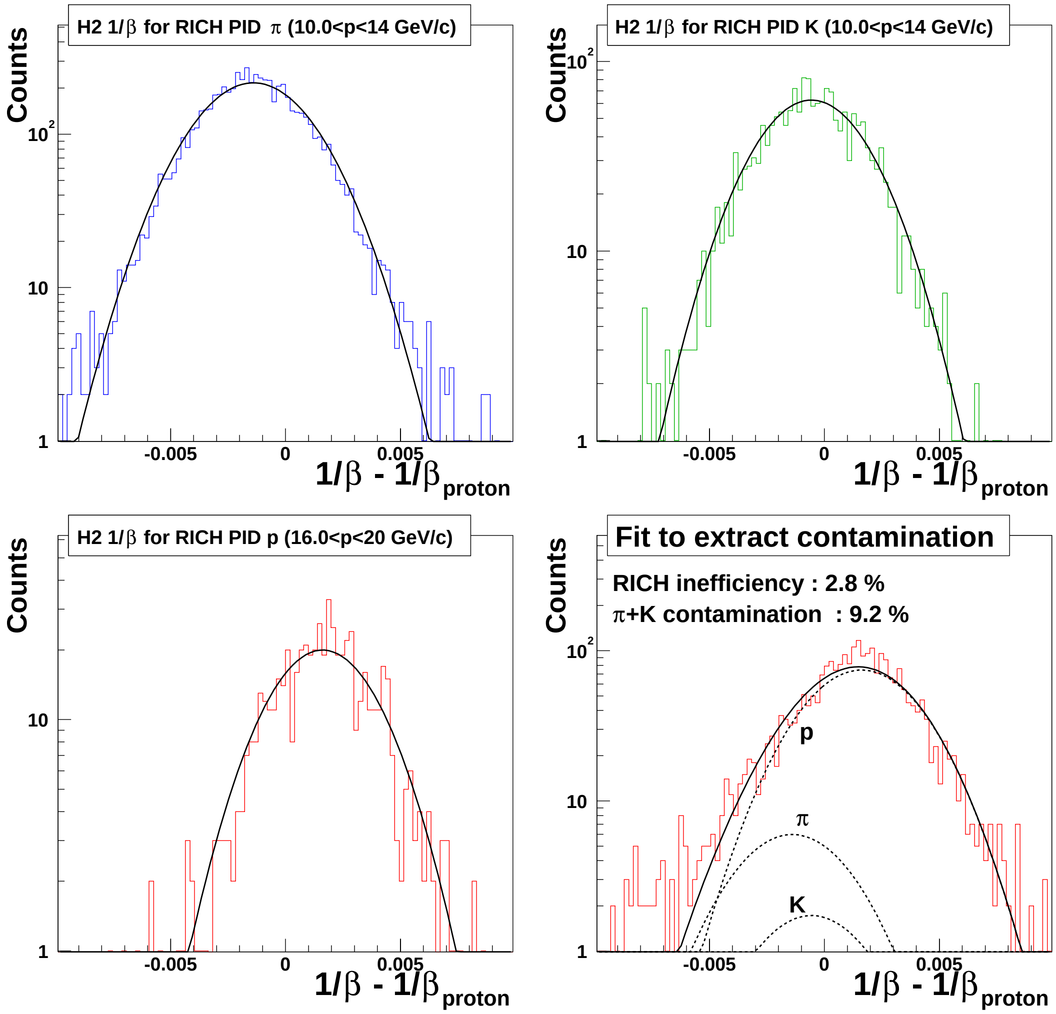

Figure 4.11: On all plots the abscissa is $1/\beta$ measured by H2, subtracted the expected $1/\beta$ for a proton with the same momentum. Top Left: Pions identified by the RICH in the momentum interval, $10 < p < 14$ GeV/c, where proton identification is done by the veto method only. The distribution has been fitted by a Gaussian. Top Right: The same distribution for kaons. Bottom Left: The same distribution for protons, however the momentum interval is, $16 < p < 20$ GeV/c, and protons are identified by rings in the RICH. (The offset in the distribution from 0 is independent of momentum and due to a poor time–offset calibration). Bottom Right: The distribution of protons identified in the RICH by the veto method ($10 < p < 14$ GeV/c) fitted with the sum of the three Gaussians from the first plots, see text.

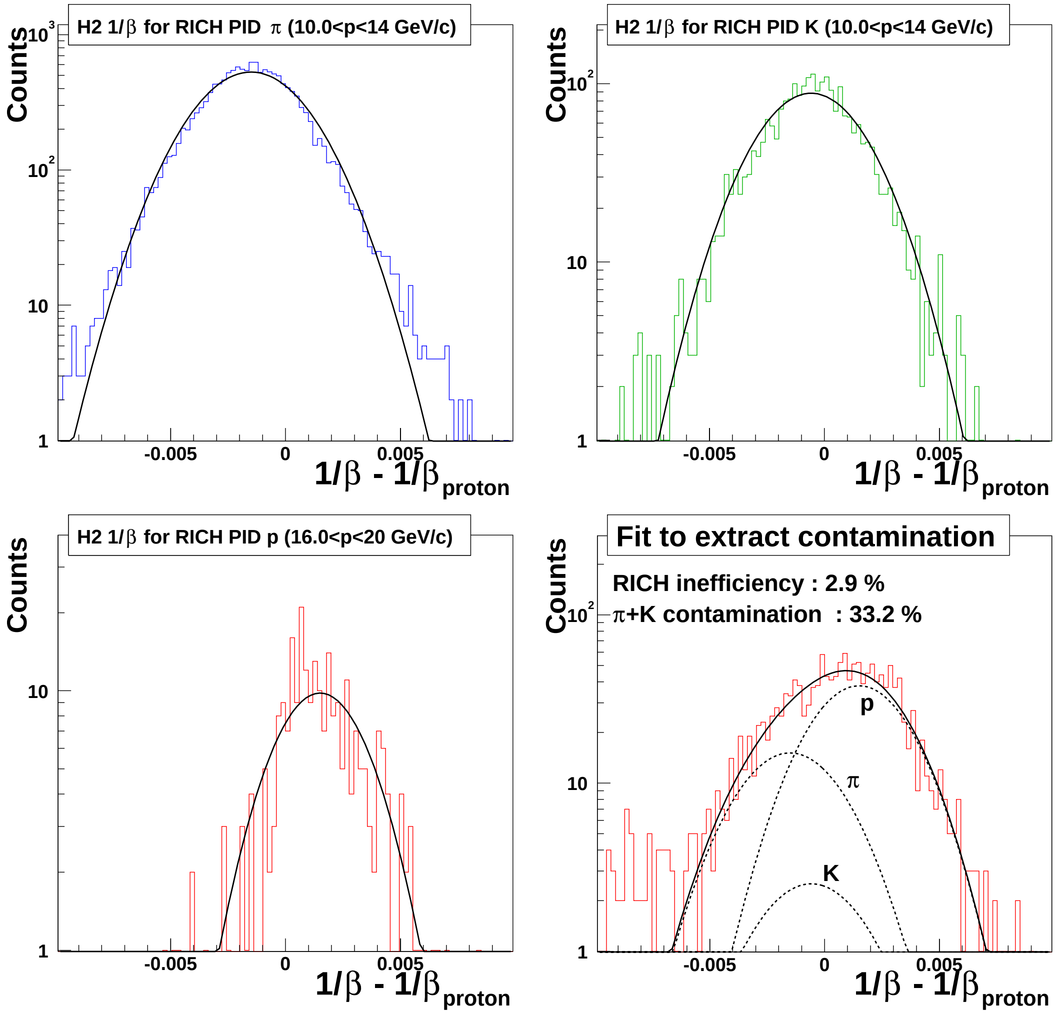

Figure 4.12: The plots are equivalent to Figure 4.11, but the study is done for anti–protons.

absorbed or decays between T5 and the RICH will be identified as a proton unless the decay products are identified in the RICH.

The contamination in the proton sample identified by the indirect method has been studied using H2. The time-of-flight resolution is not good enough to separate protons from kaons and pions, track by track, at this high momentum ($10 < p < 16$ GeV/c), but even though the m^2 distributions are wide, they are centered at the correct masses for pions, kaons, and protons.

To estimate the contamination in the proton and anti–proton data an approach similar to that done in [51] was taken. The velocity difference, $1/\beta - 1/\beta_{proton}$, where $1/\beta$ is measured by H2 is studied. The width of this distribution is almost constant as a function of momentum and it is described well by a Gaussian for pions and kaons in the region where the protons are only identified by the veto method, $10 < p < 14$ GeV/c, and for protons identified by rings in the RICH, $16 < p < 20$ GeV/c (and ring radius greater than zero). The contamination is assumed to be the same fraction of kaons and pions.

The proton sample identified by the veto method, $10 < p < 14$ GeV/c, can then be described by a signal component (proportional to the proton distribution observed at higher momentum) and a contamination component, which is proportional to the sum of the pion and kaon distributions in the same momentum range, where the proportionality constant is the RICH inefficiency. In Figure 4.11 and Figure 4.12 the results of the contamination analysis for two settings are shown. The same RICH inefficiency of $\sim 3\%$ is found in all settings used in this analysis. The effect of this inefficiency is very significant and clearly largest in the anti–proton case where 30% of the "protons" are misidentified pions and kaons. This difference is caused by the low anti–proton multiplicity compared to the proton multiplicity (while the pion multiplicity is the same in both settings), see Chapter 5. The description of the vetoed proton sample as a superposition of fits to the other data samples works well. There is a tail in the vetoed proton distribution that is not observed in the other distributions. This suggests that there is yet another, much smaller contamination from tracks that also lacks a "good" H2 signal. This is presumably some kind of background and has been ignored in the analysis.

The correction of the spectrum is done by assuming that all pions and kaons are protons, and then subtracting the spectrum obtained from this analysis multiplied by the RICH inefficiency from the spectrum obtained using the RICH PID described above. This is shown in Figure 4.13. The directly measured protons are corrected for the efficiency.

4.1.6 The Output of the Data Selection

The data is divided according to the BB IP position, since the geometrical acceptance depends on the IP (section 4.3). In the MRS as well as the FS, 5 cm wide bins have been used. For each IP bin the data is stored in 2–dimensional $y - p_T$ histograms. The segmentation of

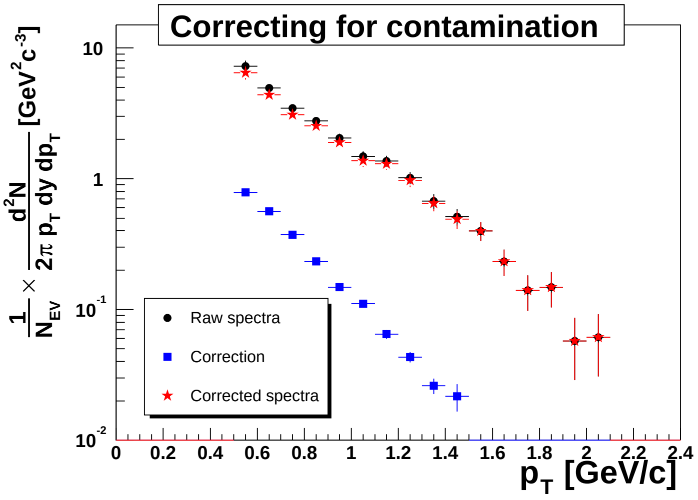

Figure 4.13: The correction for pion and kaon contamination in the spectrum obtained from protons identified by the RICH. The raw spectrum is subtracted a correction spectrum to obtain the final spectrum. The correction spectrum is built from pions and kaons identified by rings, but treated in exactly the same way as the proton spectrum i.e., the mass used for calculating the rapidity is the proton mass and the acceptance and correction for protons are used. The normalized correction spectrum is finally multiplied with the RICH inefficiency. The correction spectrum is limited to the momentum range where the indirect method is used for PID ($10.0 < p < 17.0$ GeV/c).

Type	Cut	Explanation
GLOBAL	$\Delta_{IP} < 20$ cm	Trigger efficiency
GLOBAL	BB Method = 1 or 2	BB Method 3 has bad resolution
GLOBAL	$\lvert \mathrm{BB}_{IP} - \mathrm{ZDC}_{IP} \rvert < 3\sigma$	Reject background events
TRACK	D1, D2 D3, and D4 Status = 1	Magnet fiducial and ghost cuts
TRACK	$\sigma < 4.0$	Point to IP
PID	p > 10.0 GeV	PID momentum cut
PID	RICH radius > -1.0	Track projects to RICH readout plane
PID	RICH radius cut	Proton cut see Figure

Table 4.3: Summary of cuts used in the FS to select protons and anti–protons.

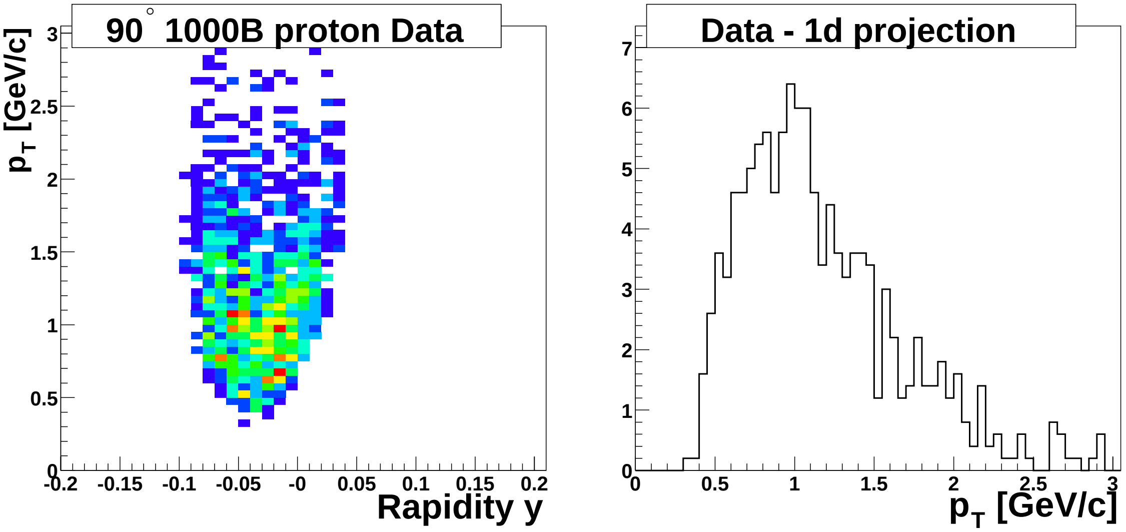

Figure 4.14: Protons selected in one setting in one IP bin (left). The right plot shows the projection for three of the central rapidity bins.

these histograms has been chosen to reflect the resolution of the detector and statistics. For transverse momentum, 50 MeV bins have been used for both spectrometers. Rapidity bins of width 0.01 unit of rapidity were used in the MRS, while bins of 0.02 units have been used in the FS. Figure 4.14 shows the proton distribution for one of the IP bins and a projection onto the p_T-axis of a few rapidity bins. The next sections will focus on how to correct the spectra for acceptance and efficiency, and how to combine different vertex bins and multiple settings to obtain spectra with good statistics.

4.2 Efficiency

The reconstruction efficiency has two components, the efficiency of the track reconstruction and the efficiency of the PID selection.

The tracking efficiency has been studied by using track embedding of simulated tracks (MRS and FFS) [54] (see details later) and by comparing the number of identified track segments in the tracking chamber under consideration to the number of reference tracks determined by other detectors disregarding the chamber [53]. The latter method is only applicable in the forward spectrometer where there are several tracking detectors (at least three are needed to have redundant information about the momentum).

The average efficiency as a function of spectrometer angle is shown in Figure 4.15.

In the MRS the track embedding efficiencies were used, while for both FFS and FS data the reference track method was used. In the FFS data the efficiency is $\approx 10\%$ lower for the reference track method than for the embedding method. This discrepancy is not understood,

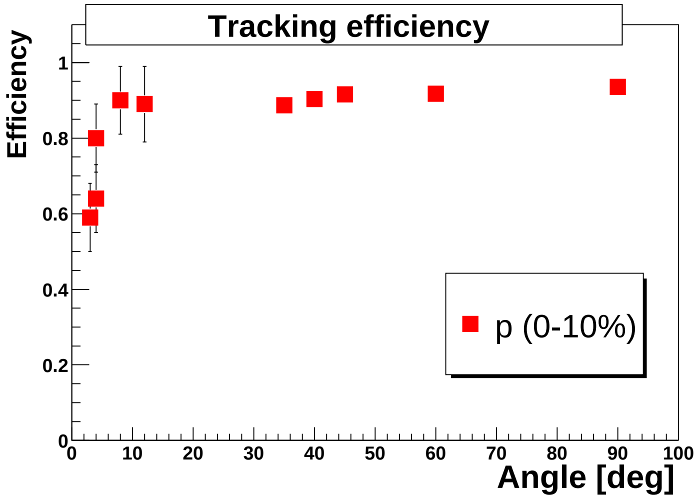

Figure 4.15: The average tracking efficiency in several different angular settings. The points at 35 degrees and above are MRS efficiencies and the points below are FS efficiencies. The two lowest points are for the full FS and the three other points are for the FFS. The reconstruction efficiency in each spectrometer increases with the spectrometer angle because the occupancy in the tracking detectors decreases. The efficiency is the same for protons and anti–protons. The error bar shows the variance of the efficiency distribution in a setting.

but it is clear that the embedding method is limited by the description of the TPC performance and if that is overestimated, the efficiency calculated with this method will be higher. In the MRS the efficiency has also been studied using zero magnetic field runs with a simple method analogous to the track reference method and here, agreement with the embedding method was found [52].

For the track embedding method the results are consistent with one universal curve in the MRS, whereas this is not the case in the FFS.

4.2.1 Track Embedding Method

The track embedding method has solely been used for the TPCs. Inserting a simulated track with a well defined momentum and PID into a real event at the raw data level (TPC segments, see section 3.7), one can study the efficiency with which it is reconstructed by the software as a function of the number of hits in the TPCs for the event. Using real events ensures realistic occupation and noise. The modified event is then reconstructed and the reconstructed tracks are compared to the known track originally inserted in the event. Each track is treated as a cylinder centered on the track with a radius of 0.4 cm. Each track is then compared to the simulated track by calculating the overlap of the two cylinder volumes (between 0 and 100%). The track is said to be reconstructed if the overlap is greater than 60%.

The results of the efficiency calculation is the efficiency in the MRS (FFS) as a (linear)

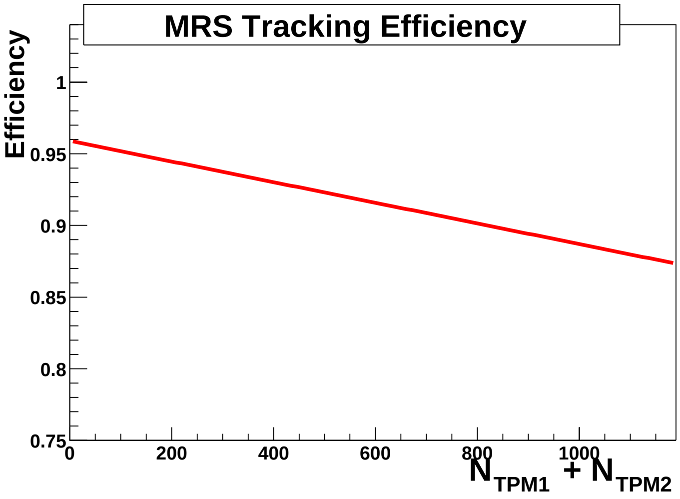

Figure 4.16: The tracking efficiency used to correct the MRS data. Average occupancy for 0–20% central events is 300 hits at 90° increasing to 800 hits at 35°, hence the tracking efficiency decreases with spectrometer angle.

function of the total number of reconstructed hits in TPM1 and TPM2 (T1 and T2) for pions, kaons, and protons in various spectrometer angle settings. The function used for the efficiency correction is shown in Figure 4.16. When the corrections are applied in this manner there is no momentum dependence. The momentum dependence was studied in [54] and the dependence observed was related to multiple scattering which is separately corrected for in this work, section 4.4. For each centrality setting the same average efficiency is applied to all the data.

The momentum resolution was studied in the same analysis by comparing the momentum of the simulated track to the momentum of the reconstructed track, see section 3.4.

4.2.2 Reference Track Method

In the reference track approach to the tracking efficiency, the aim is to construct a reference track in $N-1$ tracking detectors and then determine if it was identified in tracking detector N. The efficiency for a single detector is then given as :

$$E_{rec} = \frac{N_{local}}{N_{ref}} \tag{4.2}$$

where, N_{ref} is the total number of reference tracks and N_{local} is the number of reference tracks that were identified, in the considered detector.

In the FS there are 5 tracking detectors. The detector studied is never used to construct the reference track, instead three or four local track segments of the remaining detectors are

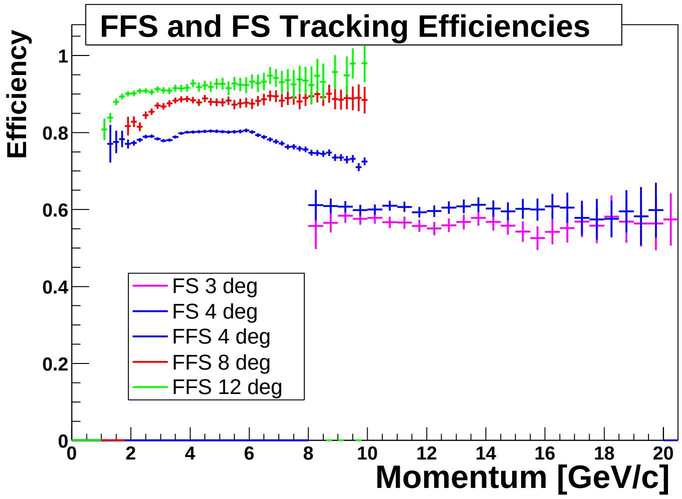

Figure 4.17: Example of tracking efficiencies used to correct the FFS and FS data. The FFS tracking efficiency is the combined efficiency of T1 and T2. The FS efficiency is the combined efficiency of the FFS and T4 and T5. The curves shown in the figure are used for correction. The efficiencies showed are for 0-10% central data.

matched and the track build from these segments are projected to the detector studied. For T5, H2 is used to confirm that the track made it through T5, while for the front detectors, T1 and T2, it is assumed that when there is a track in the BFS, there is always a corresponding FFS track. For the track to be identified, it is required that a local track is found where the deviation in positions at the center of the tracking detector as well as the slope of the two tracks are consistent by applying 4σ matching cuts in all four track variables $(x, y, \alpha_x, \alpha_y)$. On one hand the cut should reject background tracks, but on the other hand it should not reject "good" reconstructed tracks. The 4σ cut is so broad that it accepts all "good" reconstructed tracks and it was found by applying only three of the matching cuts that the background in the distribution of the final variable is negligible.

The efficiency calculation is done setting by setting. It is calculated as a function of centrality (occupancy) and horizontal position and slope in the tracking detector (three parameters). The centrality class 10-20% is typically 5% more efficient than 0-5%. More details of the calculation can be found in [53].

In Figure 4.17 the average tracking efficiencies as a function of momentum are shown. The tracking efficiency is applied to the protons in this form, rather than track by track because of the way the spectra analysis is done, see section 4.5.

4.2.3 PID Efficiency

The RICH efficiency has already been discussed in section 4.1.5, so here only the TOF efficiency is discussed.

The TOF efficiency is separated into two independent components.

Bad slats and the two outer panels in the TOFW have been ignored in the data. The correction for those missing slats was done by ignoring them in the geometrical acceptance maps, see section 4.3. The correction is hereby applied at exactly the phase space region $y - p_T$ that the slat would cover.

The second component is the efficiency of working slats. The TOF detectors have slightly different design in the MRS and in the FS. In the TOFW the slats are stacked together in a single row, so there will be some efficiency loss since the tracks can pass through the wrapping of the slats or the path length in the detector is so short and the energy deposited therefore so low, that no hit is reconstructed. For H1 and H2 the slats have been stacked in two rows where every second slat is placed in the same row to reduce this effect. The distance between the two rows is of the order of a slat width. This however results in the possibility to completely miss a slat for angled tracks.

The slat efficiency has been estimated similarly to equation 4.2 by projecting tracks from the TPCs to the slat and comparing this to how often a hit is registered. In the FS the tracking detectors after H1 can be used to ensure that the particle did not decay between T2 and H1, but this is not possible in the MRS. Instead the high momentum data ($p \geq 2$ GeV/c) is used to determine the slat efficiency. No slat dependence is observed in the MRS and the efficiency is found to be $\sim 93 \pm 2\%$ for TOFW. The error on the efficiency was estimated from the variation between settings. In H1 the efficiency depends on the slat and ranges from 0.93 to 1.0. This is related to the angle of incidence on the detector. In H2 the efficiency is $\sim 98 \pm 1\%$.

In addition to the slat efficiency there is also a correction for hits that are ignored because multiple tracks are pointing to the slat. This effect depends on the track density and is negligible for the TOFW and H2, but for H1 in the 4 degree setting it is a 5 % correction. Because of the low tracking efficiency there are many unidentified tracks that have hits in the TOF detectors, rendering the effect of multiple hits underestimated. There are preliminary studies of this for H1, using tracks in T2 that were not matched with T1 tracks and they indicate that the correction for multiple hits might be twice as large in the four degree setting [56]. This could also explain why the resolution is worse in these settings, since the large background results in a lower quality of the calibrations.

4.3 Acceptance

Figure 4.18 illustrates that the measurement has to be corrected for the finite solid angle coverage and that this correction depends on the IP. The acceptance maps used in the following are 2–dimensional histograms, where the axes are rapidity and transverse momentum. The value in each histogram cell gives the probability of a particle with that rapidity and

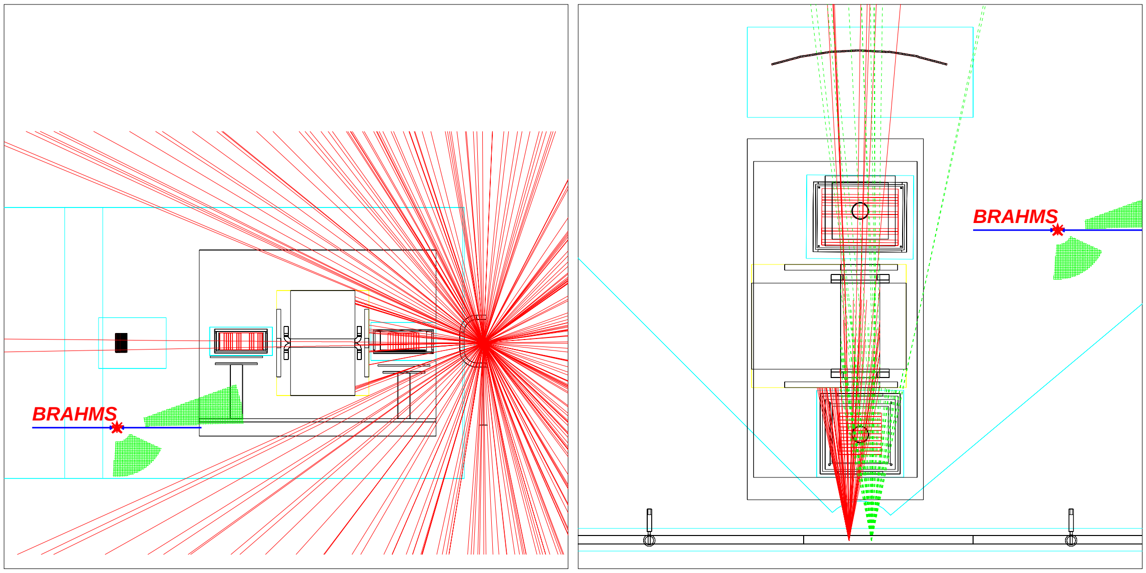

Figure 4.18: The plots illustrate some features that the geometrical acceptance correction has to correct for.

transverse momentum ending in a geometrical region of the detectors where it could be reconstructed and identified as a good (anti–)proton track. The correction applied to the data is then the inverse of this probability.

The acceptance is purely geometrical and is calculated using BRAG, see Appendix F for details. A flat distribution in momentum p, θ, and ϕ, of single particles is generated in a solid angle subtended by the magnet gap ($\mathrm{THROWN}(y, p_T)$). In the simulation, these particles are propagated through the detector and it is later determined which are detected ($\mathrm{ACCEPTED}(y, p_T)$). The acceptance map for a single vertex interval can then be calculated as :

$$\mathrm{ACC}(y, p_T) = \frac{\mathrm{ACCEPTED}(y, p_T)}{\mathrm{THROWN}(y, p_T)} \times \frac{\Delta\phi}{2\pi} \tag{4.3}$$

The last factor ($\Delta\phi/2\pi$) reflects that particles are not generated in the full ϕ range (2π), but only in a large enough angle interval $\Delta\phi$ to completely cover the vertical aperture of the first magnet in the spectrometer. Figure 4.19 shows the histograms used to build an acceptance map.

In the simulation, energy loss is the only physical process included (see Appendix F), so the simulation will be similar for pions, kaons, and protons i.e., a (p, θ) description of the geometrical acceptance will be identical. However, when rapidity y is used to characterize the phase space, a map is needed for each particle species since the rapidity depends on the particle mass. The acceptance maps for different particle species are built from the pion simulation by applying the appropriate rapidity transformation (the transverse momentum is

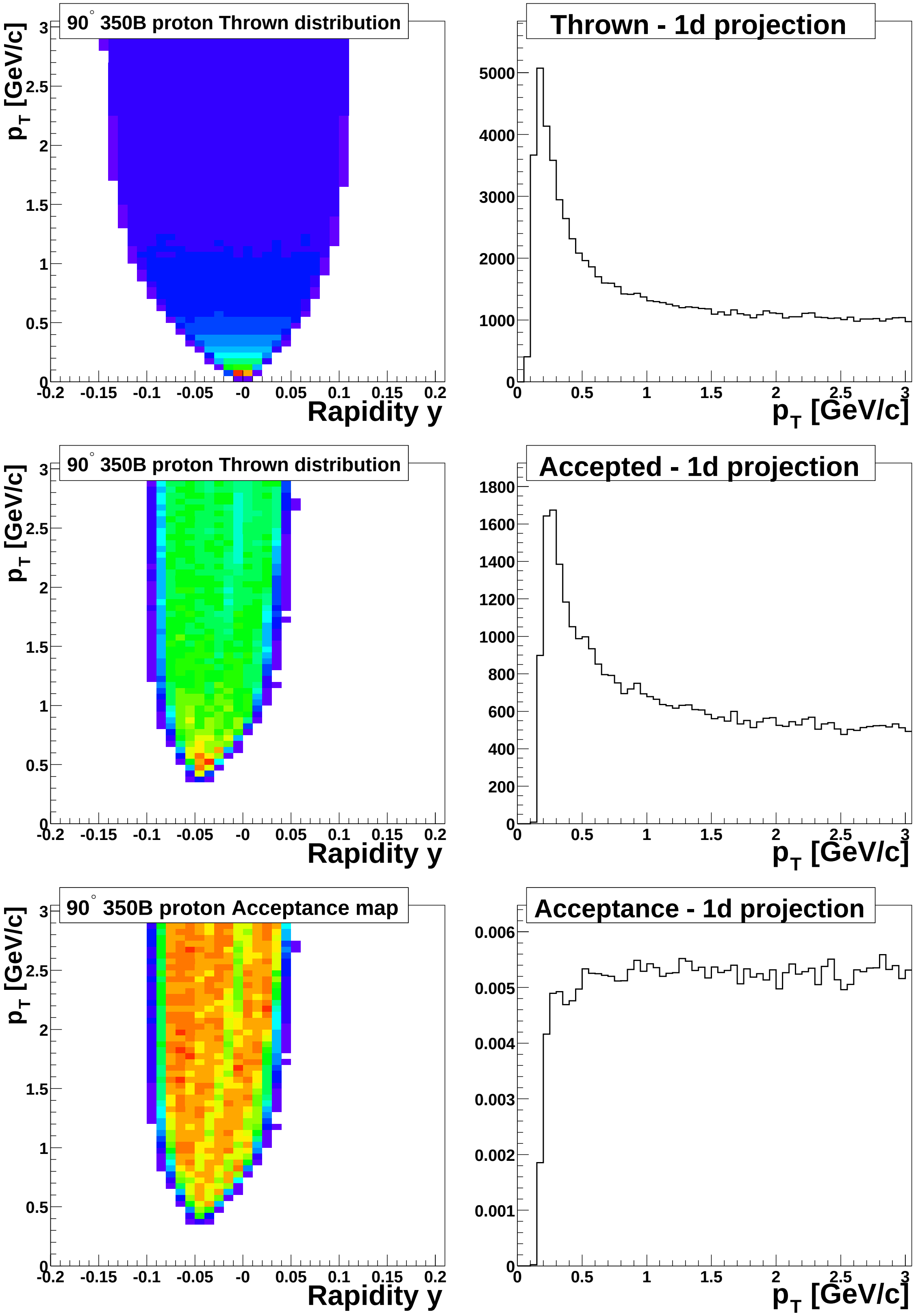

Figure 4.19: The construction of the Acceptance map. Top: The distribution of THROWN protons. Middle: ACCEPTED protons. Bottom: The final acceptance map (ACC).

the same).

Maps generated for positive particles can be used for negative particles for settings of opposite polarity, for which the magnitude of the field is the same, and vice versa.

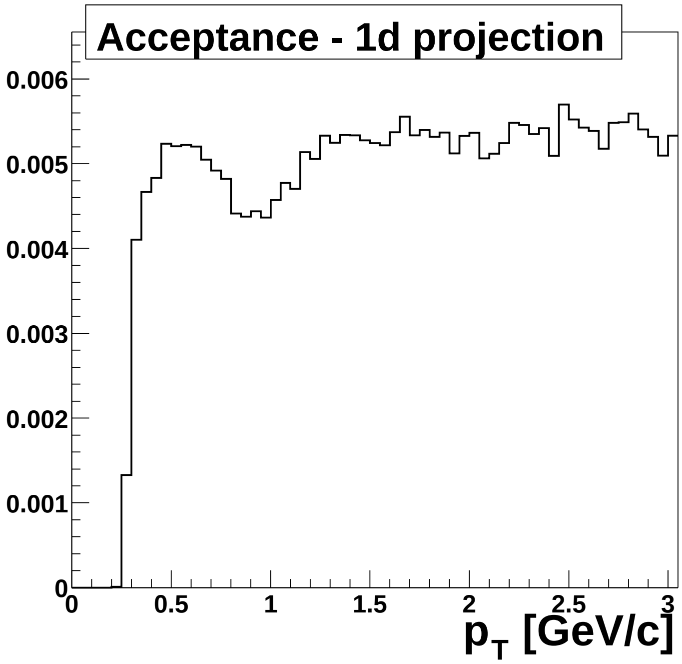

Figure 4.20: If no slat was missing the MRS acceptance would generally increase as a function of p_T, however around $p_T \sim 0.9$ GeV/c there is a small dip in the acceptance because particles in this narrow region of p_T (and rapidity) hit the TOF detector in the region where the bad slat is positioned.

To accept a track, some criteria have to be fulfilled similar to the selection cuts applied to the real data. There must be enough hits in the tracking detectors to reconstruct local tracks and all the local tracks have to "match" in the dipole magnets. The magnet fiducial cut applied to the real data (section 4.1.2) is also applied to the simulated data. If TOF is used for PID, missing slats are removed in the simulation (see Table 4.1). The effect of a missing slat is shown in Figure 4.20.

The acceptance has a strong dependence on the IP because both the θ and the ϕ coverage of the magnet aperture of the first magnet in each spectrometer depends on the IP.

4.4 Other Corrections

The proton and anti–proton data have to be corrected for multiple scattering (ms) and absorption (abs). Multiple scattering is the effect of repeated elastic Coulomb scatterings that can deflect particles in and out of the acceptance. Absorption happens when a proton or

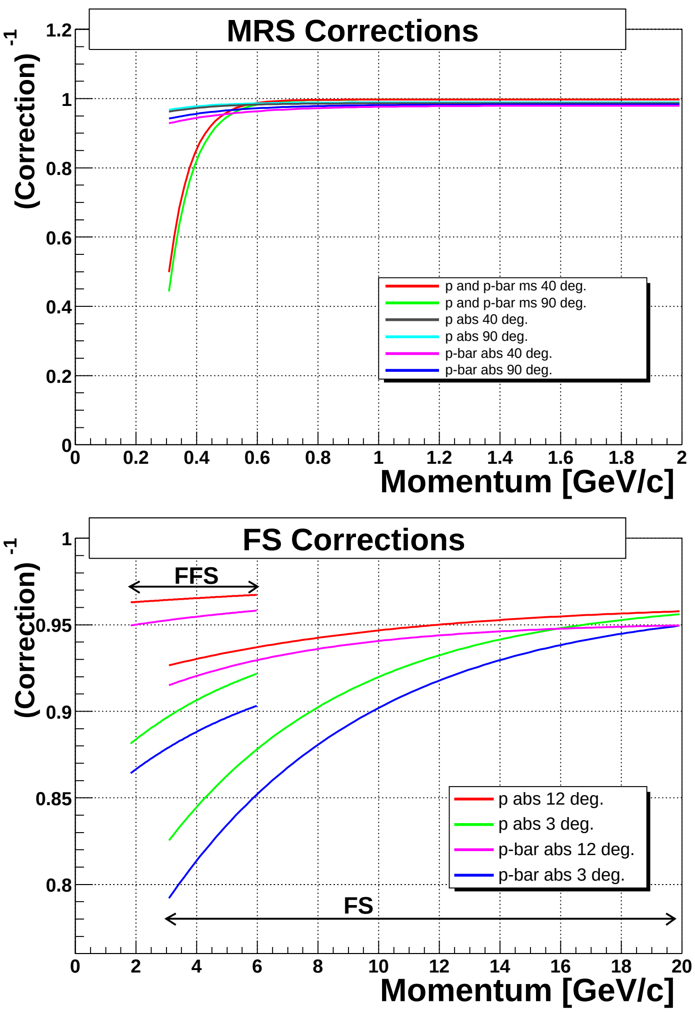

Figure 4.21: Top : Momentum dependence of the multiple scattering and absorption corrections for two MRS angles. Bottom : Momentum dependence of the absorption correction in FFS and FS. The FS simulation was limited to $p < 18$ GeV/c, so the momentum dependence above this is an extrapolation.

an anti–proton interact inelastically with the nuclei in the matter, on their way through the beam pipe and the detector. Both corrections are largest at small momenta.

Corrections for multiple scattering and particle absorption were done using the BRAHMS simulation tool BRAG (Appendix C). The corrections were obtained through the following steps.

- Simulation using single particles with and without the studied physical process
- Digitization of hits in detectors to include detector effects
- Track reconstruction using the data analysis chain
- Apply PID cuts
- Calculate the ratio of the two simulations and parameterize the correction

The corrections for multiple scattering were done for protons and applied to both protons and anti–protons. The FS multiple scattering correction was found to be of the order 0.1% and neglected. The absorption correction was done separately for protons and anti–protons in the MRS, FFS, and in the full FS. More details of the correction can be found in [55].

The momentum dependence of the corrections and the average correction at different spectrometer angles are illustrated in Figure 4.21. The MRS correction rises steeply for low momentum ¡ 0.4 GeV/c, and a cut is applied to the data to remove those tracks, see Table 4.4. In the FFS, the absorption correction is around 5–10 %, and largest at smaller spectrometer angles. The reason for this spectrometer angle dependence is scattering in the beam pipe where the path length through the pipe wall is almost four times longer at 3° than at 12°. At high momentum the beam pipe becomes “transparent” and the 3° and the 12° curves converges.

The effect of protons knocked out from the beam pipe was studied using HIJING simulation as input and the BRAG code to propagate the particles through the BRAHMS detector. Protons reconstructed in the MRS were studied to see if there was a background from protons knocked out from e.g. the beam pipe. As can be seen from Figure 4.22 the background produced by pions is negligible. A fiducial cut was performed on the HIJING distribution to reduce the CPU time, so that particles were only propagated in a solid angle subtending TPM1. As a consequence the large tail of protons observed in Figure 4.3 at large distances from the IP, is not seen in the simulation, but they are already rejected by the IP cut, see section 4.1.2. HIJING describes the overall charged multiplicity at mid–rapidity, which is dominated by pions, well [29], and it is therefore unlikely that the background should be much larger in the real data, hence this background is neglected in this analysis.

The background from Λ decays will be discussed in section 5.3.

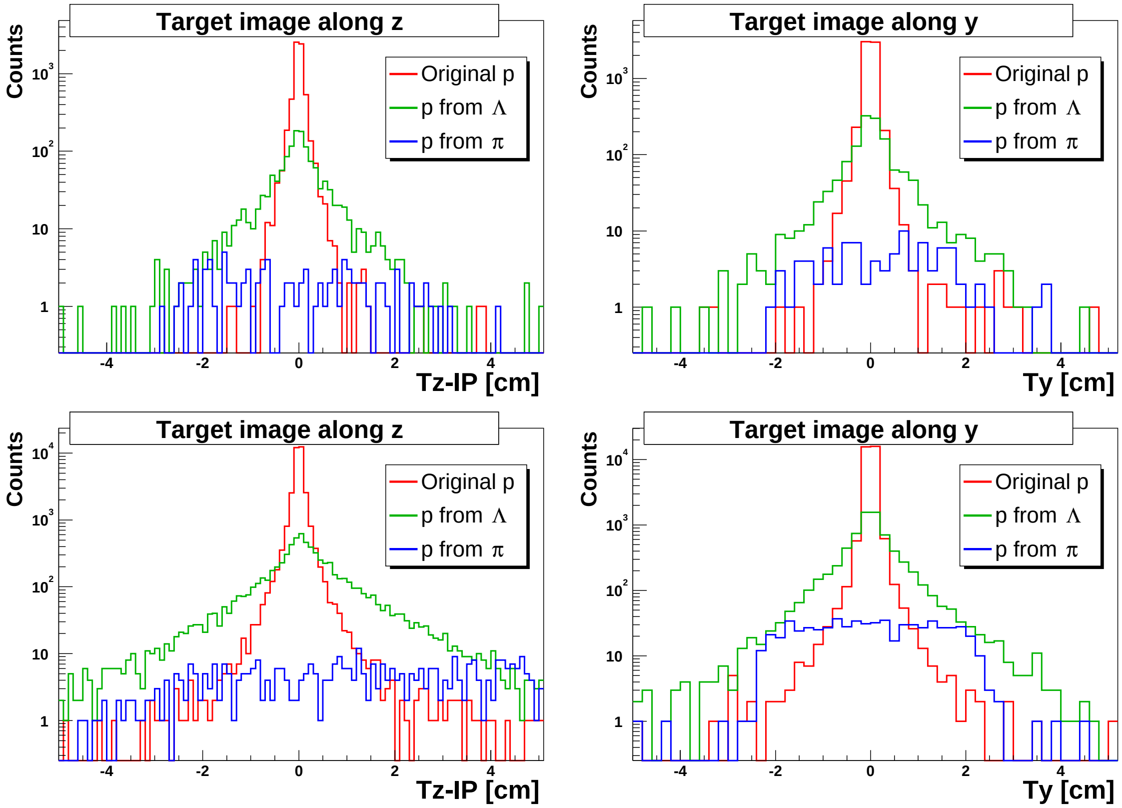

Figure 4.22: The target images of protons identified in the MRS from a HIJING simulation, found by projecting the TPM1 tracks to the beam plane. The plots are with the MRS positioned at 90° (top) and 35° (bottom).

4.5 Yields

The input to the yield calculations are the three histograms listed below :

- **Data**. The selected particles.
- **Acceptance**. Geometrical acceptance (including non-instrumented pads and slats) normalized to full 2π azimuthal coverage.
- **Correction and normalization**. Efficiencies, absorption, multiple scattering, and normalization to the number of events and bin sizes.

Tracks at the edge of the acceptance travel close to the edge of the magnets. They have the strongest IP dependence, and are most likely to have background problems from e.g. the magnet. A fiducial cut is applied to the edges of the acceptance maps illustrated in Figure 4.23. In the MRS where the acceptance correction approaches a constant value at high momentum (see Figure 4.19), the cut usually corresponds to 50–60 % of this value. In the FS where this is not the case, the cut is adjusted to remove the bins at the edge of the acceptance map. The cut is applied to all three histograms.

In the data selection only a certain range in momentum is used because of detector resolutions. To make the acceptance maps comparable with the data it is important to apply the same momentum range cut and remove the corresponding bins from all the histograms.

At low momentum the multiple scattering correction is rising steeply in the MRS, see Figure 4.21, and a momentum cut is used to remove data points where the correction changes rapidly over a single bin. For H1 a cut is applied to remove the low momentum data where the performance of the spectrometer is poorer.

The momentum cuts are shown in Table 4.4.

PID detector	Low cut [GeV/c]	High cut [GeV/c]
TOFW (MRS)	0.4	3.0
H1 (FFS)	2.0	4.0-5.0
H2 (FFS)	0.0	6.0-7.0
RICH (FS)	10.0	25.0

Table 4.4: The momentum cuts applied to all the histograms.

Now it is possible to calculate the 2–dimensional SPECTRUM$(y, p_T) = \frac{d^2N}{dy dp_T}$. The correction histogram (section 4.2) is divided by the acceptance histogram and normalized to per event and the histogram bin sizes. The resulting histogram CORR(y, p_T) then contains all corrections and normalizations including the geometric acceptance. The SPECTRUM(y, p_T) histogram is calculated as the product of the measured data and the correction (the multiplication is done cell by cell) :

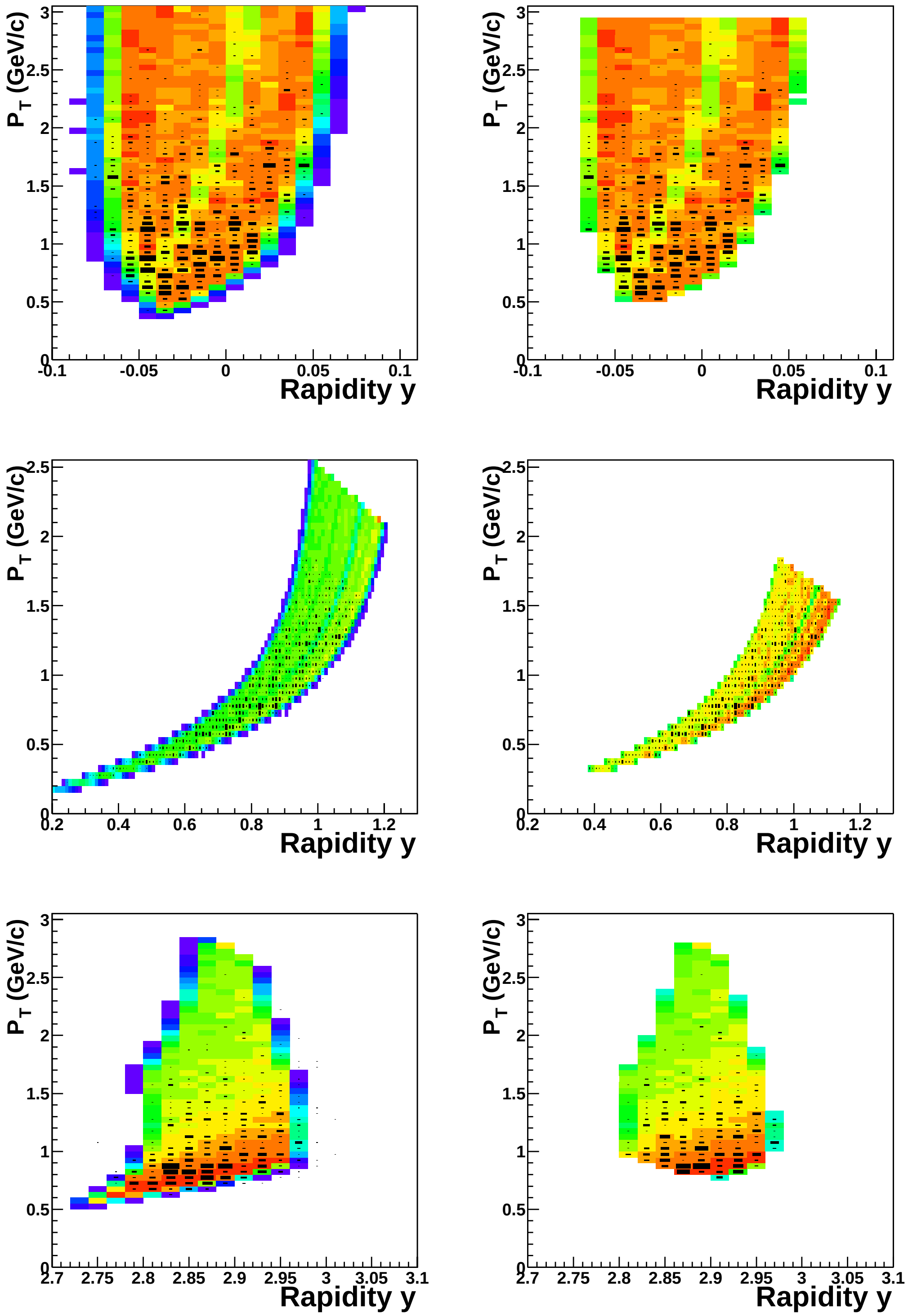

Figure 4.23: The measured data histogram overlaid on the acceptance maps for 3 settings. The acceptance map is colored and the data is black boxes. The left column is prior to any cuts. The right column displays the situation after the edges of the acceptance have been removed and the momentum cuts applied. The settings are from top to bottom : 90 degrees, 35 degrees and 4 degrees.

$$\mathrm{SPECTRUM}(y,p_T) = \mathrm{DATA}(y,p_T) \times \mathrm{CORR}(y,p_T) \tag{4.4}$$

The left hand side is $\frac{d^2N}{dp_T dy}$, i.e. the differential multiplicity per unit p_T and y, as collected in one particular setting of the spectrometer, characterized by spectrometer angle, field, and IP position. Several settings may give data to a particular (y,p_T) cell, and all such contributions should be taken into account by constructing a weighted average. The $\mathrm{DATA}(y,p_T)$ and corrections $\mathrm{CORR}(y,p_T)$ depend on the setting, and in the following this dependence is made explicit by adding an index s to identify a setting, so equation 4.4 in fact reads :

$$\mathrm{SPECTRUM}(y,p_T,s) = \mathrm{DATA}(y,p_T,s) \times \mathrm{CORR}(y,p_T,s) \tag{4.5}$$

the weights used in forming the average over settings are denoted $\mathrm{W}(y,p_T,s)$, and the average is then

$$\mathrm{AVG.SPECTRUM}(y,p_T) = \frac{\sum_s \mathrm{SPECTRUM}(y,p_T,s) \times \mathrm{W}(y,p_T,s)}{\sum_s \mathrm{W}(y,p_T,s)} \tag{4.6}$$

In this work the weights are chosen as

$$\mathrm{W}(y,p_T,s) = \frac{1}{\mathrm{CORR}(y,p_T,s)} \tag{4.7}$$

to ensure that entries with large corrections carry low weights. Equation 4.6 then becomes

$$\mathrm{AVG.SPECTRUM}(y,p_T) = \left(\sum_s \mathrm{DATA}(y,p_T,s)\right) \times \left(\sum_s \frac{1}{\mathrm{CORR}(y,p_T,s)}\right)^{-1} \tag{4.8}$$

a form that conserves the statistical distribution of the $\mathrm{DATA}(y,p_T,s)$. Other choices for the weights would not give the factorized form (4.8) and hence not the straight sum of contributing counts.

If the $\mathrm{SPECTRUM}(y,p_T,s)$ result for a cell is zero there can be two explanations. The correction factor $\mathrm{CORR}(y,p_T,s)$ could be zero, which means that the measurement does not include this region of phase space. The second explanation is that the data count $\mathrm{DATA}(y,p_T,s)$ is zero. If $\mathrm{CORR}(y,p_T,s) > 0$ this cell should not be ignored since it is a valid measurement with zero counts. This is important when settings are added or cells are averaged over to make projections. The weights used here, $\mathrm{WEIGHT}(y,p_T,s) = 1/\mathrm{CORR}(y,p_T,s)$ is valid even if $\mathrm{DATA}(y,p_T,s) = 0$, and can be interpreted as an effective number of events, see the discussion in Appendix G.

Because of the low counting statistics in most spectrometer settings the method of setting summation is crucial. Therefore the approach of making global correction histograms rather than track by track corrections was employed in this thesis. If track by track corrections had been implemented the reconstruction efficiency assigned for a track in the FS would have been exactly the estimated efficiency, rather than the momentum average as was done here, see section 4.2.2. The challenge would then be how to assign a correction for a region with no counts observed. Both methods have been attempted in the analysis process and good agreement was found, but in the end the global correction method was chosen because it simplifies the understanding of the correction histogram and the treatment of bins with zero counts. If the correction histogram was calculated based on simulated data, the track by track method is not statistical limited and would be superior.

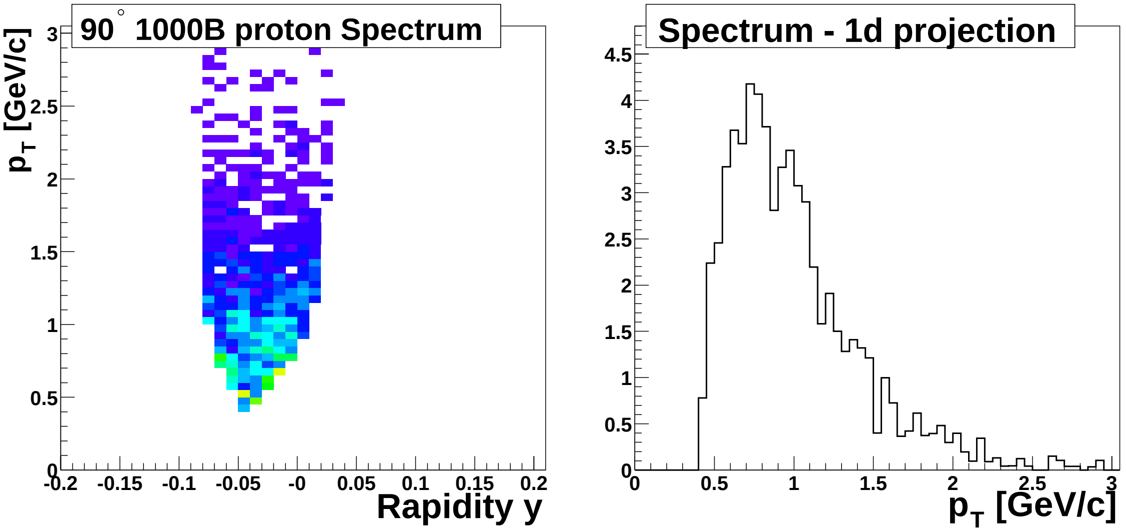

Figure 4.24: Proton spectrum in one setting and the projection for a short range in rapidity. By combining many settings and vertex bins the statistics can be increased.

In Figure 4.24 a SPECTRUM(y, p_T, s) histogram is shown.

Once the AVG.SPECTRUM(y, p_T) histogram is known, projections can be made in narrow rapidity intervals, the invariant yields $\frac{1}{2\pi p_T}\frac{d^2N}{dydp_T}$ constructed and the rapidity density determined.

The p_T spectrum in a narrow rapidity interval (usually $\Delta y \sim 0.1$) is constructed by averaging over several rapidity bins :

$$\text{AVG.SPECTRUM}(p_T) = \left(\sum_y \sum_s \text{DATA}(y, p_T, s)\right) \times \left(\sum_y \sum_s \frac{1}{\text{CORR}(y, p_T, s)}\right)^{-1} \quad (4.9)$$

Remember that CORR$(y, p_T, s) = 0$ outside the acceptance of the setting, and that these bins are ignored for both the data and the correction.

The invariant spectrum is subsequently given as :

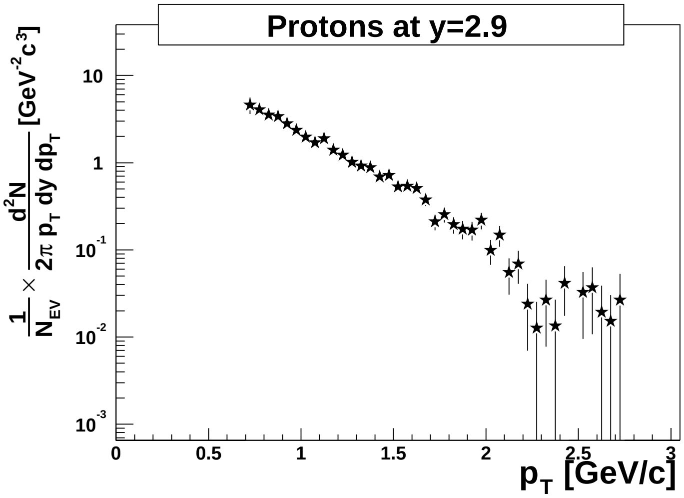

Figure 4.25: Proton spectrum at rapidity $y = 2.9$.

$$\frac{1}{2\pi p_T}\frac{d^2N}{dydp_T}(p_T) = \frac{\text{AVG.SPECTRUM}(p_T))}{2\pi p_T} \tag{4.10}$$

where the transverse momentum p_T is taken at the center of the histogram bin. In Figure 4.25 a proton spectrum at rapidity $y = 2.9$ is shown.

4.5.1 Extrapolating

At a given rapidity the proton spectrum is only measured in a limited range in transverse momentum. To extract the rapidity density dN/dy it is necessary to extrapolate from the range where the spectrum is measured, to the full interval. This extrapolation is accomplished by using a function assumed to describe the data in the full interval ($0 < p_T < \infty$). The function is fitted to the measured data points and the total rapidity density dN/dy is obtained by integrating the function (multiplied by p_T and 2π) from 0 to infinity.

Figure 4.26 illustrates the different extrapolations of functions (see Appendix E) that all fit the observed data well. As can be seen there can be large discrepancies in the region where no data is measured and this can lead to differences in the yields of 20 %.

In the next chapter, where the results are presented, the m_T–exponential is used to extrapolate the data, because it describes the data well at mid–rapidity *and* at forward rapidities, while the p_T–exponential only describes the data well at forward rapidity. The m_T–exponential fits pions, kaons, and protons reasonably well, where the Boltzmann distribution only works well for protons.

The functional expressions for all the functions can be found in the Appendix E. The

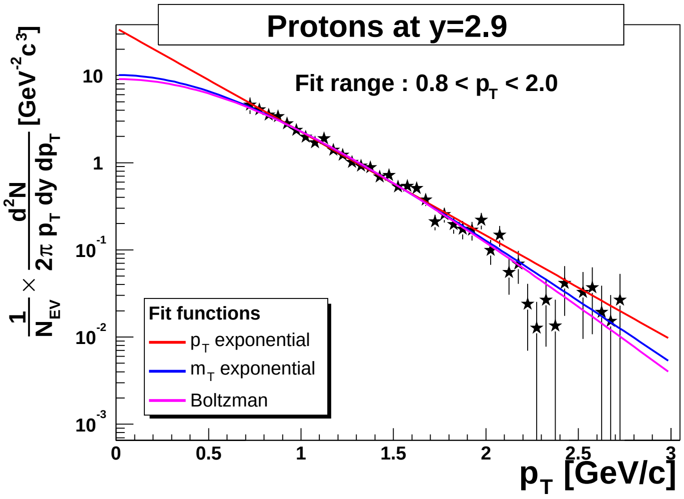

Figure 4.26: Proton spectrum at rapidity $y = 2.9$ fitted with three different fit–functions. The functions are difficult to distinguish in the measured data–range, but produces very different yields when extrapolated to low p_T.

exponential in m_T is parametrized as

$$f(m_T) = \frac{1}{2\pi}\frac{Y}{T(T+m)}e^{-\frac{m_T-m}{T}} \tag{4.11}$$

where T is the inverse slope parameter (also called the effective temperature) and Y is the integrated yield dN/dy under the fit function from $p_T = 0$ to $p_T = \infty$. The fits are done in ROOT [64] by using minimum χ^2 method.

4.6 Systematic Errors

The systematic errors are divided into two categories

- Settings. The error on the normalization of settings measuring the same phase space region.
- Extrapolation. The error introduced by fitting and extrapolating.

The systematic errors will be estimated from the data. More could be learned by studying the different pieces of the analysis separately and from detailed Monte Carlo studies, but that is beyond the time frame for this work.

Primarily the systematic errors on dN/dy will be discussed. The systematic errors will be estimated for three rapidity regions : MRS data points ($0 < y < 1$), the $y \sim 2$ FS data points, and the $y \sim 3$ FS data points.

Settings

By comparing the number of protons and anti–protons obtained from different angular and field settings that covers the same phase space, an estimate of the systematic error on the number of protons in a single setting can be obtained. At 90, 40, and 3-4 degrees there are many overlapping settings (six, six, and four, respectively) and by constructing the transverse momentum spectra in a narrow rapidity interval and summing up the counts in a p_T range covered by all the spectra, different measurements of the same quantity is obtained. Next, the weighted mean of the dN/dy measurements is constructed (exploiting one degree of freedom) and the χ^2 is derived.

y/p_T interval	dN/dy weighted	χ^2 / Ndof	p	α	σ_{scaled}
$-0.05 < y < 0.05$	22.4 ± 0.35	5.44 / 5	36 %		0.57
$0.4 < p_T < 2.0$	16.5 ± 0.28	15.84 / 5	0.7 %	1.27	0.46
$0.75 < y < 0.95$	12.5 ± 0.22	14.84 / 5	1.1 %		0.59
$0.7 < p_T < 1.5$	8.2 ± 0.19	12.24 / 5	3.2 %	1.30	0.56
$2.75 < y < 3.10$	7.0 ± 0.13	72.5 / 3	< 0.01 %		1.3
$0.8 < p_T < 1.7$	1.88 ± 0.07	29.4 / 3	< 0.01 %	4.00	0.70

Table 4.5: The results of the comparison between settings. For each setting the first line in the table is for protons and the second is for anti–protons. p is the probability $P(\chi^2 > \chi^2_{measured})$, and α is the derived systematic error scale factor for the setting (same for protons and anti–protons) and σ is the derived total systematic error, see text.

Table 4.5 show the results from the comparison between settings. The probabilities for having $\chi^2 > \chi^2_{measured}$ shows that the statistical errors alone are not enough to describe the difference between settings.

A systematic error that scales with the statistical error is added so that the total χ^2 in a phase space region becomes

$$\chi^2 = \sum_i \frac{(Yp - Yp_i)^2}{\sigma^2_{Yp_i}(1+\alpha^2)} + \sum_i \frac{(Y\bar{p} - Y\bar{p}_i)^2}{\sigma^2_{Y\bar{p}_i}(1+\alpha^2)} \tag{4.12}$$

where Yp is the protons dN/dy and $Y\bar{p}$ is the anti–proton dN/dy. α is then adjusted so the reduced χ^2 is 1. The systematic error is then $\sigma = \alpha\sigma_{stat}$.

The systematic error obtained in this way depends on the yield in the covered range i.e., it scales with the yield. To estimate total systematic errors for protons and anti–protons the systematic error is therefore scaled with a typical value in the rapidity region e.g. for MRS protons at 90 degrees $\sigma_{scaled} = 1.27 \times 0.35 \times 28.5/22.4 \sim 0.57$. The remaining systematic errors are shown in Table 4.5. Since no overlapping settings are available for the $y \sim 2$ points, the $y = 3$ systematic errors are scaled to the higher proton and anti–proton yields in that rapidity region, and $\sigma_{scaled} \sim 2.1$ is found for both protons and anti–protons.

Extrapolation

The systematic error on the extrapolation is studied by varying

- Bin size. Normally 100 MeV bins are used in the final p_T-spectrum to improve the statistics in each bin, but instead 50 MeV bins are used.
- Fit function. Instead of the m_T exponential fit function a Boltzmann function is used. The temperature from the Boltzmann fit is not comparable to the temperature in the exponential so this variation is only done to study the effect on dN/dy.
- Fit range. Two variations are done. In the first variation the low range is increased by 100 MeV and in the second, the high range is decreased by 100 MeV.
- Rapidity interval. In the first variation the p_T spectrum is calculated without the first rapidity bin and in the second variation without the last.

The systematic error is then estimated as

$$\sigma_{syst} = \sqrt{\sum_i (x - x_i)^2} \tag{4.13}$$

where x_i is the value (dN/dy or T) obtained from variation i and x is the original result.

spectrometer	dN/dy syst.	T syst. (MeV)
MRS ($0 < y < 1$)	0.8	9
FS (y=2)	1.5	13
FS (y=3)	1.2	36

Table 4.6: The systematic variations of dN/dy and T in all rapidity intervals. The procedure is described in the text.

Figure 4.27 shows the variation for protons in a single rapidity interval at mid–rapidity. The systematic errors were estimated for both protons and anti–protons in all the rapidity intervals used in this analysis. The systematic variation for protons and anti–protons are similar so the systematic error for the three rapidity regions have been calculated by averaging over proton and anti–proton errors for all rapidity settings in each subset. The systematic variations are shown in Table 4.6.

Summary

The systematic error on protons and anti–protons have been estimated from the data for the three rapidity regions. For the total systematic error it is assumed that the systematic errors on the normalization of the settings and the extrapolation are independent so that $\sigma^2_{syst} = \sigma^2_{norm} + \sigma^2_{extra}$.

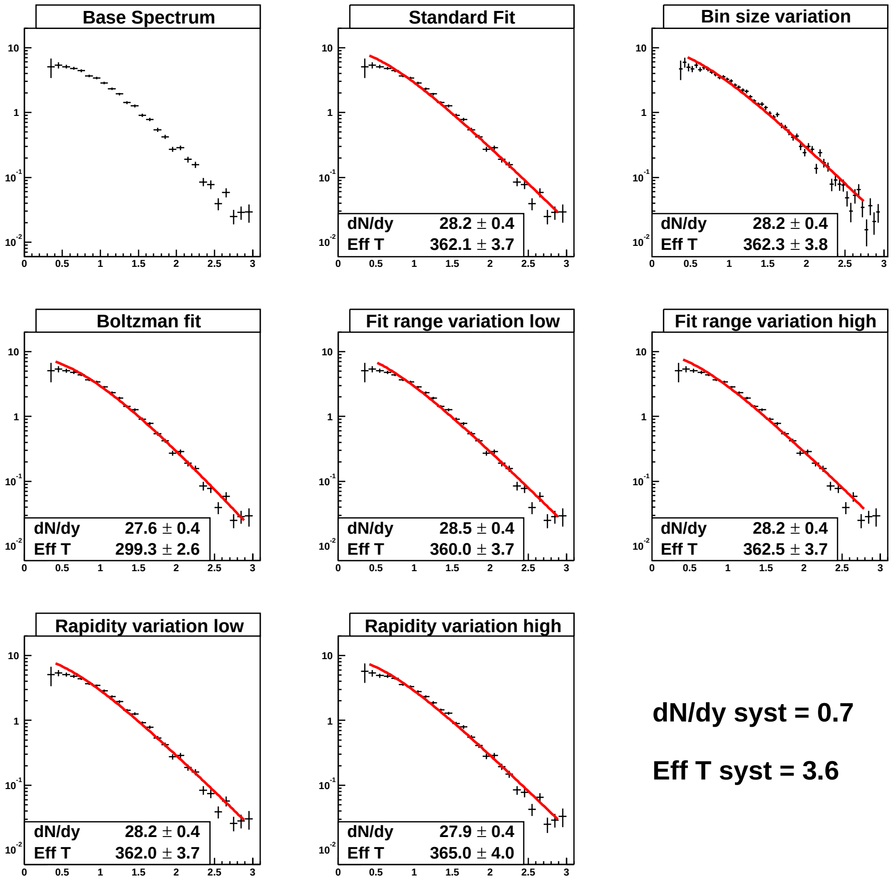

Figure 4.27: The plot shows the invariant spectrum at $y = 0$. Many variations described in the text are done to see if the result of the fit is stable.

The total systematic errors on dN/dy is then $\sigma_{syst} = 1.0$ for protons and $\sigma_{syst} = 0.9$ for anti–protons in the MRS. At $y \sim 2$ proton and anti–proton systematic errors are similar, $\sigma_{syst} = 2.6$, and at $y = 3$ the systematic error is $\sigma_{syst} = 1.8$ for protons and $\sigma_{syst} = 1.4$ for anti–protons.

The systematic errors on the net–protons are estimated to be of the same order as for the respective protons and anti–protons (instead of a factor $\sim \sqrt{2}$ larger), because it is observed that some of the systematics cancel when the anti–protons are subtracted from the protons.

The systematic error estimated in this way is a minimum error. If there are systematics in the normalization that shift all points up or down at a rapidity, they will not be included in this estimate.

Chapter 5

Results

In this chapter the results from the analysis described in the previous chapter will be presented and compared to data from other experiments and to models.

5.1 BRAHMS Results

Figure 5.1 and Figure 5.2 show the acceptance of the spectrometer settings used in this analysis. The rapidity intervals used for projections are illustrated with black lines on the figures. The MRS settings cover most of the rapidity range $-0.1 \leq y \leq 1$, and dN/dy can be obtained in this region for several rapidity values. In the FS the coverage is obtained by using several settings and PID methods. The settings at $y \sim 2$ are difficult to handle, because the p_T acceptance in a narrow rapidity interval is limited for a single setting and the statistics in these settings is low. The projections have therefore been done in broad rapidity intervals. The many projections at rapidity $y = 3$ were made to get as many independent measurements as possible to fix this point, which is at the edge of the coverage and therefore the link to extrapolate the rapidity dependence to higher rapidities.

BRAHMS measures protons in the rapidity interval $0.0 < y < 3.0$ only, but since the beam and target are the same particle species ($Au + Au$), the rapidity densities dN/dy are symmetrical around mid–rapidity, enabling the results to be symmetrized to cover $-3.0 < y < 3.0$.

The results presented here are for inclusive protons and anti–protons. This means that no attempt has been done at this point to separate protons from hyperon decays (e.g. $\Lambda \rightarrow p\pi^-$) from original protons. In section 5.3 this will be discussed in more detail.

Figure 5.3 shows the transverse momentum spectra for selected rapidities at $y \sim 0, 1, 2, 3$. In Appendix H all the proton and anti–proton transverse momentum spectra for the top 0-5 % central data are shown. The p_T coverage is different for each rapidity, meaning that the fraction of the total yield covered depends on the rapidity. The coverage ranges from ~ 85 % at mid–rapidity to ~ 40 % at the most forward rapidity, and is measured relative to the total

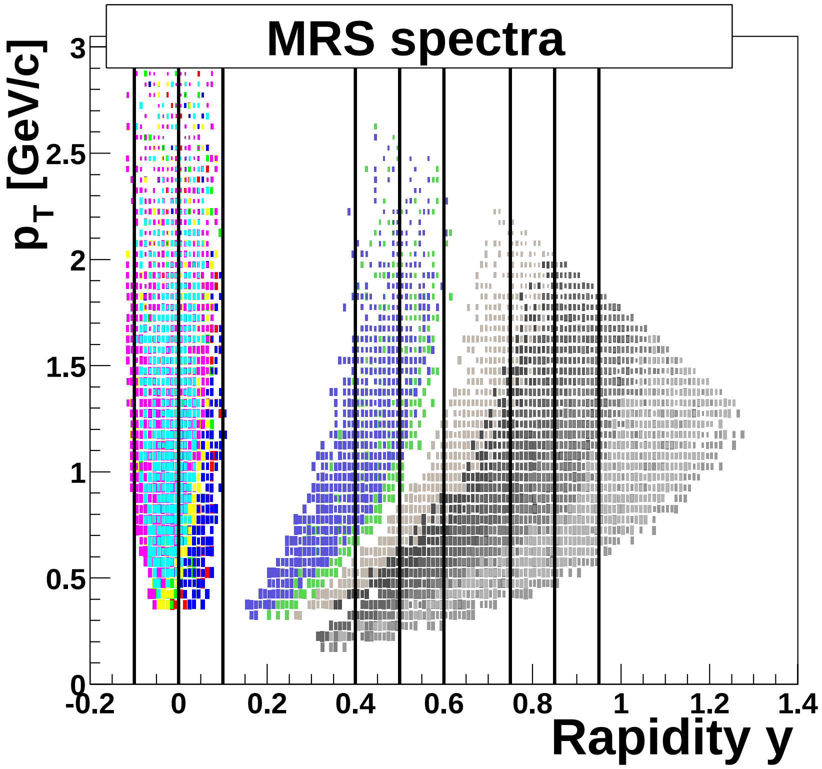

Figure 5.1: The phase–space (y, p_T) covered by the MRS with the settings used here ($\theta \sim 90, 60, 45, 40, 35, 30$). The black lines illustrate the rapidity intervals used for the projections. Each color in the plot corresponds to a different setting.

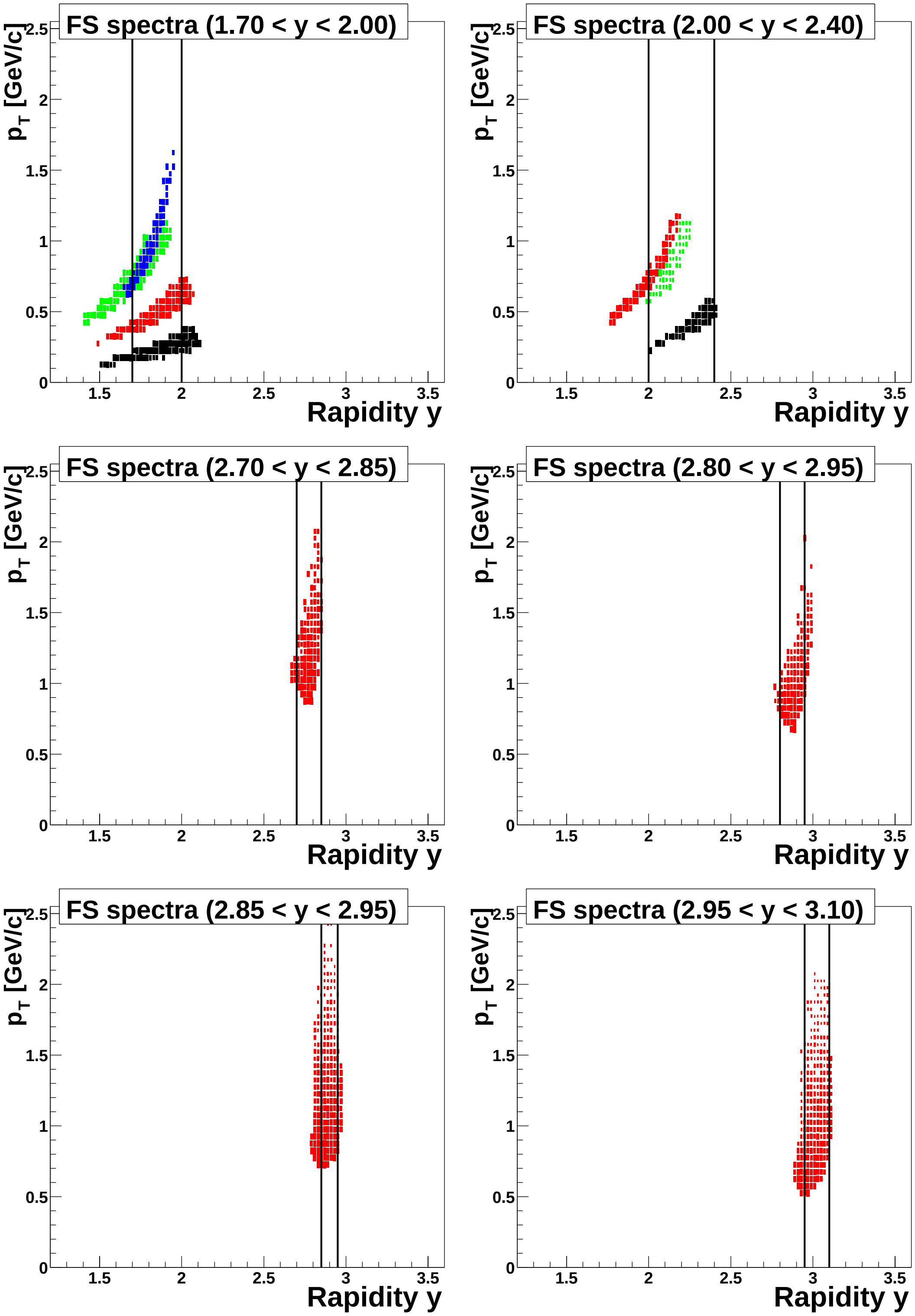

Figure 5.2: The phase–space (y, p_T) covered by the FS with the settings used here. The black lines illustrate the rapidity intervals used for the projections. The data used for the two projections at $y \sim 2$ are from TOF identification with H1 and H2 ($\theta \sim 12, 8, 4$). The PID for all the data samples at $y \sim 3$ was done with the RICH detector ($\theta \sim 4, 3$). In each plot different settings have different color.

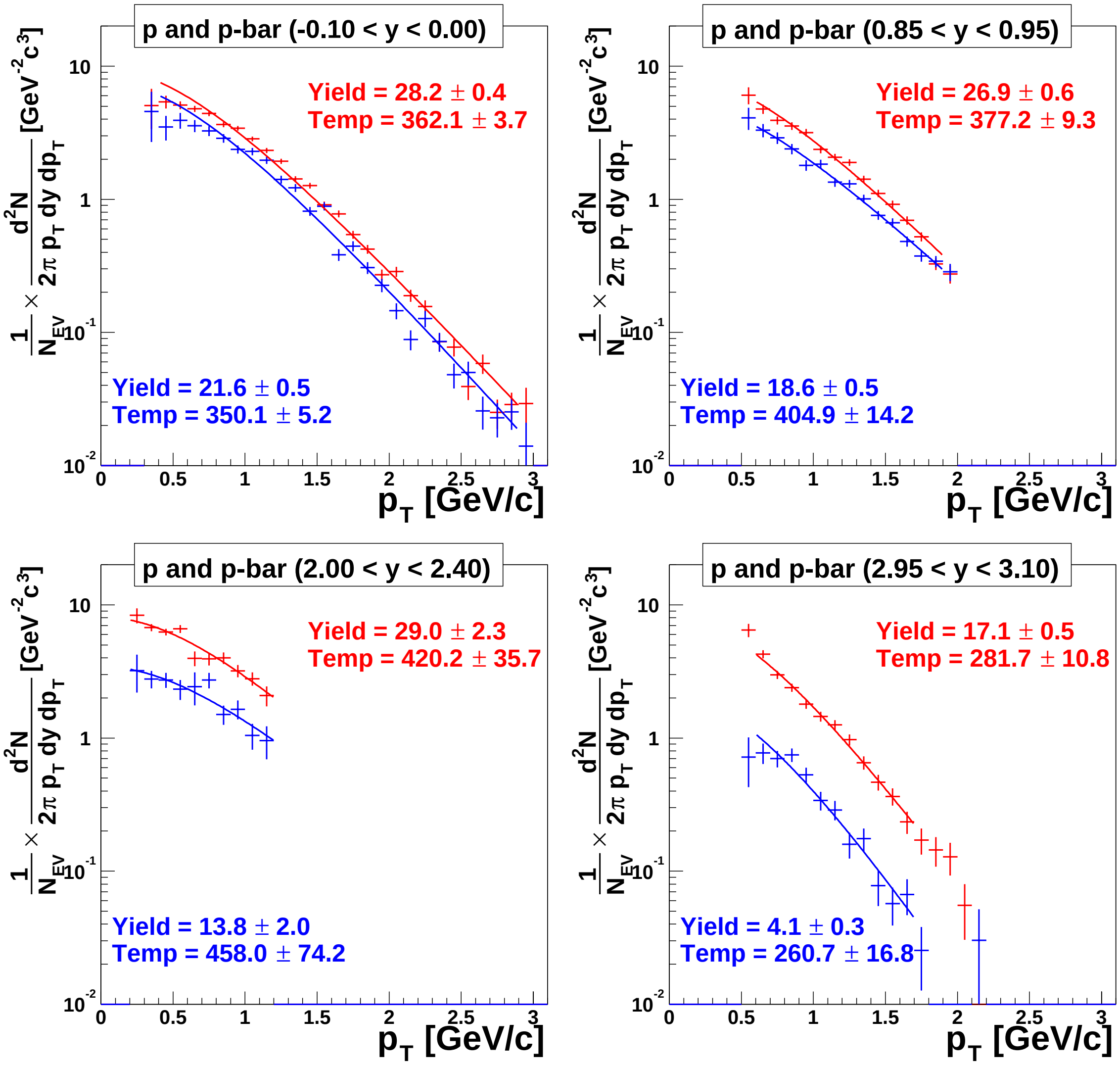

Figure 5.3: Transverse momentum spectra for protons (red) and anti–protons (blue) at selected rapidities $y \sim 0, 1, 2, 3$. The fits to the data are shown as curves. Error bars and errors on yield and temperature are statistical only.

area under the fit function from $p_T = 0$ to $p_T = \infty$, see Table 5.1. The fit function used is the exponential in m_T (equation 4.11), and the fit range has been chosen to be identical for protons and anti–protons even though the statistics at times allow the fit range to be extended for one of the particles (usually protons). This is to attempt to reduce the effect of the fit function choice on the result.

The fits generally describe the data well. The χ^2 per degree of freedom ranges from 0.5 to 4 and it is important to remember that only statistical errors have been included in the spectra, while often many settings, which might have systematic differences (section 4.6), are grouped together to form a single spectrum. The χ^2 per degree of freedom is largest for settings where low p_T ($p_T < 0.5$ GeV/c) is covered. At low p_T the spectra are very flat compared to the fit and the points are in general below the fit function, so the fit function does not seem to provide a good description of the data over the full p_T range. However, for these settings the p_T coverage is large, covering 60-90 % of the extrapolated yield, so the extrapolation to the total yield is smaller than for settings with more limited p_T coverage, where the fit describes the data better. In the measured p_T interval there is good agreement between the yield dN/dy found in the fit range by summing the measured spectra (no fitting) and the yield given by integrating the fit function in the same restricted range, indicating that even though the fit description is not perfect, the extrapolated rapidity densities obtained are accurate.

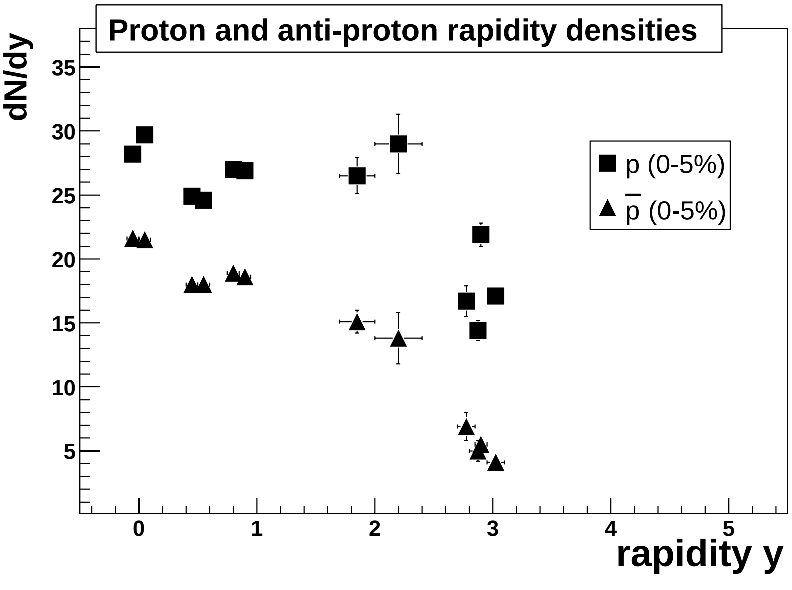

Figure 5.4: Integrated yields dN/dy as a function of rapidity for protons and anti–protons for 0-5 % centrality. Error bars are statistical only.

Figure 5.4 shows the rapidity dependence of the yields dN/dy for the most central (0-5%) selection of protons and anti–protons. The dN/dy is found by extrapolating the fit function

y interval	fit range	dN/dy	T (MeV)	χ^2/Ndof	$(dN/dy)^{counting}_{fitrange}$	$(dN/dy)^{fit}_{fitrange}$	$(dN/dy)^{counting}_{fitrange}/(dN/dy)$
$-0.10 < y < 0.00$	$0.4 < p_T < 2.9$	28.2 ± 0.4	362 ± 4	100.6/23	23.2 ± 0.3	23.7	82 %
		21.6 ± 0.5	350 ± 5	87.0/23	17.4 ± 0.4	18.1	80 %
$0.00 < y < 0.10$	$0.4 < p_T < 2.9$	29.7 ± 0.7	357 ± 5	57.7/23	23.8 ± 0.6	24.9	80 %
		21.5 ± 0.3	368 ± 5	92.5/23	17.6 ± 0.3	18.1	82 %
$0.40 < y < 0.50$	$0.3 < p_T < 2.5$	24.9 ± 0.6	369 ± 8	38.7/20	23.2 ± 0.6	22.2	93 %
		18.0 ± 0.5	390 ± 10	44.3/20	17.1 ± 0.5	16.0	95 %
$0.50 < y < 0.60$	$0.3 < p_T < 2.4$	24.6 ± 0.6	352 ± 8	41.4/19	23.0 ± 0.7	21.8	93 %
		18.0 ± 0.5	383 ± 11	28.2/19	16.3 ± 0.6	15.9	91 %
$0.75 < y < 0.85$	$0.5 < p_T < 2.1$	27.0 ± 0.4	372 ± 7	23.9/14	19.5 ± 0.3	19.7	72 %
		18.9 ± 0.4	389 ± 9	24.4/14	13.5 ± 0.3	13.9	71 %
$0.85 < y < 0.95$	$0.6 < p_T < 1.9$	26.9 ± 0.6	377 ± 9	20.3/11	16.9 ± 0.3	16.9	63 %
		18.6 ± 0.5	405 ± 14	8.7/11	11.8 ± 0.3	11.8	63 %
$1.70 < y < 2.00$	$0.2 < p_T < 1.6$	26.5 ± 1.4	420 ± 24	26.6/12	20.1 ± 0.9	20.6	76 %
		15.1 ± 0.9	478 ± 35	28.0/12	10.4 ± 0.5	11.0	69 %
$2.00 < y < 2.40$	$0.2 < p_T < 1.2$	29.0 ± 2.3	420 ± 36	11.3/8	17.7 ± 0.6	17.7	61 %
		13.8 ± 2.0	458 ± 74	7.1/8	8.1 ± 0.5	7.9	59 %
$2.70 < y < 2.85$	$0.8 < p_T < 1.8$	16.7 ± 1.2	295 ± 23	4.8/8	6.9 ± 0.4	6.8	41 %
		6.9 ± 1.1	217 ± 23	10.9/8	2.2 ± 0.2	2.1	31 %
$2.80 < y < 2.95$	$0.7 < p_T < 1.5$	14.4 ± 0.8	299 ± 41	8.3/6	6.8 ± 0.4	6.4	47 %
		5.0 ± 0.8	202 ± 32	7.8/6	1.8 ± 0.2	1.8	36 %
$2.85 < y < 2.95$	$0.8 < p_T < 1.7$	21.9 ± 0.9	293 ± 14	8.9/7	8.7 ± 0.3	8.6	40 %
		5.5 ± 0.4	331 ± 34	3.5/7	2.3 ± 0.1	2.3	42 %
$2.95 < y < 3.10$	$0.6 < p_T < 1.7$	17.1 ± 0.5	282 ± 11	6.6/9	9.7 ± 0.3	9.6	57 %
		4.1 ± 0.3	261 ± 17	11.2/9	2.3 ± 0.1	2.2	55 %

Table 5.1: The results of the fits to the proton and anti–proton p_T–spectra for the 0-5 % central data. The errors are statistical only. In each rapidity interval the proton results are presented in the top row, and the anti–proton results are presented in the bottom. The last three columns show the yield in the fit range calculated from the data (no fit), the yield in the fit range given by the fit, and the fraction of the counted yield to the total yield i.e., the coverage of the setting.

from $p_T = 0$ to $p_T = \infty$. The dN/dy values quoted in the following are the weighted average of the two points at $y \sim 0$, and the weighted average of the four points at $y \sim 3$. The proton distribution decreases from $dN/dy(y = 0) = 28.6 \pm 0.3$ to $dN/dy(y = 3) = 17.3 \pm 0.4$, and the anti–proton distribution decreases from $dN/dy(y = 0) = 21.5 \pm 0.3$ to $dN/dy(y = 3) = 4.7 \pm 0.2$.

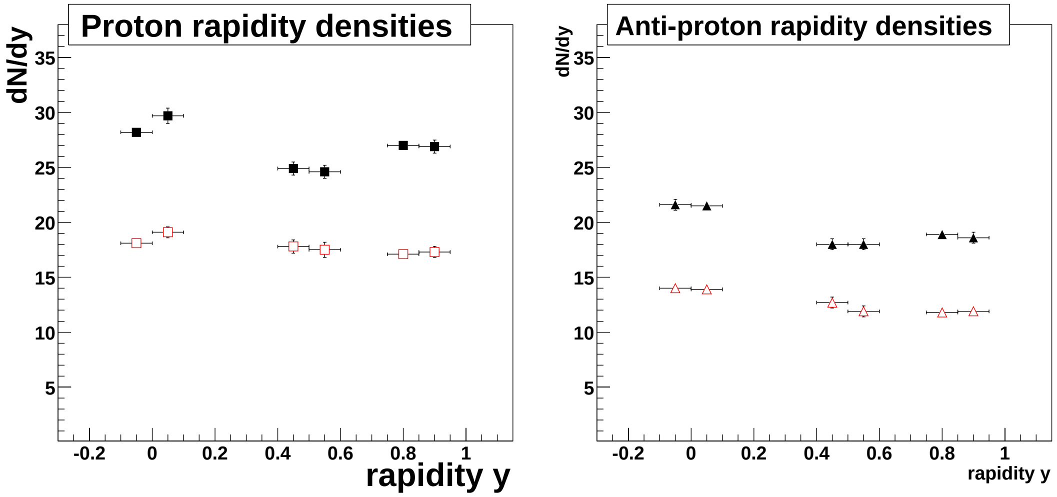

Figure 5.5: Comparison between the rapidity densities obtained for protons (left) and anti–protons (right) from fits (black) and those obtained by summing the p_T spectrum in the range $0.5 < p_T < 1.6$ (red).

In the rapidity density spectrum of both protons and anti–protons the two points at $y \sim 0.5$ seem to be systematically lower than the close points at $y \sim 0$ and $y \sim 1$. It is interesting to notice that for those points the counted yield in Table 5.2 is systematically larger than the fitted yield whereas the opposite is true for *all* the other MRS settings. This suggests that the dip in the rapidity distributions comes from systematics related to the fitting procedure. This can be tested by comparing the yields obtained by summing the p_T spectra in the p_T region, $0.5 < p_T < 1.6$ GeV/c, which is covered by all the MRS settings. Figure 5.5 shows such a comparison and the near constant yield for the straight sums indicates that the problem is related to the extrapolation.

The BRAHMS experiment has already published the rapidity dependence of $\bar{p}/p$ ratios at $\sqrt{s_{NN}} = 200$ GeV [57]. The published ratios are determined in a very different way, described in the following, than in the analysis used here. If two settings with the same angle and magnitude of the magnetic field, but opposite polarity are compared, most of the corrections that have been used here cancel i.e., acceptance, multiple scattering, tracking efficiency, and PID efficiency. Consequently the ratio of anti–protons (from one setting) to protons (from the other setting) normalized to per event, only has to be corrected for the absorption difference between protons and anti–protons. For any given setting the ratios

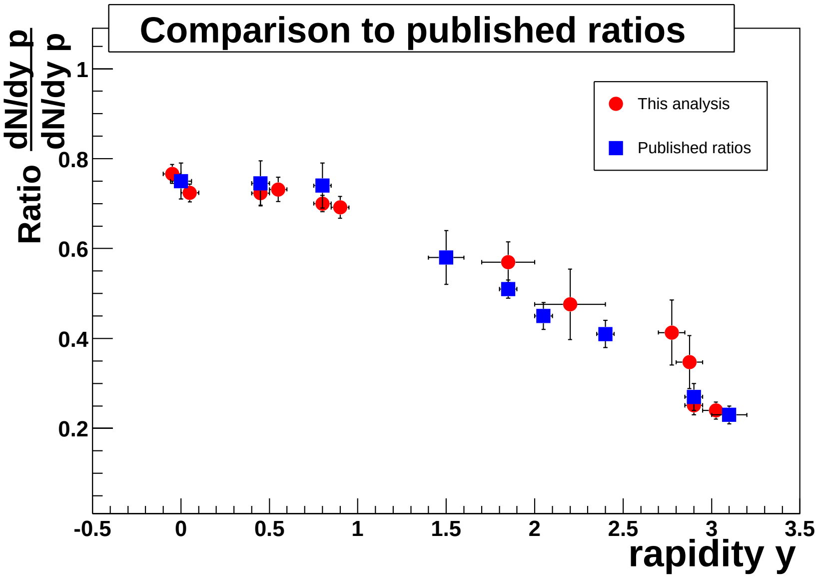

Figure 5.6: The ratio of dN/dy for anti–protons to protons, compared to the ratios published at $\sqrt{s_{NN}} = 200$ GeV, by the BRAHMS collaboration.

were observed to have no dependence on transverse momentum (consistent with the almost identical proton and anti–proton slopes observed at each rapidity in Figure 5.7), so that the ratio is characterized by a single p_T independent number at a given rapidity. The ratio of the yields from this analysis can be compared to the published ratios, and as can be seen in Figure 5.6 the two different methods of analysis give consistent results.

Figure 5.7 shows the inverse slope parameters extracted from the fits. The proton and anti–proton slopes are comparable at all rapidities indicating that the sources of protons and anti–protons are similar i.e., there is no visible difference between the protons from pair–production and from fragmentation of initial nucleons. The inverse slope seems constant in the interval around mid–rapidity ($0 < y < 1$), increases at $y = 2$ and then drops at $y = 3$. The rise at $y = 2$ could be a systematic effect of the fit–range, because for these points the p_T coverage extends lower (down to $p_T \sim 0.2$ GeV/c) than at other rapidities, and does not reach p_T values attained at other rapidities.

The net–proton dN/dy can be found by subtracting the anti–proton yield from the proton yield. Figure 5.8 shows the rapidity dependence of the net–proton yields dN/dy for the most central (0-5%) selection. The net–proton distribution increases from $dN/dy(y = 0) = 7.3 \pm 0.5$ to $dN/dy(y = 3) = 12.9 \pm 0.4$. The rise in the net–proton distribution can also be seen in Figure 5.4, where the proton distribution is broader than the anti–proton distribution. The shape of the distribution, with a minimum at mid–rapidity and a slow rise toward forward rapidity, indicates that at RHIC there is a high degree of transparency in even the most central collisions. This observation verifies an important assumption in the Bjorken picture

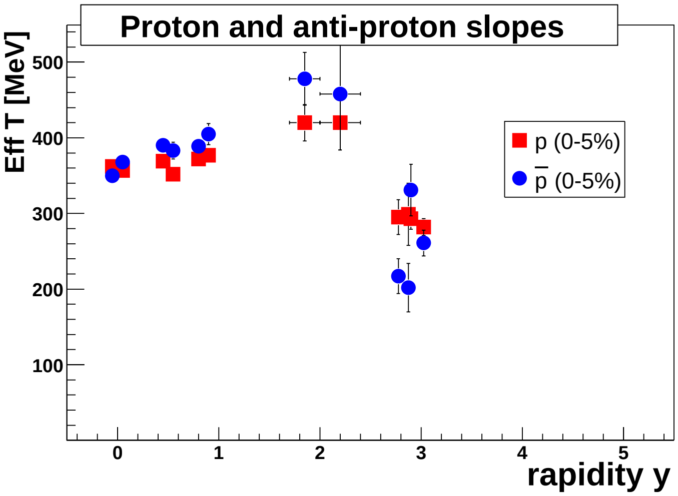

Figure 5.7: The effective temperature (inverse slope) as a function of rapidity for protons and anti–protons, as a function of rapidity. The errors are statistical only.

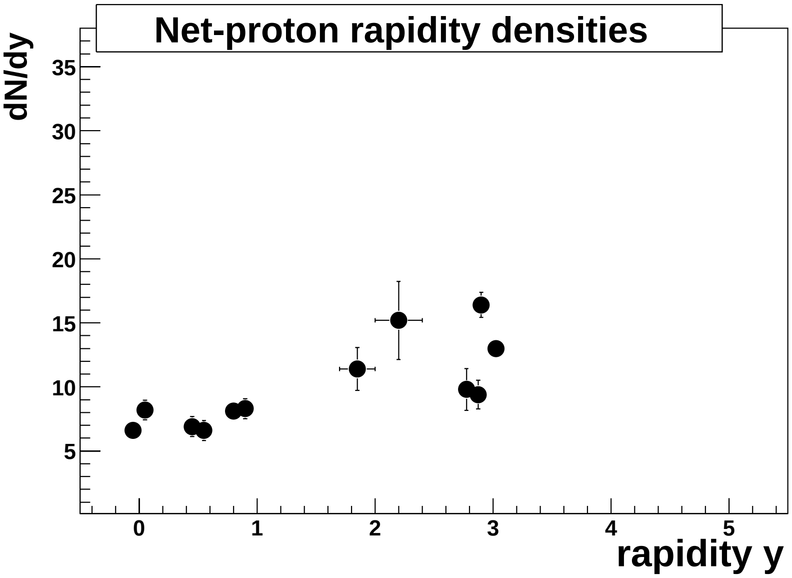

Figure 5.8: Net–proton yields (dN/dy) as a function of rapidity for 0-5 % centrality. Error bars are statistical only.

(section 1.3.2). The observation that there is practically boost invariance around mid–rapidity indicates that this assumption is also fulfilled, and the expression derived for determining the Bjorken estimate of the initial energy density, equation 1.4, should therefore be meaningful at RHIC energies.

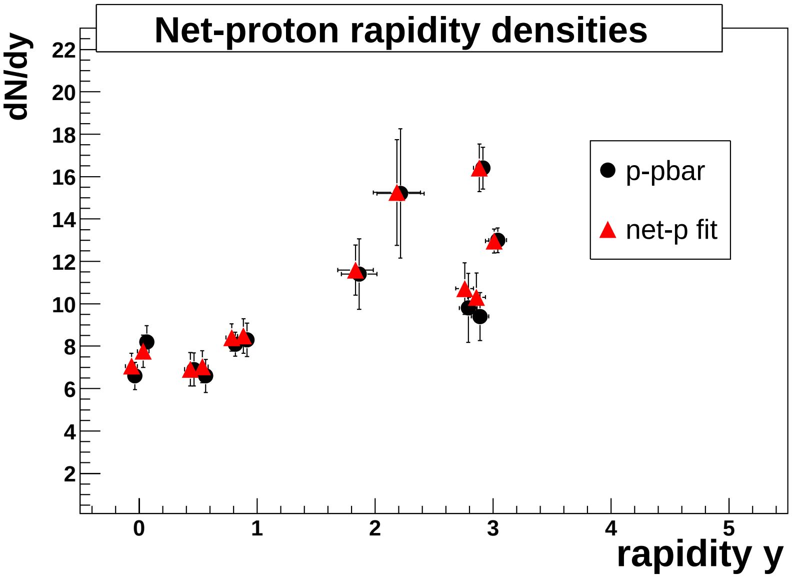

Figure 5.9: Comparison of the net–proton yield obtained by subtracting the anti–proton yield from the proton yield ($p-\bar{p}$) to the yield obtained by subtracting the anti–proton p_T spectrum from the proton p_T spectrum and then fitting (net-p fit). Error bars are statistical only.

The net–proton yield may also be determined by subtracting the anti–proton p_T spectrum from the proton p_T spectrum and then fitting the net–proton p_T–spectrum. The fit function used here is the same as for the proton and anti–proton fits i.e., a m_T exponential. The fits are all shown in Appendix H. Figure 5.9 shows the comparison between net–proton rapidity densities obtained with the two methods. The results are very similar indicating that the two methods are consistent. The statistical errors on the net–proton yields obtained with the latter method are comparable to those obtained from the first method.

The centrality dependence of the yields has also been studied. Table 5.2 and Table 5.3 shows the results obtained for 5-10 %, and 10-20 %, respectively. To make the data more visual, data points have been added by taking the weighted average. In Figure 5.10 the centrality dependence of the yields is shown for protons, anti–protons, and net–protons. At any given rapidity the proton and anti–proton yields are decreasing from central (0-5%) to less central collisions (10-20%).

The ratio of proton, anti–proton, and net–proton yields measured in 10-20 % central collisions to those measured in 0-5 % collisions are also shown. At any given rapidity the drop is similar for all three ratios, except for rapidity $y = 3$ where the protons and net–

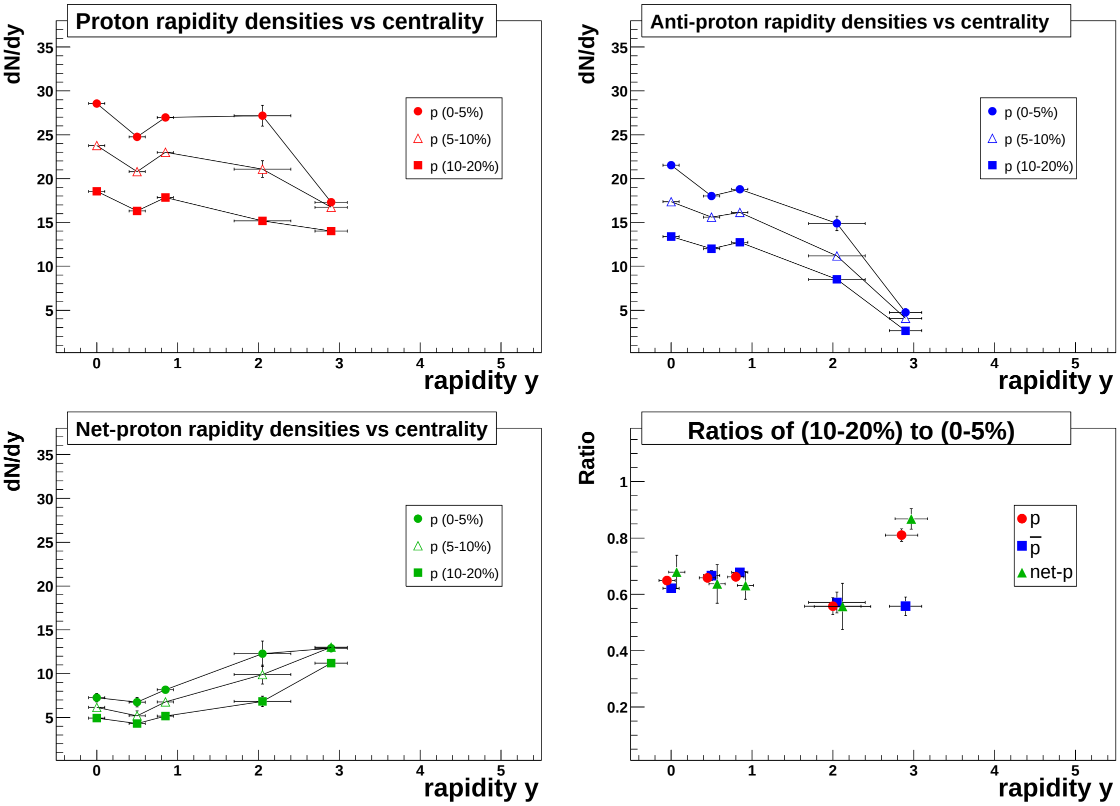

Figure 5.10: Centrality dependence of dN/dy for protons, anti–protons, and net–protons. The bottom right plot shows the ratio of proton, anti-proton, and net–proton yields from 10-20% to 0-5%. The rapidity points have been shifted slightly for protons and net–protons to make it clearer. Error bars are statistical only.

y interval	fit range	dN/dy	T (MeV)	χ^2/Ndof	$(dN/dy)^{counting}_{fitrange}$	$(dN/dy)^{fit}_{fitrange}$	$(dN/dy)^{counting}_{fitrange}/(dN/dy)$
$-0.10 < y < 0.00$	$0.4 < p_T < 2.9$	23.6 ± 0.3	364 ± 4	74.0/23	19.5 ± 0.3	19.8	83 %
		18.2 ± 0.4	353 ± 5	39.8/23	14.7 ± 0.4	15.2	81 %
$0.00 < y < 0.10$	$0.4 < p_T < 2.9$	24.4 ± 0.6	356 ± 5	67.6/23	19.7 ± 0.5	20.5	81 %
		16.9 ± 0.3	373 ± 5	59.1/23	13.9 ± 0.3	14.3	82 %
$0.40 < y < 0.50$	$0.3 < p_T < 2.5$	21.0 ± 0.6	376 ± 9	29.6/20	19.2 ± 0.6	18.7	91 %
		16.3 ± 0.5	366 ± 9	35.5/20	15.2 ± 0.5	14.5	93 %
$0.50 < y < 0.60$	$0.3 < p_T < 2.4$	20.6 ± 0.6	384 ± 10	40.0/19	19.0 ± 0.6	18.2	92 %
		14.9 ± 0.5	365 ± 11	41.8/19	13.8 ± 0.5	13.2	93 %
$0.75 < y < 0.85$	$0.5 < p_T < 2.1$	23.3 ± 0.4	364 ± 7	33.1/14	16.7 ± 0.3	17.0	72 %
		16.3 ± 0.4	375 ± 10	21.3/14	11.6 ± 0.3	11.9	72 %
$0.85 < y < 0.95$	$0.6 < p_T < 1.9$	22.5 ± 0.5	410 ± 12	23.1/11	14.3 ± 0.3	14.2	63 %
		16.0 ± 0.4	415 ± 15	14.5/11	10.0 ± 0.3	10.1	63 %
$1.70 < y < 2.00$	$0.2 < p_T < 1.6$	20.4 ± 1.1	395 ± 22	36.1/12	16.2 ± 0.7	16.2	80 %
		11.3 ± 0.5	365 ± 20	56.4/12	8.9 ± 0.4	9.3	78 %
$2.00 < y < 2.40$	$0.2 < p_T < 1.2$	23.1 ± 1.9	408 ± 36	8.0/8	14.6 ± 0.5	14.4	63 %
		10.0 ± 1.5	433 ± 74	9.0/8	6.2 ± 0.5	6.0	62 %
$2.70 < y < 2.85$	$0.8 < p_T < 1.8$	18.1 ± 1.3	283 ± 20	4.3/8	7.1 ± 0.4	7.2	39 %
		4.1 ± 0.5	303 ± 37	23.4/8	1.7 ± 0.2	1.7	41 %
$2.80 < y < 2.95$	$0.7 < p_T < 1.5$	14.0 ± 0.9	254 ± 25	5.5/6	5.9 ± 0.3	5.8	42 %
		4.8 ± 1.2	183 ± 40	6.4/6	1.8 ± 0.2	1.5	36 %
$2.85 < y < 2.95$	$0.8 < p_T < 1.7$	20.2 ± 0.8	318 ± 17	5.8/7	8.3 ± 0.3	8.3	41 %
		4.8 ± 0.4	299 ± 31	6.4/7	1.9 ± 0.1	1.9	41 %
$2.95 < y < 3.10$	$0.6 < p_T < 1.7$	16.0 ± 0.5	275 ± 11	8.4/9	9.0 ± 0.3	8.9	56 %
		3.6 ± 0.3	242 ± 17	8.0/9	1.9 ± 0.1	1.9	54 %

Table 5.2: The results of the fits to the proton and anti–proton p_T–spectra for the 5-10 % central data. The errors are statistical only. See Table 5.1 for explanations.

y interval	fit range	dN/dy	T (MeV)	χ^2/Ndof	$(dN/dy)^{counting}_{fitrange}$	$(dN/dy)^{fit}_{fitrange}$	$(dN/dy)^{counting}_{fitrange}/(dN/dy)$
$-0.10 < y < 0.00$	$0.4 < p_T < 2.9$	18.5 ± 0.2	359 ± 3	134.9/23	15.2 ± 0.2	15.5	82 %
		14.0 ± 0.3	348 ± 4	77.5/23	11.3 ± 0.2	11.7	80 %
$0.00 < y < 0.10$	$0.4 < p_T < 2.9$	18.7 ± 0.4	344 ± 4	59.0/23	14.9 ± 0.3	15.6	80 %
		13.1 ± 0.2	364 ± 4	64.0/23	10.8 ± 0.2	11.0	82 %
$0.40 < y < 0.50$	$0.3 < p_T < 2.5$	16.1 ± 0.3	368 ± 7	27.8/20	14.8 ± 0.4	14.4	92 %
		12.0 ± 0.3	370 ± 8	32.4/20	11.0 ± 0.3	10.7	91 %
$0.50 < y < 0.60$	$0.3 < p_T < 2.4$	16.5 ± 0.3	351 ± 7	28.2/19	14.9 ± 0.4	14.6	91 %
		12.0 ± 0.3	353 ± 8	44.2/19	11.4 ± 0.4	10.7	95 %
$0.75 < y < 0.85$	$0.5 < p_T < 2.1$	18.0 ± 0.3	362 ± 6	32.7/14	12.9 ± 0.2	13.1	72 %
		12.8 ± 0.2	352 ± 7	37.2/14	9.0 ± 0.2	9.3	71 %
$0.85 < y < 0.95$	$0.6 < p_T < 1.9$	17.7 ± 0.3	384 ± 8	26.9/11	11.1 ± 0.2	11.1	63 %
		12.6 ± 0.3	385 ± 11	20.6/11	7.9 ± 0.2	7.9	63 %
$1.70 < y < 2.00$	$0.2 < p_T < 1.6$	15.5 ± 0.6	346 ± 14	34.5/12	12.8 ± 0.5	13.0	82 %
		8.5 ± 0.3	390 ± 21	22.0/12	6.4 ± 0.2	6.8	75 %
$2.00 < y < 2.40$	$0.2 < p_T < 1.2$	14.7 ± 0.7	317 ± 19	4.4/8	10.6 ± 0.3	10.6	72 %
		8.5 ± 1.1	464 ± 68	14.7/8	5.4 ± 0.3	4.8	64 %
$2.70 < y < 2.85$	$0.8 < p_T < 1.8$	17.9 ± 1.2	232 ± 12	6.6/8	6.1 ± 0.2	6.0	34 %
		4.3 ± 0.5	239 ± 21	8.1/8	1.4 ± 0.1	1.5	33 %
$2.80 < y < 2.95$	$0.7 < p_T < 1.5$	12.1 ± 0.7	233 ± 17	8.4/6	4.8 ± 0.2	4.8	39 %
		3.7 ± 0.5	202 ± 26	12.5/6	1.4 ± 0.1	1.3	37 %
$2.85 < y < 2.95$	$0.8 < p_T < 1.7$	16.5 ± 0.6	278 ± 11	11.6/7	6.3 ± 0.2	6.3	38 %
		3.8 ± 0.3	272 ± 19	12.3/7	1.4 ± 0.1	1.4	38 %
$2.95 < y < 3.10$	$0.6 < p_T < 1.7$	13.5 ± 0.3	252 ± 7	9.0/9	7.3 ± 0.2	7.3	54 %
		2.4 ± 0.1	287 ± 18	13.0/9	1.4 ± 0.1	1.4	57 %

Table 5.3: The results of the fits to the proton and anti–proton p_T–spectra for the 10-20 % central data. The errors are statistical only. See Table 5.1 for explanations.

protons drop 25 % less than the anti–protons at that rapidity. Most systematic errors cancel when the ratios are constructed in this way, so the difference is significant. Compared to the other rapidities the drop is $\sim 15 - 25$ % less and indicates that the shape of the net–proton distribution is changing from central to less central collisions, and that the dip at mid–rapidity is more pronounced in less central collisions. This effect was also observed at lower energies, see e.g. Figure 2.3.

When comparing the anti–protons ratios at different rapidities, the ratios seem to be compatible with a value of 0.6 ± 0.05. This is consistent with the drop in the number of participants from ~ 350 in 0-5% collisions to ~ 220 in 10-20% collisions (Figure 1.6).

5.2 Comparison to other experiments

The STAR and PHENIX experiments have published results on proton and anti–proton yields at $\sqrt{s_{NN}} = 130$ GeV [58, 61, 60], and STAR has preliminary results for anti–protons at $\sqrt{s_{NN}} = 200$ GeV [59].

So far, STAR has only published the inclusive anti–proton yield at $y = 0$ and then deduced the net–protons from the $N(\bar{p})/N(p)$ ratio.

In the top centrality bin they find $dN/dy(\bar{p}) = 28.7 \pm 0.3(\text{stat.}) \pm 25\%(\text{syst.})$ (0-5%) at $\sqrt{s_{NN}} = 200$ GeV. This is $\sim 30\%$ larger than what was found here ($dN/dy(\bar{p}) = 21.5 \pm 0.3$ at $y = 0$), but if one takes the systematic error into account the results are consistent. The large discrepancy may be due to the fact that STAR only covers the range $0.25 < p_T < 0.95$ or ~ 45 % of the total yield [58].

From their $N(\bar{p})/N(p)$ ratio of $0.78 \pm 0.05(\text{syst.})$, they find $dN/dy = 8 \pm 2(\text{syst.})$ for net–protons at $\sqrt{s_{NN}} = 200$ GeV. The revised value from $\sqrt{s_{NN}} = 130$ GeV is $dN/dy = 8.4 \pm 2.9(\text{syst.})$.

PHENIX has measured both the feed–down corrected and uncorrected net–proton yield at $\sqrt{s_{NN}} = 130$ GeV. They find $dN/dy = 8.6 \pm 1.4(\text{stat.}) \pm 20\%(\text{syst.})$ before corrections and $dN/dy = 5.6 \pm 0.9(\text{stat.}) \pm 24\%(\text{syst.})$ after feed–down correction for Λ and $\bar{\Lambda}$, so the effect of the feed–down correction is $\sim 35\%$. The value before feed–down correction agrees with the STAR value.

The BRAHMS value for the net–proton yield, $dN/dy = 7.3 \pm 0.5$ at $y \sim 0$ is in agreement with the preliminary STAR value and similar to what was measured at $\sqrt{s_{NN}} = 130$ GeV.

Figure 5.11 shows a comparison between AGS, SPS, and the BRAHMS measurement presented in this thesis. The energy dependence is quite remarkable. At AGS energies the net–protons peaks at mid–rapidity, while at SPS a dip begins to develop in the middle of the distribution, and at RHIC a broad minimum has developed spanning several units of rapidity.

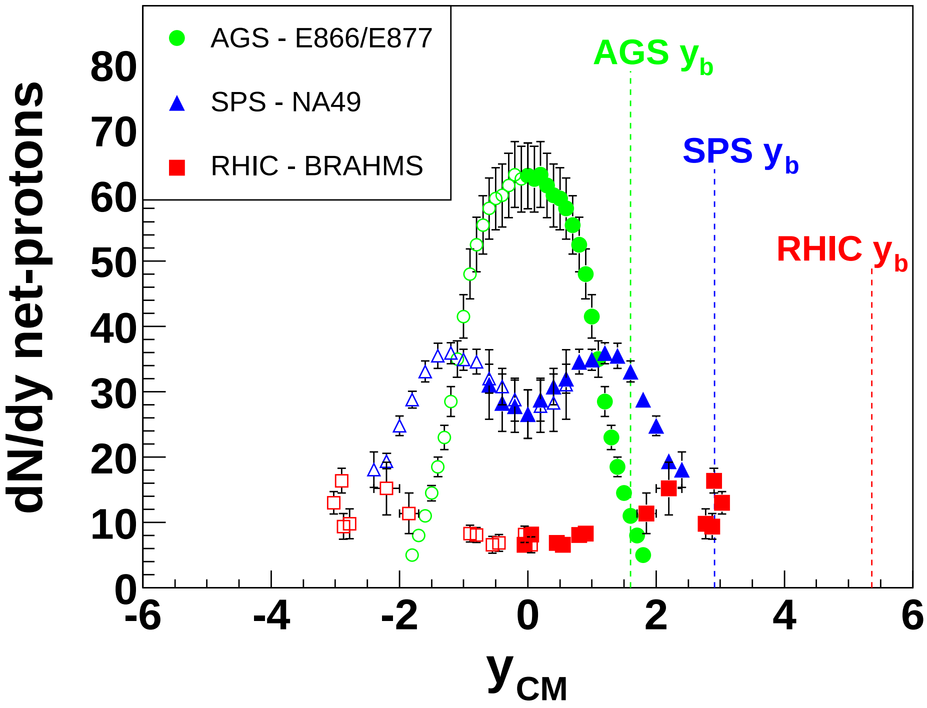

Figure 5.11: The energy systematics of the net–proton yields at AGS, SPS, and RHIC. The centrality selection is the same at all three energies and the number of participants is therefore roughly the same. The data has been symmetrized.

5.3 Model comparisons

Model	net-p	$\langle \delta y \rangle$	$\langle \delta y \rangle_{rel}$
HIJING	82.6	1.92	0.18
HIJING w. BJ	75.8	2.76	0.26
UrQMD	66.8	2.91	0.27
UrQMD ($\kappa = 3$)	55.8	3.25	0.30

Table 5.4: The predictions from the models. Net–p is the number of net–protons between mid–rapidity ($y = 0$) and rapidity $y = 6$. The rapidity loss $\langle \delta y \rangle$, and the relative rapidity loss $\langle \delta y \rangle_{rel}$, were defined in Chapter 2.

To make a comparison between the models presented in chapter 2 and the data, it is important to correct the data for hyperon decays. Hyperons are baryons with one or more strange quarks, so they can carry some of the net–baryon content after the collision.

The dominantly produced hyperon is the Λ ($\bar{\Lambda}$), but also the $\Sigma^0, \Xi^0,$and Ξ^-, that all decay to Λ's (100 %), and the Σ^+ that decays to a proton (52 %), will be considered here(as well as their antiparticles). A good estimate for the relative production of the hyperons is that the number of Λ particles equals the total number of Σ (+, 0, -) particles. The Λ has two primary decay modes $\Lambda \rightarrow p\pi^-(\sim 64\%)$ and $\Lambda \rightarrow n\pi^0(\sim 36\%)$. The proton from the first decay mode might be detected as a primary proton and lead to an overestimation of the original proton and anti–proton ($\bar{p}$ from $\bar{\Lambda}$) production. Due to the long lifetime ($c\tau = 7.89$ cm) the track does not have to point back to the IP, so not all tracks are accepted. This could depend strongly on initial momentum of the Λ, but there are two effects that tend to cancel each other out. At high momentum the life–time is longer in the laboratory frame and the Λ therefore decays further away from the IP than at low momentum and in that sense makes it more likely that the track is not pointing to the IP. However, since the lab–momentum is larger, the decay–angle between the decay products is smaller and this makes it more likely that the direction of the Λ and proton are the same. Here, the dependence on momentum has been ignored.

There have been attempts to measure the Λ and $\bar{\Lambda}$ production with the BRAHMS detector [18], but the analysis has had large problems because the solid angle coverage of the spectrometers is so low that it is very rare that both decay products can be identified in the spectrometer. Additionally, the tracking and IP determination is not good enough to determine the decay vertex. Instead the ratio of $\Lambda/p \sim \bar{\Lambda}/\bar{p} \sim 0.9$ (where $\Sigma^0, \Xi^0,$and Ξ^- are counted as Λ's) measured at $\sqrt{s_{NN}} = 130$ GeV [61] was assumed to be similar at $\sqrt{s_{NN}} = 200$ GeV and used to scale the input from an event generator.

The HIJING model was used as input to a BRAG simulation to determine the contamination at $y \sim 0$ and at $y \sim 1$. In the simulation it is known if a particle identified as a proton (with IP cut) was a primary proton or originated from a decay. The correction factor C can then be constructed as

$$C = \frac{N_p}{N_p + s \times N_\Lambda + s \times N_{\Sigma+}} \tag{5.1}$$

where N_p is the primary protons, N_Λ is the detected protons from Λ decays, $N_{\Sigma+}$ is the detected protons from Σ^+ decays, and s is a scale factor. The HIJING production ratios are $\Lambda/p \sim \bar{\Lambda}/\bar{p} \sim 0.4$ (where Σ^0, Ξ^0, and Ξ^- are counted as Λ's) so that the scale factor is $s = 0.9/0.4$. The correction factor was found to be $C \sim 0.75$ at both rapidities indicating that ~ 25 % of the measured protons originate from hyperon decays, and this value is used at *all* rapidities. Earlier studies have found that the correction was the same at $y \sim 0$ and $y \sim 3$ [62]. The correction is applied by multiplying the points in the net–proton rapidity distribution by 0.75.

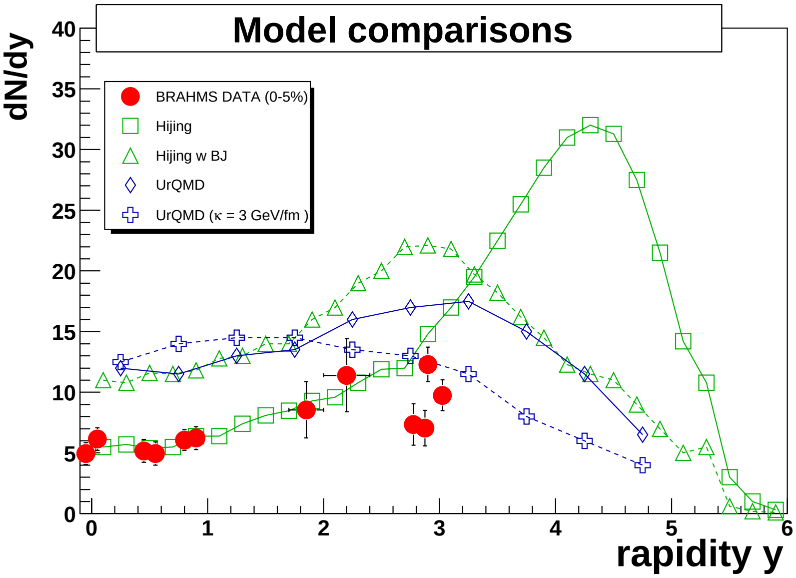

Figure 5.12: The net–proton distribution compared to the prediction of various models. The measured net–proton distribution has been corrected for Λ feed-down as discussed in the text. The model results have been read off from plots in the publications [31, 34], also shown in chapter 2.

Figure 5.12 displays the comparison of the model predictions shown in chapter 2 to the measured data. The data favors the HIJING model without the baryon junction mechanism, but at forward rapidity the data points is lower than the HIJING curve suggesting that the transparency is higher in the measured data. The proton transportation to mid–rapidity is too large in both versions of UrQMD and in HIJING with baryon junction. This indicates that there is no requirement for new mechanisms to produce the observed baryon stopping.

5.4 The rapidity loss

To calculate the rapidity loss $\langle \delta y \rangle$, the rapidity distribution of net–protons has to be known in principle from mid–rapidity to beam–rapidity. BRAHMS can only measure over the three first units of rapidity and the dN/dy–distribution has to be extrapolated to obtain the shape of the full distribution.

Since the baryon number is conserved, the integral of the net–baryon distribution (0-5 % central) should be $\sim$ 350 (see Figure 1.6) if the spectators are ignored, so initially there is $350 \times 79/197 = 140$ proton participants and 210 neutron participants. BRAHMS does not measure neutrons, hence the effect of the neutrons has to be estimated. Let us consider the following processes

$$\begin{array}{ll} p+p \rightarrow n+p+\pi^{+} & \text{converts a } p \rightarrow n \\ n+n \rightarrow n+p+\pi^{-} & \text{converts a } n \rightarrow p \\ p+n \rightarrow n+n+\pi^{+} & \qquad p \rightarrow n \\ p+n \rightarrow p+p+\pi^{-} & \qquad n \rightarrow p \end{array}$$

The two last processes occur with equal probability, so they can be disregarded. Initially there are twice ($210^2/140^2$) as many $n+n$ collisions as $p+p$ collisions, so there is a net conversion $n \rightarrow p$. This chemical equilibration would lead to an almost equal number of protons and neutrons after many interactions. This is in agreement with the predictions of the statistical model discussed in section 1.4.1.

Experimentally the yields of protons and neutrons in $p+A$ collisions have been studied with 12 GeV/c and 19 GeV/c proton beams (fixed target) [63]. At these low energies the pair production is negligible, so one effectively studies the isospin exchange process. The ratio

$$R = \frac{(dN/dy)_{protons}}{(dN/dy)_{neutron}} \tag{5.2}$$

is measured as a function of rapidity. The initial proton rapidity is $y = 3.7$, and it is found that R increases from 1 at $y \sim 2.3$ to 2.3 at $y \sim 3.3$. This shows that in collisions where the initial proton is transported to around mid–rapidity, there is equal probability of detecting a neutron and a proton, while if the rapidity loss is less, the probability of observing a proton increases (relative to the probability of observing a neutron).

There are therefore strong indications that there is a contribution to the net–protons from the neutron excess prior to the collision.

As was discussed in the last section some of the net–baryon content following the collision is carried by the hyperons. The system will also be driven toward chemical equilibration between e.g. $\Lambda, n,$ and p, but since the hyperons are heavier than the nucleons they are suppressed. Some of these hyperons will be measured as protons and thereby decrease this effect.

The total number of net–protons after the collision therefore depends on how the increase from $n \to p$ compares to the decrease $p \to \Lambda$. In the models HIJING and UrQMD the total number of net–protons after the collision is 163 and 134 respectively, see Table 5.4. Both numbers are similar to the original 140, indicating that in these models the two effects cancel. HIJING underestimates the Λ/p ratio at mid–rapidity, so the total number of net–protons is quite likely too high. Here 140 net–protons will be used in the following for the total number of net–protons that BRAHMS would measure if the full rapidity interval could be covered i.e., including protons from hyperon decays.

The number of net–protons in the rapidity region $-3 < y < 3$ is ~ 58 (see below) without the correction for hyperon decays. This suggests that BRAHMS covers $58/140 \sim 40$ % of the total net–proton yield. The remaining 60 % lies outside the rapidity interval covered by BRAHMS, so the maximum in the net–proton distribution is therefore *outside* the rapidity region covered by BRAHMS as was also indicated by Figure 5.11.

To obtain estimates of the rapidity loss, two different methods will be applied. The relative rapidity loss $\langle \delta y \rangle_{rel}$ will be compared to the model predictions and the near constant values observed at lower energies. The two methods are :

- Total number of net–protons based on the estimate above. The number of net–protons not measured by BRAHMS can then be assigned to $y \sim 3.5$ and $y \sim 5$ to estimate minimum and maximum values for the stopping.
- MCM inspired fit. Use a function assumed to describe the full rapidity distribution to extract the stopping power.

The net–proton rapidity distribution can be fitted with a second degree polynomial to obtain an estimate of the total number of net–protons and their average rapidity loss in the rapidity interval $0 < y < 3$. In this way it is found that there are ~ 29 net–protons with an average rapidity loss of $\langle \delta y \rangle \sim 3.67$. First, the 41 remaining net–protons are placed at rapidity $y = 3.5$ to gain an estimate for the maximum rapidity loss. The rapidity loss is :

$$\langle \delta y \rangle = \frac{3.67 \times 29 + (5.35 - 3.5) \times 41}{70} = 2.60 \tag{5.3}$$

and the relative rapidity loss is $\langle \delta y \rangle_{rel} = 0.24$.

Secondly, to obtain an estimate for the minimum rapidity loss, the 41 remaining net–protons are instead placed at $y \sim 5.0$. The rapidity loss is then $\langle \delta y \rangle = 1.73$ and the relative rapidity loss is $\langle \delta y \rangle_{rel} = 0.16$.

The second method is to use a fit function inspired by the MCM model discussed in section 2.3.1. The function

$$dN/dy = N \left((y + y_{beam})^{\alpha} e^{-\alpha(y + y_{beam})} + (y_{beam} - y)^{\alpha} e^{-\alpha(y_{beam} - y)} \right), \tag{5.4}$$

is inspired by equation 2.5, but it contains two parameters, the normalization N and the parameter α that can modify the shape analogous to what is done in the MCM model.

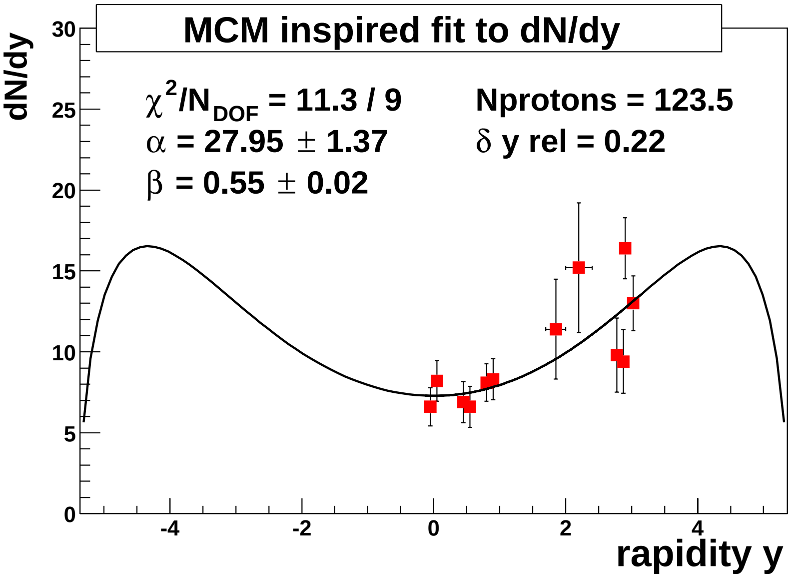

Figure 5.13: A fit to the net–proton data to extract the shape of the net–proton distribution and thereby determine the rapidity loss. The fit function is inspired by the MCM model.

Figure 5.13 shows the fit to the data obtained with this function. The total number of net–protons obtained from the fit is ∼ 10 % below the estimated value of 140, but the relative rapidity loss of $\langle \delta y \rangle_{rel} = 0.22$ is still below the maximum estimate from the first method.

Figure 5.14 shows an updated version of Figure 2.6 with the relative rapidity loss measured by BRAHMS and the predictions from the other models.

The estimated maximum for the relative rapidity loss is clearly lower than the $\langle \delta y \rangle_{rel} \sim 0.32$ observed at lower beam energies, so rapidity scaling is broken at RHIC.

The only models that have relative rapidity losses in the range between the minimum and maximum estimates are HIJING and the MCM. All the other models overestimates the rapidity loss.

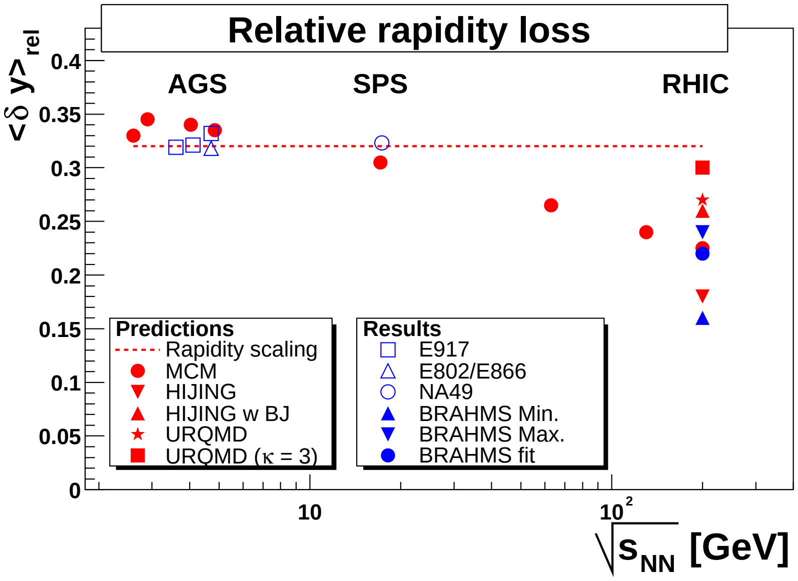

Figure 5.14: The relative rapidity loss as a function of beam energy for big systems ($Au + Au$ or $Pb + Pb$) in central collisions. The data points at lower energy have been read off from Figure 2.6.

Chapter 6

Conclusions

The invariant yields dN/dy for protons and anti–protons have been deduced from measurements at several rapidities in the interval $0.0 < y < 3.0$ in $Au + Au$ collisions at $\sqrt{s_{NN}} = 200$ GeV. For the most central data sample (0-5%) the proton yields decrease from $dN/dy(y = 0) = 28.6 \pm 0.3(\text{stat.}) \pm 1.0(\text{syst.})$ to $dN/dy(y = 3) = 17.3 \pm 0.4(\text{stat.}) \pm 1.8(\text{syst.})$, and the anti–proton yields decrease from $dN/dy(y = 0) = 21.5 \pm 0.3(\text{stat.}) \pm 0.9(\text{syst.})$ to $dN/dy(y = 3) = 4.7 \pm 0.2(\text{stat.}) \pm 1.4(\text{syst.})$. The width of the proton rapidity distribution is larger than the width of the anti–proton rapidity distribution indicating that at forward rapidities a larger fraction of the protons are net–protons than for rapidities closer to mid–rapidity.

The net–proton distribution ($dN/dy(p) - dN/dy(\bar{p})$) increases from $dN/dy(y = 0) = 7.3 \pm 0.5(\text{stat.}) \pm 1.0(\text{syst.})$ to $dN/dy(y = 3) = 12.9 \pm 0.4(\text{stat.}) \pm 1.6(\text{syst.})$ (0-5% centrality) and increases smoothly from mid–rapidity to rapidity $y = 3$. The shape of the net–proton rapidity distribution with the minimum at mid–rapidity indicates that a high degree of transparency is observed even in the most central collisions.

The total number of net–protons in the rapidity interval ($0.0 < y < 3.0$) has been evaluated to be 29 (0-5% centrality) without hyperon decay corrections. The total number of net–protons has been estimated to be ~ 70 in the rapidity interval ($0.0 < y < y_{beam}$), so a large fraction ($\sim 60\%$) of the total net–proton yield is outside the acceptance of the BRAHMS detector at rapidity $y > 3$, supporting the conclusion that the collisions are quite transparent.

The centrality dependence of the proton and anti–proton yields were studied in the centrality interval 0-20%. At almost all rapidity points identical scaling with centrality was observed between the most central data points (0-5%) and the most peripheral sample (10-20%). The sole exception was the proton yields at $y = 3$ which decreased by 20% less than any other yields. This deviation indicates that the shape of the net–proton rapidity distribution changes with centrality and the observed dip broadens in more peripheral collisions as was also observed at lower beam energies [16].

At lower bombarding energies (AGS and SPS) the maximum in the net–proton rapidity distribution in central collisions lies close to mid–rapidity. The measurement presented here shows that this trend is broken at RHIC and thereby suggests that the formation of the source at mid–rapidity is dominated by different physical processes then at lower energies.

Of the models that have been compared to the data, the basic version of HIJING was most successful at describing the net–proton rapidity distribution. This indicates that new mechanisms to enhance the baryon stopping, like baryon junction or larger string tensions, are not needed to describe stopping at RHIC.

Finally the relative rapidity loss was estimated to be in the range $0.16 < \langle \delta y \rangle_{rel} < 0.24$. This range excludes the constant value of $\langle \delta y \rangle_{rel} \sim 0.32$ observed at AGS, and CERN, and demonstrates that linear rapidity scaling of the rapidity loss is broken at RHIC.

Appendix A

The BRAHMS Collaboration

I. G. Bearden[7], D. Beavis[1], C. Besliu[10], Y. Blyakhman[6], B. Budick[6], H. Bøggild[7], C. Chasman[1], C. H. Christensen[7], P. Christiansen[7], J. Cibor[3], R. Debbe[1], E. Enger[12], J. J. Gaardhøje[7], M. Germinario[7], K. Hagel[8], O. Hansen[7], A. Holm[7], A. K. Holme[12], H. Ito[11], E. Jakobsen[7], A. Jipa[10], F. Jundt[2], J. I. Jørdre[9], C. E. Jørgensen[7], R. Karabowicz[4], T. Keutgen[8], E. J. Kim[1], T. Kozik[4], T. M. Larsen[12], J. H. Lee[1], Y. K. Lee[5], G. Løvhøiden[12], Z. Majka[4], A. Makeev[8], B. McBreen[1], M. Mikelsen[12], M. Murray[8], J. Natowitz[8], B. S. Nielsen[7], J. Norris[11], K. Olchanski[1], J. Olness[1], D. Ouerdane[7], R. Płaneta[4], F. Rami[2], C. Ristea[10], D. Röhrich[9], B. H. Samset[12], D. Sandberg[7], S. J. Sanders[11], R. A. Scheetz[1], P. Staszel[7], T. S. Tveter[12], F. Videbæk[1], R. Wada[8], A. Wieloch[4], Z. Yin[9], I. S. Zgura[10]

[1] Brookhaven National Laboratory, Upton, New York 11973, USA
[2] Institut de Recherches Subatomiques and Université Louis Pasteur, Strasbourg, France
[3] Institute of Nuclear Physics, Krakow, Poland
[4] Smoluchkowski Inst. of Physics, Jagiellonian University, Krakow, Poland
[5] Johns Hopkins University, Baltimore 21218, USA
[6] New York University, New York 10003, USA
[7] Niels Bohr Institute, Blegdamsvej 17, University of Copenhagen, Copenhagen 2100, Denmark
[8] Texas A&M University, College Station, Texas, 17843, USA
[9] University of Bergen, Department of Physics, Bergen, Norway
[10] University of Bucharest, Romania
[11] University of Kansas, Lawerence, Kansas 66049, USA
[12] University of Oslo, Department of Physics, Oslo, Norway

Appendix B

Kinematic and Other Variables

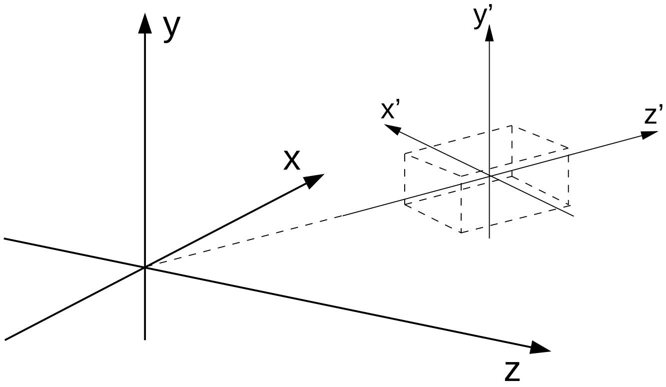

Figure B.1: The BRAHMS global and local coordinate systems. In the global coordinate system (denoted x, y, z) the nominal IP is located at $(0, 0, 0)$ and the z–axis follows the beam–line. The x–axis points toward the MRS and the y–axis is pointing toward the roof. For each detector a local system is defined (denoted x', y', z') with the z'–axis pointing away from the nominal IP and the y'–axis parallel to the y–axis.

The coordinate systems used to describe global and local positions are shown in Figure B.1. In the global coordinate system the beam axis and z–axis coincide.

The transverse momentum p_T and transverse mass m_T are defined as :

$$p_T = \sqrt{p_x^2 + p_y^2} \tag{B.1}$$

$$m_T = \sqrt{m^2 + p_T^2} \tag{B.2}$$

where m is the rest mass of the particle.

Instead of the longitudinal momentum p_z it is common to use the rapidity y :

$$y = \frac{1}{2} \ln \left(\frac{E + p_z}{E - p_z} \right) \tag{B.3}$$

where E is the energy $E = \mathbf{p}^2 + m^2$. If the system is Lorentz transformed along the beam axis (boosted) the rapidity changes by an additive constant (the rapidity of the moving frame of reference), so that the shape of the rapidity density distribution dN/dy, where N is the total number of the particles per event, is invariant.

The following relations are useful :

$$E = m_T \cosh(y) \tag{B.4}$$

$$p_z = m_T \sinh(y) \tag{B.5}$$

The pseudo–rapidity η is often used where the mass is unknown :

$$\eta = -\ln(\tan(\theta/2)) \tag{B.6}$$

where θ is the polar angle between the momentum vector $\mathbf{p}$ and the beam axis. If $|\mathbf{p}| \gg m$ then $\eta \sim y$.

In $p + p$ collisions it has been observed that the Feynman x (x_F) variable is a good scaling parameter i.e., the observed yields plotted as a function of x_F (dN/dx_F) are almost independent of beam energy. The Feynman variable is defined as :

$$x_F = \frac{p_z}{p_{z,MAX}} \tag{B.7}$$

and in the center of mass frame it is

$$x_F \approx \frac{2p_{z,CM}}{\sqrt{s_{NN}}} = \frac{2m_T \sinh(y_{CM})}{\sqrt{s_{NN}}} \tag{B.8}$$

Appendix C

BRAHMS Software

Some software has been specially developed for the BRAHMS experiment. Here the Brahms Analysis Tool (BRAT) and Brahms Analysis GEANT (BRAG) are described.

C.1 BRAT

BRAT is a set of C++ classes built on top of the ROOT library [64]. The classes are divided into different categories of which the most interesting are

- **db**. Database handling.
- **data**. Raw data and reconstructed data classes.
- **modules**. The active classes that perform input/output, tracking etc.

BRAT is used for storing raw data, calibrations, reconstruction etc.

C.2 BRAG

BRAG is a simulation tool based on the GEANT libraries [65], and contains the geometry and materials of the BRAHMS detector and experimental area. The input to the simulation is a distribution of charged particles at an IP that are then propagated through the detector elements. The output of a simulation contains information on the position and momentum of particles and their hits in the active detectors e.g. TPM1.

BRAG is used for generating the acceptance maps, studying multiple scattering, absorption, weak decay corrections, and tracking efficiencies etc.

Appendix D

The TOF m^2 Resolution

The parameterization of the m^2 resolution used in Figure 4.5 and Figure 4.7 have been derived in the following. The idea came from what was used in PHENIX [66]. The starting point is equation 3.4. It therefore follows from error propagation that the resolution σ_{m^2} is given by

$$\left(\frac{\sigma_{m^2}}{m^2}\right)^2 = 4\frac{\sigma_p^2}{p^2} + 4\gamma^4\frac{\sigma_\beta^2}{\beta^2} \tag{D.1}$$

The first term depends on the momentum resolution that can be parameterized as $\sigma_p^2/p^2 = p^2\sigma_{ang}^2 + (1+m^2/p^2)\sigma_{mult}^2$. The first term was derived in equation 3.3 in the small angle limit and depends on angular resolution of tracks and the magnitude of the magnetic field. The second term is a parametrization of the effect of multiple scattering taken from [66].

The second term in equation D.1 is related to the velocity resolution. The velocity is determined from time of flight, $\beta = l/\mathrm{TOF}$, so that

$$\frac{\sigma_\beta^2}{\beta^2} = \frac{\sigma_{\mathrm{TOF}}^2}{\mathrm{TOF}^2} + \frac{\sigma_l^2}{l^2} \approx \frac{\sigma_{\mathrm{TOF}}^2}{\mathrm{TOF}^2} \tag{D.2}$$

The approximation, $\sigma_l/l << \sigma_{\mathrm{TOF}}$ is, at least, good in the MRS where the dependence of l on the IP is small.

By using $\gamma = E/m$ the following parametrization of the m^2 resolution is obtained :

$$\sigma_{m^2}^2 = 4\left[m^4p^2\sigma_{ang}^2 + m^4\left(1+\frac{m^2}{p^2}\right)\sigma_{mult}^2 + (m^2+p^2)^2\sigma_t^2\right] \tag{D.3}$$

where $\sigma_t = \sigma_{\mathrm{TOF}}/l$.

In Figure D.1 the procedure for obtaining the parameters $\sigma_{ang}, \sigma_{mult}$, and σ_t is shown for a FFS setting. First the narrow bands in m^2 are sliced in momentum intervals and fitted with Gaussians. The small contamination in the pion sample from kaons is ignored. The kaons are ignored because they can only be separated from pions in a very short momentum range. The width $\sigma_{m^2}^2$ can then be fitted simultaneously for pions and protons. In the MRS kaons

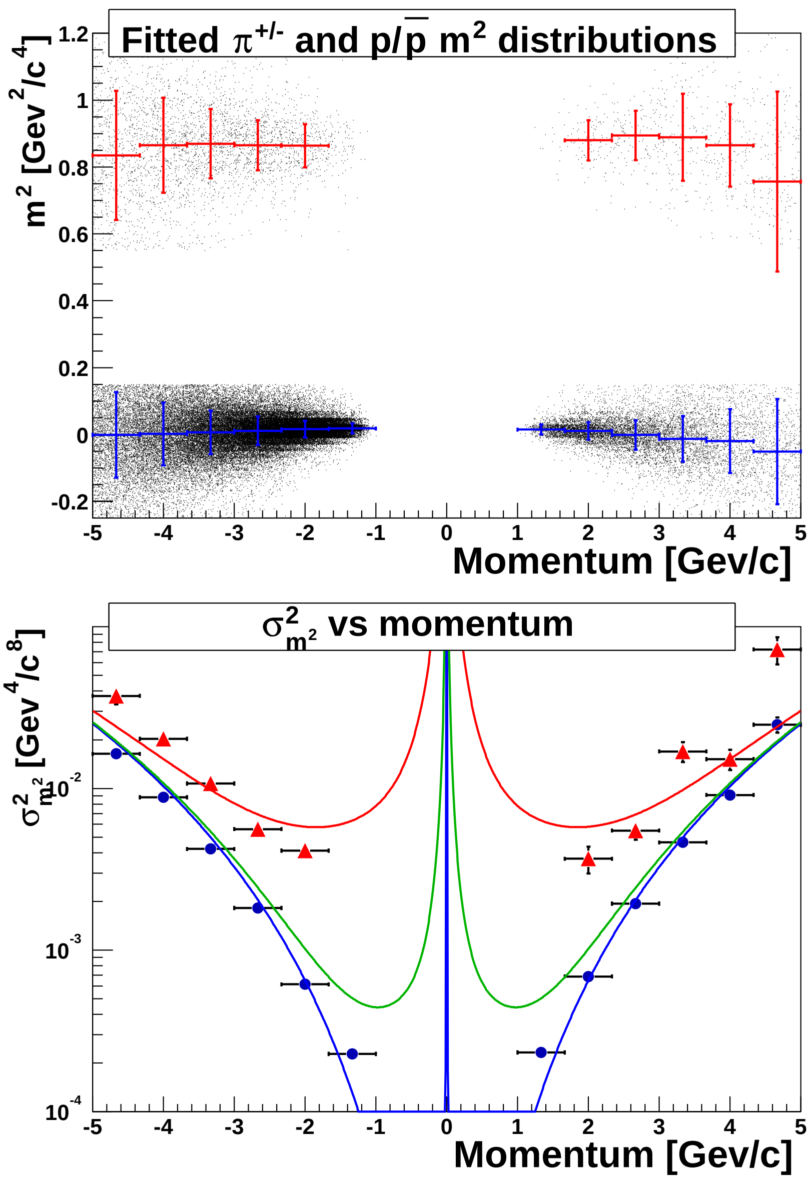

Figure D.1: The results for a 12 degree setting in the FFS. Top: Narrow bands in m^2 are fitted in small momentum intervals with Gaussians to extract the momentum dependence of the width of the pion (blue) and proton band (red). Bottom: The widths are fitted using equation D.3 to extract the momentum and TOF resolution. The green curve shows the prediction for kaons.

are also included in the fit.

The fit often has a very large value for χ^2 per degree of freedom, primarily because the momentum intervals are quite broad and the point is simply placed in the middle with very small error bars on the width of the Gaussian. The pions are more numerous than the protons and they therefore dominate the fit. These issues might make the selection non–optimal for protons but, as the figures of the proton selection in Chapter 4 show, the procedure works quite well.

Typical values for σ_{TOF} obtained from the fit are 70-110 ps in the MRS and 90-100 ps in the FS, which is consistent with the values determined from the velocity distribution of e.g. pions in a narrow momentum range.

Typical values for σ_{mult} are 0.02 in the MRS, and the multiple scattering component is negligible for most FS settings. The angular resolution σ_{ang} is consistent with the values obtained for the momentum resolution (there called σ_{res}) in section 3.4.

Appendix E

Fit functions

There are many possible fit functions. The functions used in this thesis are p_T–exponential, m_T–exponential, and Boltzmann. All parameterizations have two parameters. It is practical to choose the inverse slope and the rapidity density dN/dy for these parameters, since these are the quantities we are interested in. If they were to be derived from other fit parameters one would have to take the covariance matrix into account to get correct errors.

The following is an example of how to change parameters for the m_T–exponential (the fit–function used in this thesis) as well as for the results for the other functions quoted. The initial function is :

$$f(m_T) = ke^{-\frac{m_T}{T}} \tag{E.1}$$

The idea is to utilize $\frac{1}{2\pi m_T}\frac{d^2N}{dydm_T} = f(m_T)$, so that :

$$\begin{aligned}
Y &= \int_m^\infty \frac{d^2N}{dydm_T}dm_T \\
&= \int_m^\infty 2\pi k m_T e^{-\frac{m_T}{T}} \\
&= 2\pi k\left[-(Tm_T + T^2)e^{-\frac{m_T}{T}}\right]_m^\infty \\
&= 2\pi kT(m+T)e^{-\frac{m}{T}} \qquad \Rightarrow \\
k &= \frac{1}{2\pi}\frac{Y}{T(T+m)}e^{\frac{m}{T}}
\end{aligned}$$

inserting in equation E.1

$$f(m_T) = \frac{1}{2\pi}\frac{Y}{T(T+m)}e^{-\frac{m_T-m}{T}} \tag{E.2}$$

The p_T–exponential can be written as :

$$f(p_T) = \frac{1}{2\pi}\frac{Y}{T^2}e^{-\frac{p_T}{T}} \tag{E.3}$$

and the Boltzmann as :

$$f(m_T) = \frac{1}{2\pi}\frac{Y}{T(2T^2 + 2mT + m^2)}m_T e^{-\frac{m_T - m}{T}} \tag{E.4}$$

The m_T functions can be used to fit in p_T by substituting $m_T = \sqrt{p_T^2 + m^2}$.

Sometimes simultaneous fits are done to π, K, and p, to extract the transverse flow and the thermal freeze–out temperature. Often the hydrodynamical blast wave function is used in these fits, and it has also been used with BRAHMS data in the MRS [50].

Appendix F

The Acceptance Correction

This appendix contains a description of the details of generating the geometrical acceptance correction.

The simulation is carried out for IP bins of 5 cm with a flat IP distribution. The pion input distribution used for the simulation is a flat distribution in θ, ϕ, and momentum p. The ranges in θ, and ϕ are determined from the front of the magnet gap, taking the extreme of the ranges calculated using the 2 IP end points. The front of the magnet gap is used to ensure that all possibilities are covered.

Due to the sizes of the simulated files, there are many different data files for the same setting (even for the same IP range). It is therefore important that the random numbers are initialized differently for each file. In BRAG there are 2 random number generators used. The first one is a standard FORTRAN generator used to generate the input distribution, which uses **RANLUX**[1]. The second random number generator is used by GEANT itself for the physics[2]. Both generators must therefore be initialized.

The output of each simulated event is the input track and the hits in all the detectors. In this simulation we only activate the tracking detectors, dipole magnets, and PID detectors (TOFW, C1, etc.), so there is no beam pipe, multiplicity array, etc. The hits in the TPCs are converted to tracks using the Brahms Analysis Tool (BRAT) class **BrGeantToTpcTrackCandidate**. They are then matched with the matching module and the swim status is used to reject tracks that are close to the magnet with the same cut as on real data.

F.1 The Software

The software used to generate the acceptance files is located in
brahms_app/pc_app/brag/generate.

---

[1] (http://wwwinfo.cern.ch/asdoc/shortwrupsdir/v115/top.html)

[2] **BASE420** (http://wwwinfo.cern.ch/asdoc/geant_html3/node44.html)

There are two programs : **mrsgenerate** and **fsgenerate**. The options for **mrsgenerate** are :

```
 -e  --events           Number of events, default is 2000000
 -h  --help             Show this help, default is true
 -M  --max              Max momentum, default is 4.05
 -m  --min              Min momentum, default is 0.1
 -n  --name             base name of files, default is generate
 -E  --prfile           Number of events pr file, default is 500000
 -R  --range            Range of accepted vtx, default is 17.5
 -r  --run              Run number, default is 0
 -N  --step             Number of steps to divide vtx range in, default is 7
 -V  --version          Version number, default is false
```

The default is to generate 2 million single particle events for each vertex setting, with the momentum range $0.1 < p < 4.05$. The base name of each file is **generate** and each kumac generates 500 k events. There are 7 IP bins from -17.7 to 17.5. Finally you must supply a run number to get the right geometry. The program takes into account that TPM1, D5, and TPM2 were moved back for some of the runs.

After executing the command :

```
~/brahms_app/pc_app/brag/generate/mrsgenerate -r 5692
```

The directory should now contain :

```
generate_8          generate_8_20.kumac  generate_9_11.kumac
generate_8_01.kumac generate_8_21.kumac  generate_9_12.kumac
generate_8_02.kumac generate_8_22.kumac  generate_9_13.kumac
generate_8_03.kumac generate_8_23.kumac  generate_9_14.kumac
generate_8_04.kumac generate_8_24.kumac  generate_9_15.kumac
generate_8_05.kumac generate_8_25.kumac  generate_9_16.kumac
generate_8_06.kumac generate_8_26.kumac  generate_9_17.kumac
generate_8_07.kumac generate_8_27.kumac  generate_9_18.kumac
generate_8_08.kumac generate_8_28.kumac  generate_9_19.kumac
generate_8_09.kumac generate_9           generate_9_20.kumac
generate_8_10.kumac generate_9_01.kumac  generate_9_21.kumac
generate_8_11.kumac generate_9_02.kumac  generate_9_22.kumac
generate_8_12.kumac generate_9_03.kumac  generate_9_23.kumac
generate_8_13.kumac generate_9_04.kumac  generate_9_24.kumac
generate_8_14.kumac generate_9_05.kumac  generate_9_25.kumac
generate_8_15.kumac generate_9_06.kumac  generate_9_26.kumac
```

```
generate_8_16.kumac  generate_9_07.kumac  generate_9_27.kumac
generate_8_17.kumac  generate_9_08.kumac  generate_9_28.kumac
generate_8_18.kumac  generate_9_09.kumac
generate_8_19.kumac  generate_9_10.kumac
```

The 8 and 9 indicates the GEANT PID of the thrown particles, $8 = \pi^+$ and $9 = \pi^-$. There are 28 files because there are 4 files for each vertex setting (2M/500k) and 7 vertex settings. An example of a kumac is given in section F.2. When **generate_8** and **generate_9** are executed (make executable first) all the kumacs are submitted to the **rcas** nodes using **bsub**. For each kumac the output is a GEANT cdat file.

The cdat files can be read and converted into an acceptance map using the bratmain script **brahms_app/pc_app/brag/acceptance/cdat2acc.C**. The call is commented out at the end of **generate_8** and **generate_9** files and should be executed when all the cdat files are available.

For the FS the software has been designed along the same lines.

F.2 Example of a Generation Kumac

```
* acceptance on (means that brag stops if particle
* hits magnet iron) in the real world pions could
* go though a part of the magnet and be seen
cards accp 1
* physics included
dcay 0
muls 0
loss 1
munu 0
phot 0
comp 0
pair 0
brem 0
dray 0
anni 0
hadr 0
* recalculate cross sections
physi

geoini
* mrs on
```

```
set_tree mids o
* tpm1, tpm2, tofw active, d5 on
set_tree tpm1 afo
set_tree d5 o
set_tree tpm2 afo
set_tree tofw afo
* mrs angle 90 deg.
set_mangle 90
* 2001 setup
* set tpm1 geometry
set_param tpm1 deltay 1.8
set_param tpm1 deltaz 0.0
* set tpm2 geometry
set_param tpm2 deltax 0.2
set_param tpm2 deltay 2.05
set_param tpm2 deltaz -5.4
set_param tpm2 refang -0.34
* set tpm2 instrumentation 2^0 (=row 1) + 2^1 (=row 2) etc.
set_param tpm2 actrows 248883
* full tofw
set_param tofw mode 2
* turn fs off
set_tree fms1 z
set_tree fms2 z
* turn zdc, dx magnet, beam pipe, mult, bb off
set_tree zdc z
set_tree dx z
set_tree beam z
set_tree mult z
set_tree bb z
geodef
geofin
call gbr2c.f
* call to functions in gbr2c.f
call init_detector
call initrandom(1)

* set magnet field
```

```
set_field m0 -2.12407
* Setup vertex (negative sigma means flat distribution)
* x_mean x_sigma  y_mean y_sigma z_mean z_sigma x_max y_max z_max
u/c/spot 0.0 0.0 0.0 0.0 -15 -2.5

* define thrown particles pid
*  8 pi+, 9 pi-, 11 K+, 12 K-, 14 p+, 15 p-
*
* select flat distribution in p, theta and phi
cards ukin 1
* define thrown range : 0.1 < p < 4.05, theta range, phi range, pid range
kine 1 0.1 4.05 77.0315 91.8843 -1.88529 1.88529 8 8
* do 1 track at a time
evsplit 1
* output format
cards spac 1
swit 3 1

setup/save geom mrs.geo
setup/save magnet mrs.mag
* open outputfile
call gbrfile('brag_run5692_pid08_01.cdat')
* saveoptions are defined in gbr2c.f (3 means always save thrown track)
call saveoption(3)

* throw 500000 events and print event number every 10000
analyze gbrana 500000 10000

* close file
call gbrend

quit
```

Appendix G

How to Add Spectra from Different Settings

The purpose of this appendix is to discuss how to average over histogram cells in the $1/N * 1/p_T * d^2N/dydp_T$ distribution, when making 1–dimensional projections or summing over different settings or IP bins. A problem occurs when there are no counts. If there are counts, we have an error ($\sqrt{n}$) and can use the error as weight in a weighted average calculation.

G.0.1 The Method

The information we have available consists of measurements for $p_i = n_i/N_i * \varepsilon_i$:

- **p** "Probability" in one event for observing one particle in the cell ($1/N * 1/p_T * d^2N/dydp_T$). This is the value we must determine.
- $\mathbf{N_i}$ The number of events accepted in an event sample.
- $\varepsilon_{\mathbf{i}}$ Overall acceptance, efficiency, $1/p_T$, etc.
- $\mathbf{n_i}$ The actual number of particles in the cell.

We want to determine the best possible estimate for p and the error, $\hat{p}$ and $\sigma_{\hat{p}}$. The cell count n_i is Poisson distributed :

$$P(n_i) = \frac{\mu_i^{n_i}}{n_i!} \exp(-\mu_i) \tag{G.1}$$

where $\mu_i = N_i * \varepsilon_i * p$.

In the spirit of the maximum likelihood method we can construct the likelihood function :

$$L(p) = \prod_i P(n_i) = \prod_i \frac{\mu_i^{n_i}}{n_i!} \exp(-\mu_i) \tag{G.2}$$

Taking the logarithm :

$$\begin{aligned} \log L(p) &= \sum_i n_i \log \mu_i - \log n_i! - \mu_i \\ &= \sum_i n_i \log N_i \varepsilon_i + n_i \log p - \log n_i! - N_i \varepsilon_i p \end{aligned} \tag{G.3}$$

And differentiating with respect to p :

$$\begin{aligned} \frac{d \log L(p)}{dp} &= \sum_i \frac{n_i}{p} - N_i \varepsilon_i = 0 \quad \Rightarrow \\ \hat{p} &= \frac{\sum_i n_i}{\sum_i N_i \varepsilon_i} \end{aligned} \tag{G.4}$$

This expression has a simple interpretation. The nominator is the total number of measured particles and the denominator is the total number of tries scaled for efficiency etc.

The statistical error purely comes from the nominator and so the relative error on the calculated probability is the relative error on the nominator :

$$\sigma_{\hat{p}} = \frac{\hat{p}}{\sqrt{\sum_i n_i}} \tag{G.5}$$

G.0.2 A Test Simulation of the Method

To test equation G.4 and equation G.5, I implemented a small root script (`brahms_app/pc_app/yields/sum/testTheory.C`) with a class that that takes the following arguments :

- **fNSamples** Number of “cells”
- **fEffLow** Minimum efficiency.
- **fEffHigh** Maximum efficiency.
- **fNLow** Minimum number of throws.
- **fNHigh** Maximum number of throws.
- **fProbability** Probability that the throw ends up in the cell.

The program then generates (call **Generate**) fNSamples distributions with random flat efficiency and a random flat number of throws and calculates the estimated probability and error.

One can now perform many tests with the same parameters and compare the output to the input, see Figure G.1. The only variable that is changed between the three simulations is the probability. Values for the other parameters are shown in Table G.1.

In Figure G.1 the histogram output from 3 tests is displayed. The top column shows the deviation from the input probability fitted with a Gaussian over the full range. The Gaussian fit is quite good, but we begin to see minor deviations at the edges when the probability goes down and the spread increases, because the probability cannot be negative. It is good to see that when we look at the calculated error (middle row) the mean agrees with the standard deviation of the Gaussian fit of the deviation. The width of the distribution illustrates the strong dependence on the number of cell counts. The bottom row shows the distribution of the deviation divided by the error. By doing that I hoped to get similar Gaussian distributions for the 3 cases with sigmas of 1.0. The first two cases are, but the last case is clearly not Gaussian. In case 3 there is a very low estimated number of counts ($\langle n \rangle = 10 * 1500 * 0.6 * 0.001 = 9$) where we are on the limit if errors are really Gaussian distributed.

Params	**values**
fNSamples	10
fEffLow	0.2
fEffHigh	1.0
fNLow	1000
fNHigh	2000

Table G.1: Parameters used for the 3 simulation.

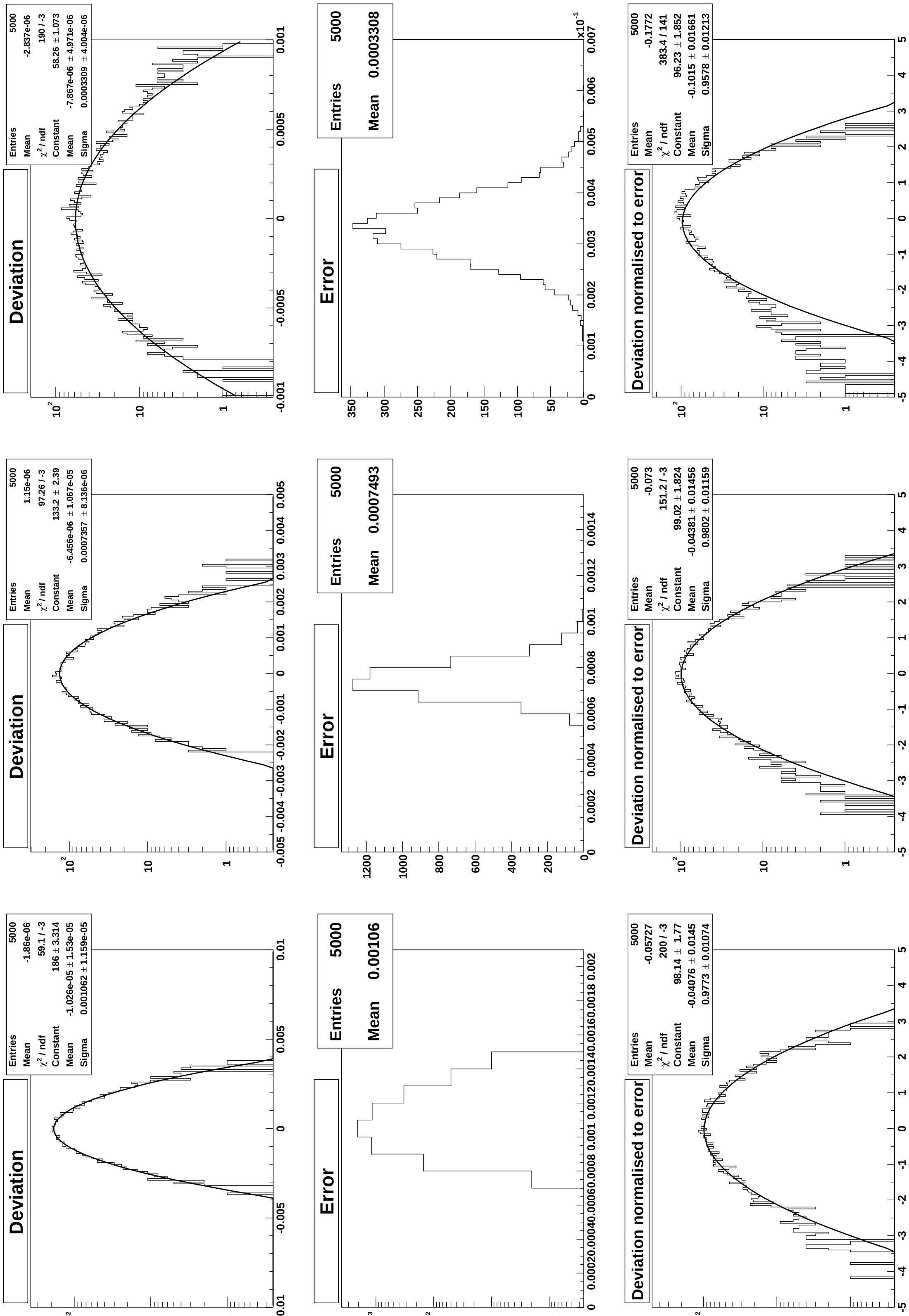

Figure G.1: The output from the simulation for 3 different probabilities, p=0.10 (left column), p=0.05, p=0.01(right column).

Appendix H

Transverse Momentum Spectra

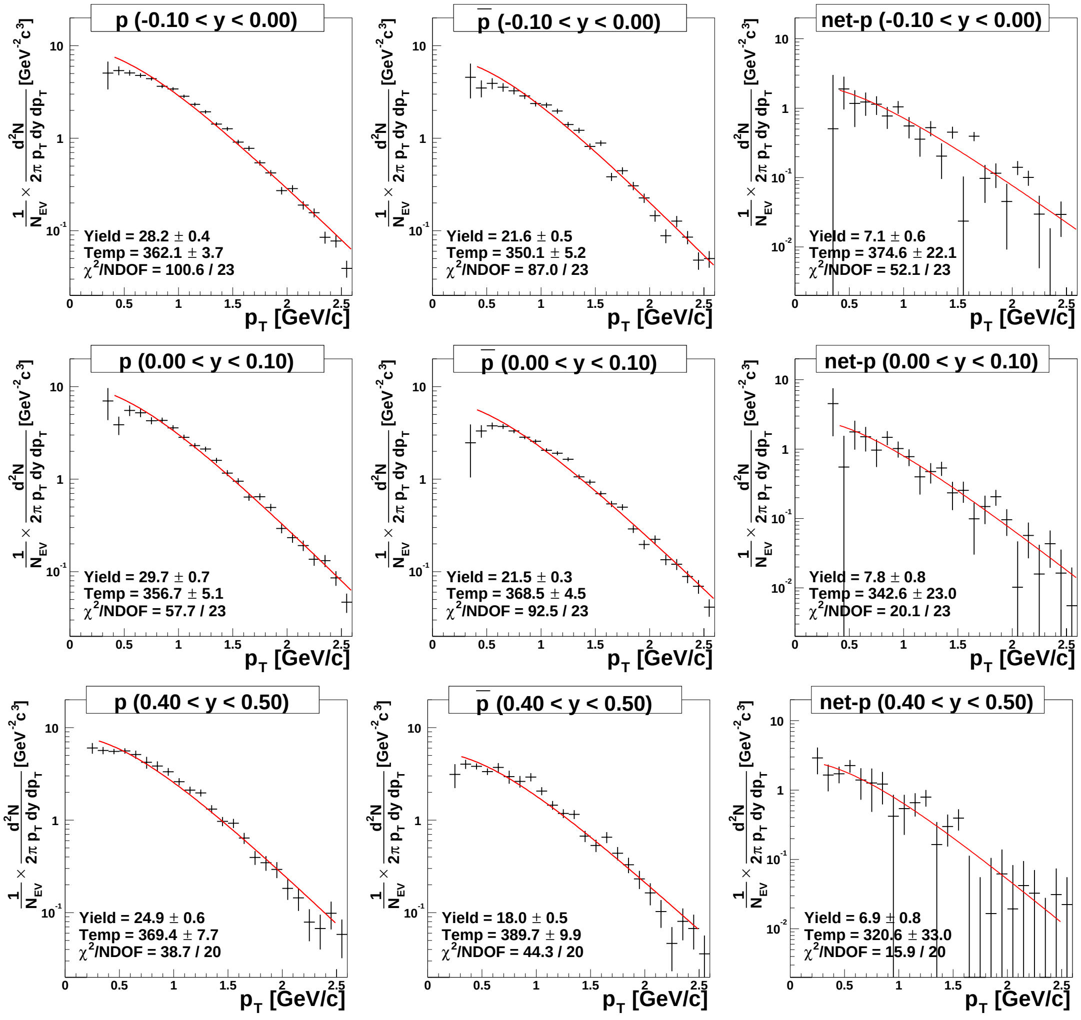

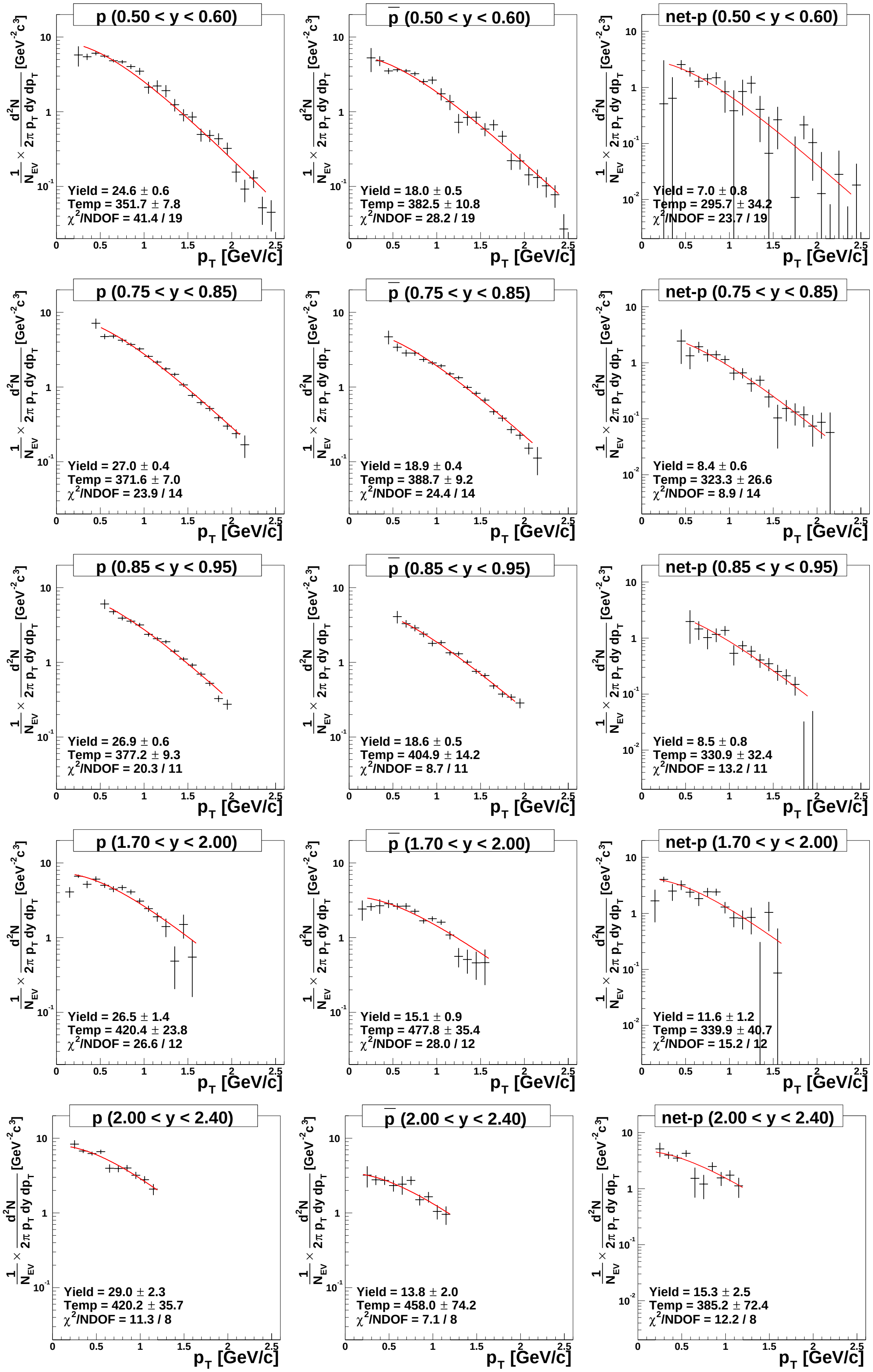
p (0.50 < y < 0.60)
Yield = 24.6 ± 0.6
Temp = 351.7 ± 7.8
χ2/NDOF = 41.4 / 19
p̄ (0.50 < y < 0.60)
Yield = 18.0 ± 0.5
Temp = 382.5 ± 10.8
χ2/NDOF = 28.2 / 19
net-p (0.50 < y < 0.60)
Yield = 7.0 ± 0.8
Temp = 295.7 ± 34.2
χ2/NDOF = 23.7 / 19
p (0.75 < y < 0.85)
Yield = 27.0 ± 0.4
Temp = 371.6 ± 7.0
χ2/NDOF = 23.9 / 14
p̄ (0.75 < y < 0.85)
Yield = 18.9 ± 0.4
Temp = 388.7 ± 9.2
χ2/NDOF = 24.4 / 14
net-p (0.75 < y < 0.85)
Yield = 8.4 ± 0.6
Temp = 323.3 ± 26.6
χ2/NDOF = 8.9 / 14
p (0.85 < y < 0.95)
Yield = 26.9 ± 0.6
Temp = 377.2 ± 9.3
χ2/NDOF = 20.3 / 11
p̄ (0.85 < y < 0.95)
Yield = 18.6 ± 0.5
Temp = 404.9 ± 14.2
χ2/NDOF = 8.7 / 11
net-p (0.85 < y < 0.95)
Yield = 8.5 ± 0.8
Temp = 330.9 ± 32.4
χ2/NDOF = 13.2 / 11
p (1.70 < y < 2.00)
Yield = 26.5 ± 1.4
Temp = 420.4 ± 23.8
χ2/NDOF = 26.6 / 12
p̄ (1.70 < y < 2.00)
Yield = 15.1 ± 0.9
Temp = 477.8 ± 35.4
χ2/NDOF = 28.0 / 12
net-p (1.70 < y < 2.00)
Yield = 11.6 ± 1.2
Temp = 339.9 ± 40.7
χ2/NDOF = 15.2 / 12
p (2.00 < y < 2.40)
Yield = 29.0 ± 2.3
Temp = 420.2 ± 35.7
χ2/NDOF = 11.3 / 8
p̄ (2.00 < y < 2.40)
Yield = 13.8 ± 2.0
Temp = 458.0 ± 74.2
χ2/NDOF = 7.1 / 8
net-p (2.00 < y < 2.40)
Yield = 15.3 ± 2.5
Temp = 385.2 ± 72.4
χ2/NDOF = 12.2 / 8
1/N_EV × d2N/(2π pT dy dpT) [GeV-2c3]
pT [GeV/c]
0
0.5
1
1.5
2
2.5
10-2
10-1
1
10

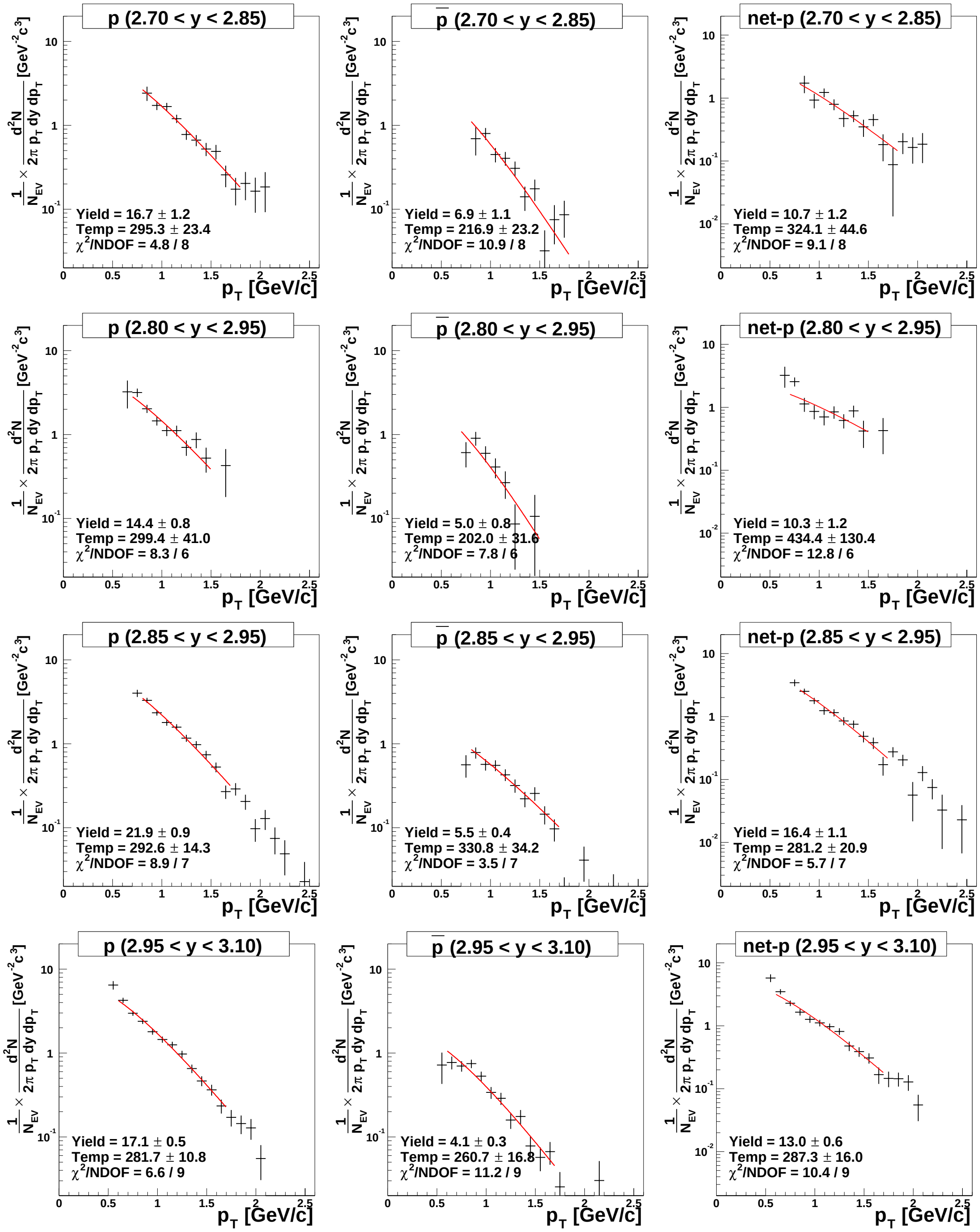
p (2.70 < y < 2.85)
Yield = 16.7 ± 1.2
Temp = 295.3 ± 23.4
χ²/NDOF = 4.8 / 8
p̄ (2.70 < y < 2.85)
Yield = 6.9 ± 1.1
Temp = 216.9 ± 23.2
χ²/NDOF = 10.9 / 8
net-p (2.70 < y < 2.85)
Yield = 10.7 ± 1.2
Temp = 324.1 ± 44.6
χ²/NDOF = 9.1 / 8
p (2.80 < y < 2.95)
Yield = 14.4 ± 0.8
Temp = 299.4 ± 41.0
χ²/NDOF = 8.3 / 6
p̄ (2.80 < y < 2.95)
Yield = 5.0 ± 0.8
Temp = 202.0 ± 31.6
χ²/NDOF = 7.8 / 6
net-p (2.80 < y < 2.95)
Yield = 10.3 ± 1.2
Temp = 434.4 ± 130.4
χ²/NDOF = 12.8 / 6
p (2.85 < y < 2.95)
Yield = 21.9 ± 0.9
Temp = 292.6 ± 14.3
χ²/NDOF = 8.9 / 7
p̄ (2.85 < y < 2.95)
Yield = 5.5 ± 0.4
Temp = 330.8 ± 34.2
χ²/NDOF = 3.5 / 7
net-p (2.85 < y < 2.95)
Yield = 16.4 ± 1.1
Temp = 281.2 ± 20.9
χ²/NDOF = 5.7 / 7
p (2.95 < y < 3.10)
Yield = 17.1 ± 0.5
Temp = 281.7 ± 10.8
χ²/NDOF = 6.6 / 9
p̄ (2.95 < y < 3.10)
Yield = 4.1 ± 0.3
Temp = 260.7 ± 16.8
χ²/NDOF = 11.2 / 9
net-p (2.95 < y < 3.10)
Yield = 13.0 ± 0.6
Temp = 287.3 ± 16.0
χ²/NDOF = 10.4 / 9
1/N_EV × d²N/(2π p_T dy dp_T) [GeV⁻²c³]
p_T [GeV/c]
0
0.5
1
1.5
2
2.5
10⁻²
10⁻¹
1
10

Appendix I

Acronyms

ADC Analog–to–Digital converter

AGS Alternating Gradient Synchrotron

BB Beam Beam Counters

BFS Back Forward Spectrometer

BNL Brookhaven National Laboratory

BRAG Brahms Analysis GEANT

BRAHMS Broad Range Hadronic Magnetic Spectrometers

BRAT Brahms Analysis Tool

C1 Threshold Cherenkov in FFS

CERN European Organization for Nuclear Research

D1 Dipole magnet in front of the FFS

D2 Dipole magnet in FFS between T1 and T2

D3 Dipole magnet in BFS between T2 and T3

D4 Dipole magnet in BFS between T3 and T4

D5 Dipole magnet in BFS between T4 and T5

DAQ Data Acquisition

DC Drift Chamber

FFS Front Forward Spectrometer

FS Forward Spectrometer

GEANT CERN developed Monte Carlo Tool

H1 TOF detector in FFS

H2 TOF detector in BFS

HBT Hanbery–Brown Twiss interferometry

HIJING Heavy–Ion Jet Interaction Generator

IP Interaction Point

LQCD Lattice QCD

MA Multiplicity Array

MCM Multi Chain Model

MC Monte Carlo

MIP Minimum Ionizing Particle

MRS Mid Rapidity Spectrometer

NA49 Large TPC experiment at CERN

PHENIX One of the big experiment at RHIC

PHOBOS The other small experiment at RHIC

PID Particle Identification

PMT Photo Multiplier Tubes

QCD Quantum Chromo Dynamics

QED Quantum Electro Dynamics

QGP Quark Gluon Plasma

RHIC Relativistic Heavy Ion Collider

RICH Ring Imaging Cherenkov

ROOT An Object–Oriented Data Analysis Framework

RQMD Relativistic Quantum Molecular Dynamics

SIS Heavy–Ion Synchrotron

SPS Super Proton Synchrotron

STAR One of the big experiments RHIC

T0 Start Time

T1 Front TPC in the FFS

T2 BackTPC in the FFS

T3 Front DC in the BFS

T4 Middle DC in the BFS

T5 Back DC in the BFS

TMA Tile Multiplicity Array

TOFW TOF detector in MRS

TOF Time Of Flight

TPC Time Projection Chamber

TPM1 Front TPC in the MRS

TPM2 BackTPC in the MRS

UrQMD Ultra–relativistic Quantum Molecular Dynamics

VENUS Event generator

ZDC Zero Degree Calorimeters

pQCD Perturbative QCD

Bibliography

[1] S. Bethke, arXiv:hep-ex/0211012 (2002)

[2] T. R. Klassen, Phys. Rev. D 51, 5130 (1995)

[3] Z. Fodor, S.D. Katz, JHEP 0203, 014 (2002)

[4] F. Karsch, E. Laermann, A. Peikert, Nucl. Phys. B605, 579 (2001)

[5] R.J. Glauber, Lectures in theoretical Physics (Inter–Science, New York, 1959) Vol. 1

[6] Lecture notes UCT 05, `http://hep.phy.uct.ac.za/~steinber/lectures/`

[7] STAR Collaboration, Phys. Rev. Lett. 89, 202301 (2002)

[8] J.D. Bjorken, Phys. Rev. D 27, 140 (1983)

[9] P. Braun-Munzainger, D. Magestro, K. Redlich, J. Stachel, Phys. Lett. B 518, 41 (2001)

[10] P. Braun-Munzainger, J. Stachel, J. Phys. G 28, 1971 (2002)

[11] R. Stock, arXiv:hep-ph/0212287

[12] NA50 Collaboration, Phys. Lett. B 477, 28 (2000)

[13] S. Mioduszewski for the PHENIX Collaboration, arXiv:nucl-ex/0210021

[14] BRAHMS Collaboration, Nucl. Phys. A 715, 741 (2003)

[15] STAR Collaboration, Phys. Rev. Lett. 90, 0823021 (2003)

[16] E917 Collaboration, Phys. Rev. Lett. 86, 1970 (2001)

[17] F. Videbæk, O. Hansen, Phys. Rev. C 52, 2684 (1995)

[18] BRAHMS Master thesis by Mads Gammeltoft (2002)

[19] A. Rybicki for the NA49 Collaboration, Acta Phys. Pol. B 33, 1483 (2002)

[20] FOPI Collaboration, Phys. Rev. C 57, 244 (1998)

[21] N. Hermann, J.P. Wessels, T. Wienold Annu. Rev. Nucl. Part. Sci. 49, 581 (1999)

[22] NA49 Collaboration, Phys. Rev. Lett. 82, 2471 (1999)

[23] F. Videbæk, Proc. 17th Winter Workshop on Nuclear Dynamics (arXiv:nucl-ex/0106017) (2001)

[24] S. Date, M. Gyulassy, H. Sumiyoshi, Phys. Rev. D 32, 619 (1985)

[25] M. Gyulassy, V. Topor Pop, S.E. Vance, arXiv:nucl-th/9706048

[26] B. Andersson, C. Gustafson, G. Ingelman, T. Sjöstrand, Phys. Rep. C 97, 31 (1983)

[27] J. Ranft, Phys. Rev. D 37, 1842 (1988)

[28] X. Wang, M. Gyulasssy, Phys. Rev. D 44, 3501 (1991)

[29] PHOBOS Collaboration, Phys. Rev. Lett. 85, 3100 (2000)

[30] S.A. Bass et al., Nucl.Phys. A661, 205 (1999)

[31] S.E. Vance, M. Gyulassy, X. Wang, Phys. Lett. B 443, 45 (1998)

[32] S.A. Bass et al., Prog. Part. Nucl. Phys. 41, 225 (1998)

[33] M. Bleicher et al., J. Phys. G 25, 1859 (1999)

[34] S. Soff, J. Randrup, H. Stöcker, N. Xu, Phys. Lett. B 551, 115 (1998)

[35] M. Harrison, S. Peggs, T. Roser, Annu. Rev. Nucl. Part. Sci. 52, 425 (2002)

[36] BRAHMS Collaboration, Nucl. Instr. Meth. A 499, 437 (2003)

[37] BRAHMS Collaboration, Phys. Lett. B 523, 227 (2001)

[38] BRAHMS Collaboration, Phys. Rev. Lett. 88, 202301(2002)

[39] BRAHMS Ph.d. thesis by Yury Blyakhman

[40] BRAHMS Ph.d. thesis by Djamel Ouerdane (2003)

[41] BRAHMS Ph.d. thesis by Hironori Ito (2002)

[42] BRAHMS Master thesis by Erik Jakobsen

[43] BRAHMS Master thesis by Christian Holm Christensen (2003)

[44] M. Chiu et al., Phys. Rev. Lett. 89, 012302 (2002)

[45] C. Adler et al., Nucl. Instr. Meth. A 470 (2001) 488

[46] BRAHMS Master thesis by Jens Ivar Jordre

[47] DC studies - BRAHMS Analysis Notes 27, 29, 34, and 38

[48] BRAHMS Master thesis by Radek Karabowicz (2002)

[49] `http://www.nbi.dk/~pchristi/BRAHMS/TPC/`

[50] BRAHMS Master thesis by David Sandberg

[51] `http://www4.rcf.bnl.gov/brahms/WWW/private/meetings/Dec2002/richeff.pdf`

[52] `http://www.nbi.dk/~pchristi/BRAHMS/SPECTRA/tpm1eff.html`

[53] P. Staszel, BRAHMS Analysis note 27

[54] BRAHMS Master thesis by Truls Martin Larsen

[55] `http://pii3.brahms.bnl.gov/~ejkim/brahms/mrs_cor.html` and `http://pii3.brahms.bnl.gov/~ejkim/brahms/fs_cor.html`

[56] `http://www.nbi.dk/~ouerdane/quick/#multi`

[57] BRAHMS Collaboration, Phys. Rev. Lett. 90, 102301 (2003)

[58] STAR Collaboration, Phys. Rev. Lett. 87, 2623021 (2001) and Erratum to be published with revised net–proton value.

[59] G. Buren for the STAR Collaboration, arXiv:nucl-ex/0211021

[60] PHENIX Collaboration, Phys. Rev. Lett. 88, 242301 Phys. (2002)

[61] PHENIX Collaboration, Phys. Rev. Lett. 89, 0923021 (2002)

[62] BRAHMS Collaboration, Net–proton QM02 proceeding (see BRAHMS homepage)

[63] E941 Collaboration, Phys. Rev. C 65, 014904 (2001)

[64] ROOT homepage `http://root.cern.ch/`

[65] CERN Program Library Long Writeup W5013

[66] PHENIX Ph.d. thesis by Jane Muriel Burward–Hoy (2001)